FACOLTÀ DI SCIENZE MATEMATICHE FISICHE E NATURALI

DIPARTIMENTO DI FISICA

TESI DI LAUREA MAGISTRALE

Hunting X17 using resonant production at PADME

Laureando:
Marco MANCINI

Relatori:
Prof.ssa Annalisa D'ANGELO
Prof. Mauro RAGGI
Dott.ssa Paola GIANOTTI

ANNO ACCADEMICO 2021/2022

Abstract

The lack of direct experimental observations of dark matter candidates at electroweak scale energies could be resolved by introducing a hidden sector that can only weakly interact with the Standard Model. The mediator that allows this interaction is the Dark Photon. Several experiments around the world are searching for a dark photon in the visible or invisible decays. One candidate is the X17 particle, a boson of mass ~ 17 MeV that would explain the nuclear anomalies of ^{8}Be and ^{4}He. These anomalies were observed in an experiment studying nuclear transitions via Internal Pair Creation. The PADME experiment allows the energy range of the mass of X17 to be tested with a positron beam interacting with the electrons of a fixed target. The aim of my thesis work is to study the feasibility of searching for X17 at PADME and determine its sensitivity.

Index

1 Introduction to Hidden Sectors

The discovery of the Higgs boson completed the framework of the Standard Model (SM) theory. Although, the picture it describes seams somehow incomplete, since many phenomena could not be understood with the SM, and they may indicate that it is just an approximation of another more fundamental theory. These phenomena have been observed in several areas of physics, such as cosmology, particle and nuclear physics.

The early cosmological observations of the anomalous dispersion velocity of the Coma cluster galaxies [1], the rotational speed of galaxies observed to be approximately flat instead of exhibiting the expected $1/\sqrt{r}$ behaviour [2] indicates the existence of a new form of matter. More recently, other anomalous effects observed on gravitational lensing [3], on Bullet cluster studies and on the Cosmological Microwave Background radiation, led to the introduction of non-visible matter: the Dark Matter (DM). The Dark Matter cannot be incorporated within the Standard Model and its possible understanding requires the introduction of new degrees of freedom, weakly interacting with the ordinary matter.

The recent measurements of the antiproton spectrum in the cosmic rays provided an additional evidence that antimatter in the cosmic rays is not just due to secondary production. This result, together with the positron excess observed in cosmic rays, could be interpreted as products of the annihilation of Dark Matter particles. The annihilation could lead to the production of an interaction carrier which subsequently decays into Standard Model particles [4].

A direct search of a signature of Dark Matter is carried out with the hunting for the Weakly Interacting Massive Particles (WIMPs) [5], which could represent a good candidate for DM. An excess of events of unknown origin has been reported by the DAMA-LIBRA collaboration [6], but it has never been confirmed by other experiments. In any case, the preferred region of parameters clusters towards WIMPs mass in the range of $\sim 10\,\mathrm{GeV} - 10\,\mathrm{TeV}$. The mechanism of the WIMPs scattering could involve an interaction carrier of approximately arbitrary mass.

In the field of particle physics, the recent disagreement showed by the muon g-2 collaboration [7] between the measured and the calculated anomalous magnetic momentum of the muon represents another issue that can be explained if new not yet observed particles exist. The difference between the experimental value and the SM prediction is found to be $4.2\,\sigma$. This discrepancy can indicate lepton flavour non-universality (or violation) since it relates the electromagnetic coupling constant, determined mostly from the anomalous magnetic momentum of the electron a_e, with the a_μ and is a result of the description of the two observables with a single interaction constant. A solution to this problem, but also to the precedents, could be New Physics (NP) effects, represented by a light hypothetical vector boson from the dark sector that couples to the Standard Model. The preferred mass region for this new particle lies in the interval $m \sim 10 - 100$ MeV.

Concerning nuclear physics, the study of the de-excitation of nuclear states via Internal Pair Conversion (IPC) has shown unexpected results [8]. The angular distribution of the electron-positron pairs emitted by the IPC shows a peak that can not be ascribed to nuclear effects and has been explained by some authors [9, 10] as due to a new unknown particle. More details on this scenario will be provided in this thesis work.

The explanation of any of the described phenomena requires introduction of physics beyond the Standard Model. One of the possible directions is to introduce new particles of higher mass, above the threshold reached so far. However, with the present highest energy reached at colliders, none indications of New Physics has been observed. A complementary approach is represented by the so-called precision physics. This requires high statistics and/or high intensity to study rare unexplained phenomena. The lack so far of experimental evidence of WIMPs and of any other Dark Matter candidates, has driven the attention towards new explanations. The introduction of a new hidden sector, where the dark particles could interact only among them, constrained by some kind of symmetries, is one of the possible alternative scenarios.

Essentially, the mass scale of the hidden sector can be arbitrary if it respect the constraint of being weakly coupled with the SM. Then, the New Physics contribution can be described as a combination of two terms, one corresponding to high masses and suppressed by the UV scale Λ_{UV}, and other long distance infrared (IR) contribution. The Lagrangian will appear like:

$$\mathcal{L} = \mathcal{L}_{SM} + \mathcal{L}_{NP} \tag{1.1}$$

where $\mathcal{L}_{NP} = \mathcal{L}_{UV} + \mathcal{L}_{IR}$. This thesis work will focus on the infrared contributions, explaining the model which describes them and providing some experimental results [4].

1.1 The weakly coupled light particles panorama

The most general low energy extension of the Standard Model, introduces the so-called dark sector characterised by an extremely weak coupling with the hadronic matter. The connection between the the two sectors is usually expressed through a mediator that is a particle owning both Standard Model and dark sector quantum numbers. An alternative to the "direct connection" is inferring the dark sector indirectly, trough loop diagrams or mixing processes. Both scenarios are possible, and the different categories of models depends on the spin-parity state of the mediator. A reasonable constraint to the models is that of considering only extensions with operators in the Lagrangian with dimension at most four. This simplifies the picture and gives a separate attention to the infrared physics only.

Depending on the spin-parity state of the mediator, different "portals" to the hidden sector can be identified:

- **Scalar portal**: the mediator is a scalar particle interacting with the Higgs boson of the Standard Model. This includes both operands dimensionally allowed in the Lagrangian, resembling the Higgs potential

$$\mathcal{L} \sim \mu S H^{\dagger} H + \lambda S^2 H^{\dagger} H. \tag{1.2}$$

  The best way to search for such type of new particles is through the study of the Higgs boson and its decays. Then, the most appropriate experiments to address this scenario are those at high energy colliders, *i.e.* LHC experiments like CMS and ATLAS.

- **Pseudoscalar portal**: with the introduction of a new Peccei-Quinn global $U(1)$ symmetry, which is broken spontaneously, it is possible to find a solution to the strong CP problem. The Nambu-Goldstone boson of the symmetry breaking is the axion. Adding the axion a to the Lagrangian corresponds to take into account the interaction of the axions with the Standard Model fermions

$$\mathcal{L} \sim \frac{\partial_\mu a}{f_a} \, \bar{\psi}_f \gamma^\mu \gamma_5 \psi_f. \tag{1.3}$$

The axion mass and the coupling to the Standard Modell depend strictly to the magnitude of the $U(1)$ symmetry breaking scale f_a. Other axion-like particles (ALPs) are allowed and their parameters are free, then also the couplings of the ALPs to the Standard Model are arbitrary.

- **Neutrino portal**: the neutrino mass puzzle provides input for few interesting models explaining these phenomena. The existence of a sterile neutrino may lead to an additional Yukawa term

$$\mathcal{L} \sim Y_N L H N. \tag{1.4}$$

This sterile neutrino would be a Standard Model singlet and would be produced in the early Universe. If the relic abundance and interaction strength with the dark matter are present, they will delay the DM kinetic decoupling and then provide a solution to the problem with the missing-small scale structures, like satellite galaxies.

- **Vector portal**: a general interaction of an electrically neutral vector particle A' with the Standard Model fermions can be written as:

$$\mathcal{L} \sim g' q_f \bar{\psi}_f \gamma^\mu \psi_f A'_\mu \tag{1.5}$$

where g' is the universal coupling constant of the new interaction and q_f is the charge associated to each interacting fermion.

Other extensions of the Standard Model may involve new interactions with the already known matter. They could be made anomaly free (like in the case of B-L as a gauge symmetry) and then the interaction term could be of order $D \leq 4$. The tree level process may again proceed through vector particles that are neutral under any of the Standard Model gauge groups. In order to focus mostly on the vector portal, we need to introduce the so-called "dark photons" models. The dark photon class of models includes all the interactions that involve a neutral vector mediator. These models do not require the introduction of any UV physics and can be probed with good efficiency at high intensity and low energy experiments. This scenario is also the most experimentally tested.

1.2 The dark photon models

The models classified as dark photon models (or hidden photons or heavy photons) are those predicting the existence of a new neutral vector particle (A') which

has a non-vanishing coupling to the Standard Model fermions in the form described in equation 1.5 and represented schematically in Fig. 1.1. The A' could
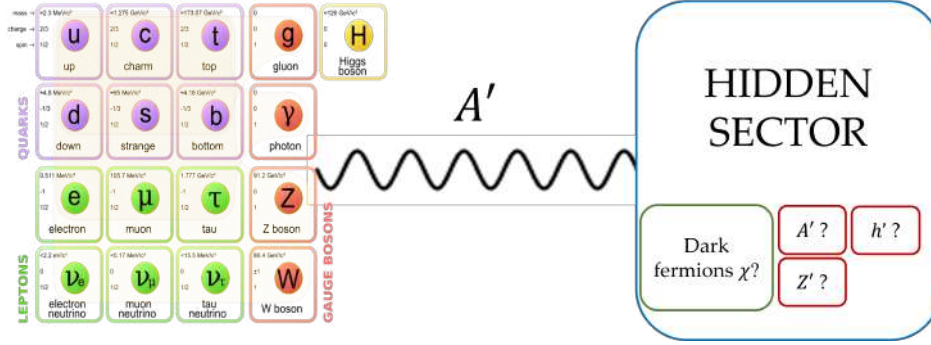

Figure 1.1: A schematic representation of the dark photon class of models: the mediator particle owns both SM and hidden sector quantum numbers.

itself be the mediator between the visible and the dark sector, but the link can also be realised in different ways. The origin of the coupling of the A' to fermion fields could arise in various modes. Since almost any extension of the Standard Model introduces new symmetries and gauge groups, the wide range of possibilities go from maximally universal models to other that only include a single type of fermions or even a single generation. The hidden symmetry group that mixes with SM particles can be realised in many different ways, some of them are presented below.

1.2.1 The dark photon kinetic mixing

One of the best motivated dark photon model is the kinetic mixing model, in which a new $U(1)_D$ group is introduced, responsible for the interactions between the particles in the dark sector. It works as the hypercharge of the Standard Model particles, and require that the dark photon could mix with the ordinary photon.

$$\mathcal{L}_{mix} = -\frac{\varepsilon}{2} F^{\mu\nu} F'_{\mu\nu} \tag{1.6}$$

Where $F^{\mu\nu}$ and $F'_{\mu\nu}$ are the field strength of the two $U(1)_{Y,D}$ symmetry groups. When the electroweak symmetry breaks this introduces an effective interaction between the fermions and the dark photon in the form

$$\mathcal{L} \sim \varepsilon e \bar{\psi} \gamma^{\mu} \psi A'_{\mu}, \tag{1.7}$$

where the charges of the individual fermions are exactly the electromagnetic ones. In this model the dark photon could be either massive or massless. The main characteristic of the kinetic mixing model is that all the phenomenology

depends on two parameters: the coupling strength ε and the dark photon mass $m_{A'}$. For these parameters several constraints already exists and will be described in section 1.4.

1.3 The A' production and decay mechanism

The experimental approaches to search for the A' can be divided into two classes: in the first one, the A' is produced via its coupling to the quarks, in the second one via its coupling to $e^{\pm}$. In principle, there should exist a third class where the A' production occurs via Dark Matter annihilation. Nevertheless, this is clearly not accessible to us. This thesis work will focus on the A' coupling to the electrons, then in the next section such processes will be described.

1.3.1 A' Production with leptons

The processes involving $e^{\pm}$ that can allow the production of a dark photon, at energies $\mathcal{O}(\mathrm{GeV})$, are shown in Fig. 1.2. Diagram Fig. 1.2a and 1.2b describe the A' resonant $e^- e^+ \rightarrow A'$ and associated $e^- e^+ \rightarrow \gamma A'$ production, via positrons annihilation on atomic electrons, respectively. The first production mechanism is actually the most important for this thesis work, since is the one that will be considered to test the X17 production at PADME. Diagram in Fig. 1.2c, instead, represents the "A'-strahlung" process, *i.e.* the radiative dark photon emission by an $e^{\pm}$ induced by the electromagnetic field of a target nucleus [11, 12].
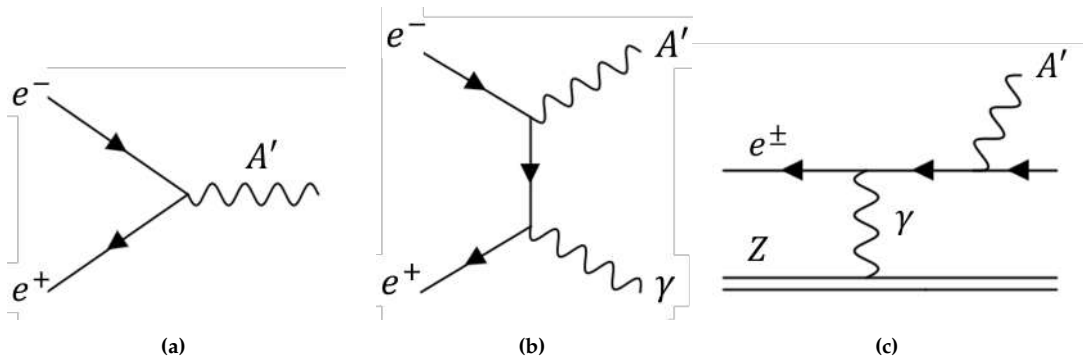

Figure 1.2: Feynman diagrams of the A' **(a)** resonant production via $e^+ e^-$ annihilation; **(b)** associated production via $e^+ e^-$ annihilation; **(c)** radiative emission via A'-strahlung.

The interaction of a positron beam with a fixed target allows to access all three diagrams in Fig. 1.2.

1.3.2 A' **decay mechanism**

Depending on the relative values of the masses of the hidden gauge mediator and of the particles belonging to the hidden sector, the dark photon can undergo visible or invisible decays. If the mass of the A' is lighter than twice the mass of any Dark Matter particle χ, $m_{A'} < 2m_\chi$, the decay in DM particles is kinematically forbidden and the dark photon can only decay to SM particles: this hypothesis is referred to as "visible decays". A sketch of the trend of the branching fractions of A' visible decays in several channels, as a function of the A' mass, is reported in Fig. 1.3. The proper lifetime for the visible A' decay in SM particles is:

$$c\tau = \frac{1}{\Gamma} \propto \frac{1}{\varepsilon^2 m_{A'}}. \tag{1.8}$$

Equation 1.8 depends from the inverse of ε^2, and its direct consequence is the possibility of investigating small couplings by experiments able to detect considerably detached decay vertices.

On the other hand, if the A' decays to lighter particles of the hidden sector are kinematically allowed, "invisible decays" will mainly occur. In this case, the visible branching fractions will be reduced in strength by a factor α_D^2.

The decays in DM particles escape of course the detection by particle detectors, but can be inferred by missing-mass or missing momentum techniques. The A' can also, in principle, decays into mixed final states containing both SM and dark particles. In this case, the decay identification would benefit from missing-energy techniques, that are mostly insensitive to the set of particles produced in the final state.
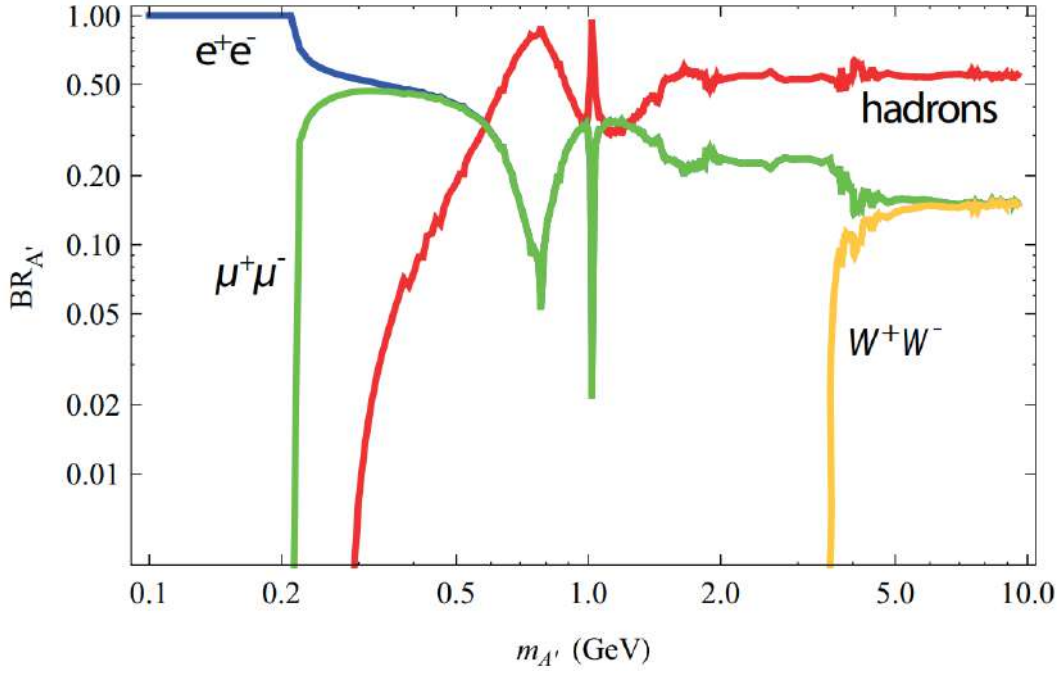
Figure 1.3: Dark photon "visible decay" modes and their branching fractions (with respect to the $A' \rightarrow e^- e^+$) for different dark photon mass values.

1.4 The constraints on A' parameters

In this section I report a summary of the main features and strategies adopted in past, present, and future experiments searching for the dark photon and Dark Matter candidates with mass lighter than 10 GeV at accelerator facilities.

All the constraints on the space parameters reported here are shown as exclusion limits derived at 90 % Confidence Level.

1.4.1 General constraints to dark photon existence

The dark photon visible decays are mostly constrained by bump-hunting, beam-dump and decay-vertex reconstruction experiments. Fig. 1.4 shows the current experimental constraints on the visible decays of the dark photon. In general, three regions can be identified, relative to a different detection strategy. The upper part of Fig. 1.4, corresponding to $\varepsilon^2 \geq 10^{-6}$ and 10 MeV $< m_{A'} <$ 10 GeV, refers to bump-hunt searches performed at beauty and kaon factories, electro-production experiments and hadron induced reactions. The exclusion region related to the a_μ value, is also shown. The nearly triangular bottom-left shaded region ($10^{11} \leq \varepsilon^2 \leq 10^6$, 1 MeV $\leq m_{A'} \leq$ 200 MeV) is covered by old beam-dump experiments, and by astrophysical observations. The central region of Fig. 1.4

can be mostly accessed by experiments able to reconstruct the A' decay vertex [13].
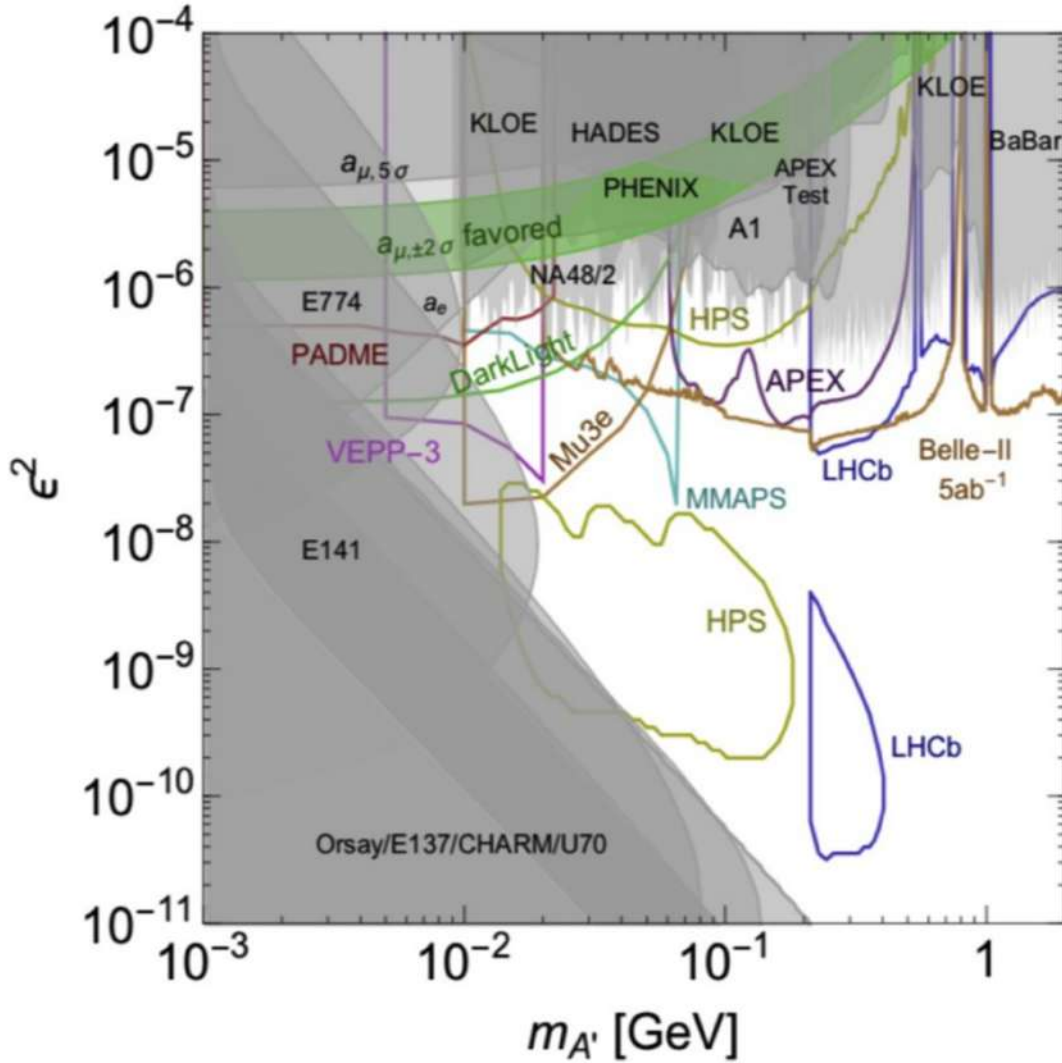
Figure 1.4: Existing bounds (shaded regions) and projected sensitivities of ongoing/proposed experiments (lines) for dark photon in visible decays in the square of mixing strength ε^2 with respect to the mass parameter plane. The constraints are given at 90 % CL [13].

The invisible decay searches are based on the general assumption that new particles χ in the hidden sector have mass lower than $m_{A'}/2$. Then, the dominant A' decay mode is invisible: $A' \to \chi\chi$ *i.e.* $\Gamma(A' \to \chi\chi)/\Gamma_{tot} \simeq 1$. The magnitude of this decay mode is controlled by the dark fine structure constant $\alpha_D = \frac{g_D^2}{4\pi}$. The invisible decays can be detected by using missing-mass, missing-energy or missing-momentum techniques. The direct detection of the DM particles from the decay can potentially be achieved via beam-dump experiments. Differently from the dark photon case, the search for DM χ particles involves a four-dimensional parameter space which includes the mass of the χ and of the A' and the two couplings α_D and ε.

Fig. 1.5 shows the current constraints on the dark photon invisible decays, where the shaded regions are set by missing mass experiments (BABAR [14], NA62 [15], E787 [16], E949 [17]), missing energy/momentum experiments (NA64 [18]) and the a_μ studies [13].

Figure 1.5: The current parameter space associated to the A' invisible decay. The shaded region correspond to previous experimental results: BABAR [14], NA62 [15], E787 [16], E949 [17], NA64 [18] and the present a_μ studies. The constraints are given at 90 % CL [13].
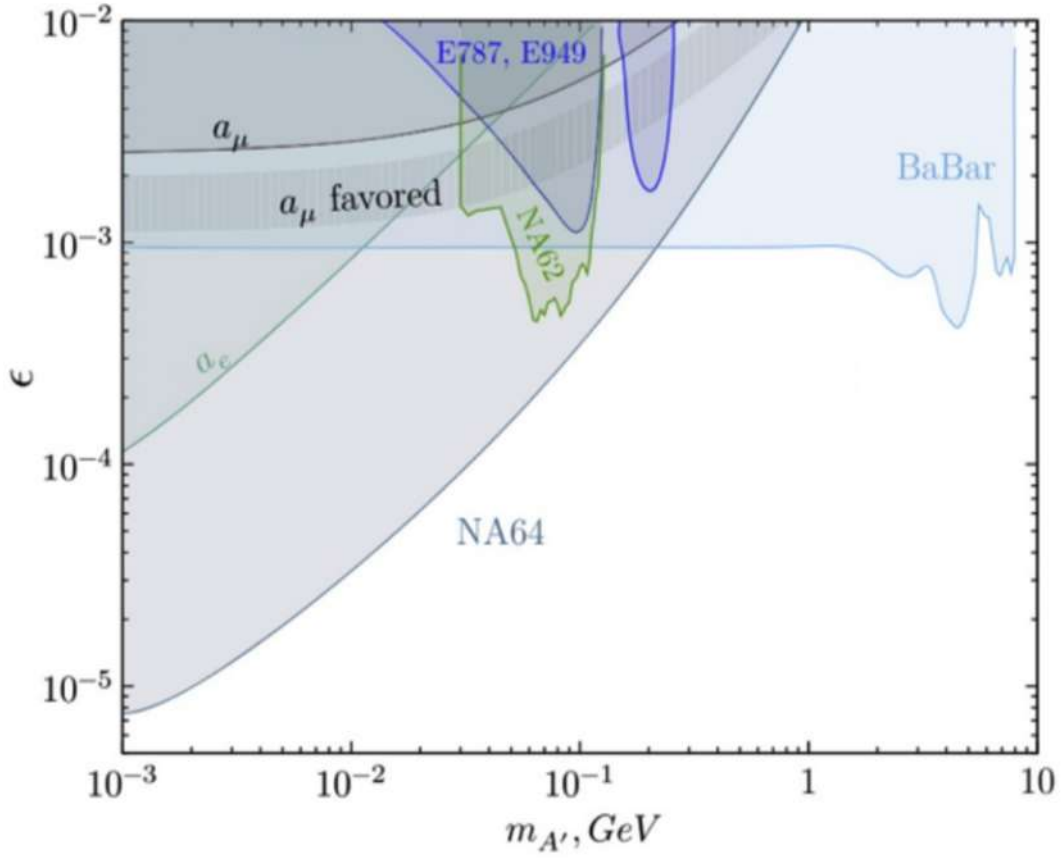
2 The Beryllium and Helium anomaly

SUMMARY OF THE CHAPTER. The ^{8}Be and ^{4}He anomalies appeared in a nuclear physics experiment performed at the Institute for Nuclear Research, Hungarian Academy of Science (MTA ATOMKI), in 2016 and 2018, respectively. The experiment study the Internal Pair Conversion of Beryllium and Helium excited nuclear states. A significant deviations was observed at large angles in the angular correlation of e^+e^- pairs first in ^{8}Be and later on ^{4}He. These anomalies were observed with a significant confidence level and may indicate, in an intermediate step, the creation of a new neutral particle with mass ~ 17 MeV. This particle has been named X17. Different theoretical interpretations, beyond the standard model, have been proposed and some of them are described at the end of the chapter.

2.1 The Internal Pair Conversion (IPC)

The Internal Pair Conversion (IPC) is an electromagnetic alternative decay mode of an excited nucleus, in competition with the photon emission and the atomic internal conversion [19]. The IPC spectroscopy has been studied for a long time, since the process has a reasonably high conversion coefficient, in the order of 10^{-4}-10^{-3}, for a wide range of energies and atomic numbers. The measurement of these coefficients provides an effective method for determining the multipolarity of electromagnetic transitions [20]. To measure the multipolarity of the electromagnetic transition, the angular distribution of the e^+e^- pair emitted via IPC is studied. Quantum Electrodynamics (QED) predicts that the angular correlation of the final state electron-positron pair peaks at $0°$ and decreases rapidly with the correlation angle (ϑ_{CoM}) in the Centre of Mass frame (CoM), when the process is mediated by a massless particle. Instead, if the decay occurs through the emission of a short-lived ($\tau \sim 10^{-13}$ s) neutral particle, the angular correlation will exhibit a peak at angles depending on the mediator mass. In the laboratory frame, the pair angular distribution is peaked at intermediate angles due to the

Lorentz boost and it provides a measurement for the mass of the intermediate state. In the laboratory frame, the invariant mass can be derived from the measurement of the relative angle ϑ and from the energy of the final state electron and positron. The invariant mass is given by [21]:

$$m^2 \simeq (1 - y^2)E^2 \sin^2 \frac{\vartheta}{2} + 2m_e^2\left(1 + \frac{1 + y^2}{1 - y^2}\cos\vartheta\right) + \mathcal{O}(m_e^4) \tag{2.1}$$

where $E = E_{e+} + E_{e-} + 1.022$ MeV is the transition energy, $y = \frac{E_{e+} - E_{e-}}{E_{e+} + E_{e-}}$ is the disparity, and $E_{e\pm}$ is the energy of final state particles in the laboratory frame.

A spectrometer with good energy and angular resolution is mandatory to study IPC processes. At the Institute for Nuclear Research of the Hungarian Academy of Science of Debrecen (MTA ATOMKI), an optimised multidetector system was build to perform such studies.

2.2 The ATOMKI experiment

The ATOMKI apparatus is designed to measure the IPC of excited nuclei obtained via proton capture of a target nucleus. The process under investigation is:

$$p + {}_{Z}^{A}\text{X} \rightarrow {}_{Z'}^{A'}\text{X}'^* \rightarrow {}_{Z'}^{A'}\text{X}' + e^+ + e^- \tag{2.2}$$
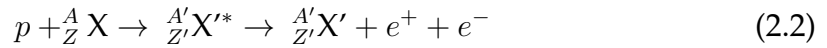
The first target used by the ATOMKI team was made of Lithium: ${}_{3}^{7}\text{Li}$, and the excited nuclear state produced was ${}_{4}^{8}\text{Be}$ whose de-excitation via IPC was studied. A schematic representation of the ATOMKI apparatus is shown in Fig. 2.1. The main components of the setup are: [22]:

- The **Proton beam** with energy tuned to 1.03 MeV to produce the resonance by means of the excitation of the target nuclei. The beam is produced by the 5 MV Van De Graaff accelerator with typical current of $1~\mu$A;

- The **Lithium target** installed perpendicular to the beam direction and mounted on 10 μm Al backings. It consits of a 15 μg/cm^2 thick LiF$_2$ evaporated target and a 300 μg/cm^2 thick LiO$_2$ evaporated target. A HPGe detector is installed at 50 cm from the target to veto the γ-ray of the ${}^7\text{Li}(p, p'\gamma)$ reaction, which has a very high cross section.

- The **Multi-detector-array spectrometer**. It is composed by five plastic $\Delta E-$

(a)

(b)
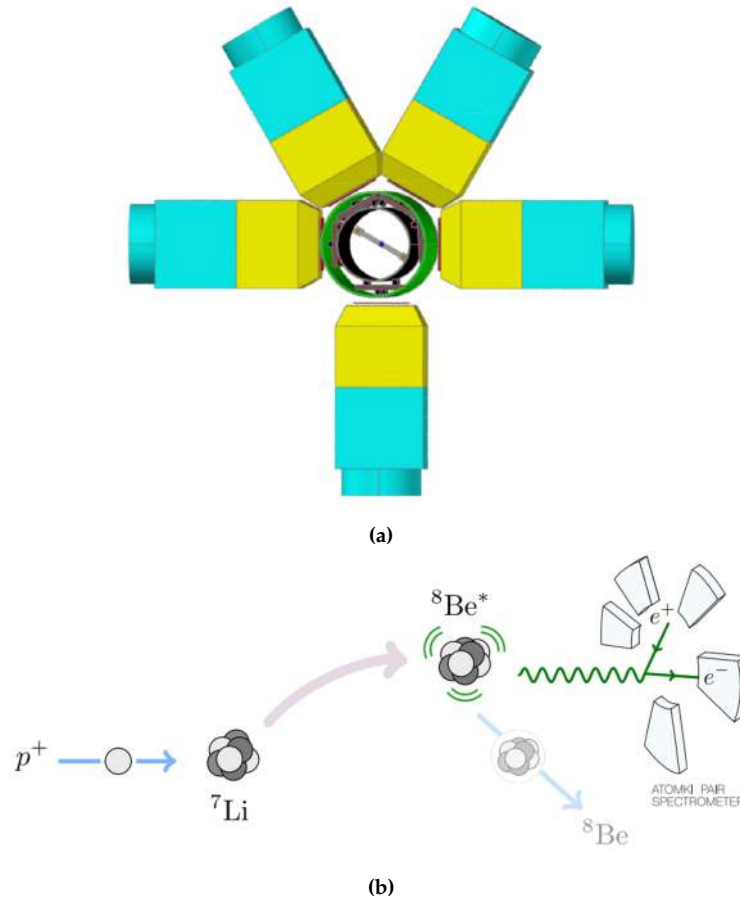
Figure 2.1: (a) CAD drawing of the e^+e^- ATOMKI spectrometer with five MWPCs and $\Delta E - E$ telescopes. The target is the blue spot in the centre. It is spanned between 3 mm thick Perspex rods to minimise the scattering and pair creation from the vicinity of the target. The beam pipe is shown in black around which the MWPCs are arranged. Their gas volume is closed by plastic foils having thickness (1 mm). The 1 mm thick ΔE detectors are shown in red, while the E scintillators in yellow with their light guides in cyan [22]. **(b)** A scheme of the ATOMKI experiment. The proton beam impinges on a Lithium target producing an excited Beryllium state which decays via IPC and the emitted pairs are detected with the 5 arms spectrometer [23].

E telescopes. The telescopes are used in combination with position sensitive detectors to increase spatial resolution. The ΔE detectors have dimensions $38 \times 45 \times 1$ mm^3 and the E detectors $78 \times 60 \times 70$ mm^3. They were placed in a plane orthogonal to the beam direction at azimuthal angles of $0°$, $60°$ $120°$, $180°$ and $270°$. These angles are chosen to obtain a homogeneous acceptance of the electron-positron pairs as a function of the correlation angle. The impact positions are measured by multi-wire proportional counters (MWPC), installed in front of the detectors;

A comparison with GEANT3 [24] simulations demonstrates that the angular correlation between $50°$ and $180°$ of this setup for electron-positron pairs in the energy range between 6 and 18 MeV can be determined with sufficient resolution

and efficiency.

2.2.1 First observation of the Beryllium Anomaly

In 2016 the ATOMKI collaboration focused on the study of electron-positron angular correlations for the ^{8}Be transition produced by excited states with spin-parity $J^P = 1^+$ and isospin $T = 0, 1$. The lowest excited states of ^{8}Be are characterised by different combination of spin-parity and isospin, as shown in Fig. 2.2. This early work focused only on the $J^P = 1^+$ states, labelled ^{8}Be$^{*\prime}$ and ^{8}Be* [8]. ^{8}Be$^{*\prime}$ state has isospin $T = 1$, energy $E = 17.64$ MeV and width $\Gamma = 10.7$ KeV, while ^{8}Be* state has isospin $T = 0$, energy $E = 18.15$ MeV and width $\Gamma = 138$ KeV.
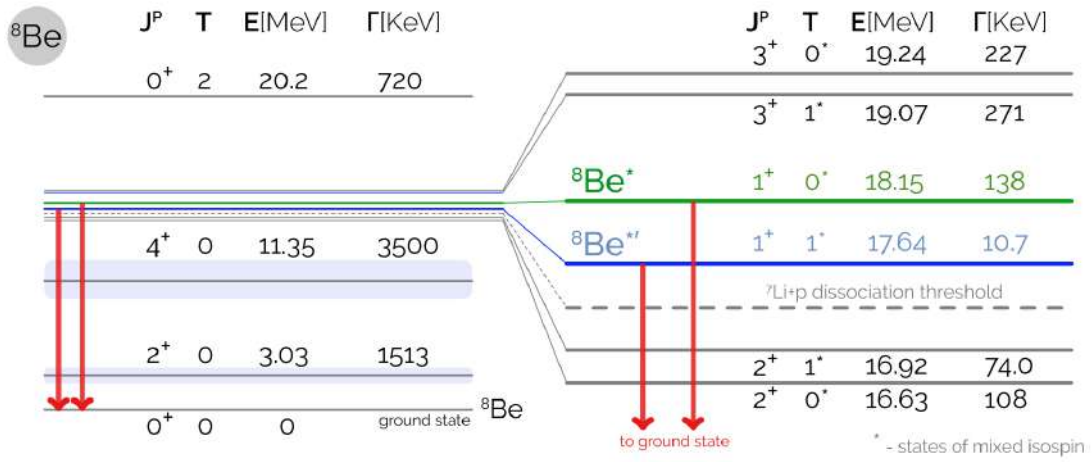
Figure 2.2: The most important ^{8}Be states. Each state is labelled with its the spin-parity J^P, isospin T, energy E, and decay width Γ from [25]. The "*" represents a state with a significant isospin mixing [23].

Both transitions showed an enhancement of e^+e^- pair production at large angles: the ^{8}Be$^{*\prime}$ at $\vartheta \sim 110°$ and ^{8}Be* at $\vartheta \sim 140°$.

The first anomaly was explained by the ATOMKI collaboration as a combination of different states, considering a mixed multipolarity transition. The deviation at $\vartheta \sim 110°$ was explained considering the de-excitation of a M1 transition mixed with a small E1 component from the background. The transition is purely M1, but at the resonant energy 17.64 MeV, there is a small, but not negligible, background component. This background contribution is due to the non-resonant direct proton capture, whose multipolarity is dominantly E1 and must therefore be added to the resonant transition. Since the width is very tiny, the background contribution is small and the combination which best fit the results is M1+2 % E1.

The ^{8}Be* anomaly shown in Fig. 2.3 is the most important for this thesis work. It shows the first significant IPC angular distribution anomaly. This in the laboratory frame peaks at $\vartheta = 140°$ and returns close to the SM predictions at $\vartheta = 170°$. Since this transition has a large width, it was considered affected by a large background contribution coming from different multipolarity states. Nevertheless, this explanation was not sufficient to justify the phenomenon.

Fig. 2.3a shows the Internal Pair Conversion Correlation (IPCC) as a function of the angle ϑ in the laboratory frame. The anomaly is present at the beam energy $E_p = 1.10$ MeV, that is the resonant energy. The peak has a significance of 6.8σ, then is reasonable to consider it as a resonant production of a neutral intermediate massive particle whose mass is derived by equation 2.1. The invariant mass distribution for the ^{8}Be* decay is shown (dots with error bars) in Fig. 2.3b. The dash-dotted line is the sum of the result of the simulation performed for M1+23%E1 mixed IPC transition and the distribution of the decay of a massive neutral particle with mass $M = 16.60$ MeV. The multipolarity combination has a large background term with respect the one associated to ^{8}Be*, which has a much smaller width. This graph shows the agreement with the experimental distribution and the simulated result, then the deviation in the angular distribution can be described by assuming the creation and subsequent decay of a boson with mass $M = 16.70 \pm 0.35(stat) \pm 0.5(syst)$ MeV with a confidence level $> 5\sigma$. The branching ratio of the process is:

$$\frac{\text{Br}(e^+e^- \to X)}{\text{Br}(e^+e^- \to \gamma)} = 5.8 \cdot 10^{-6} \tag{2.3}$$

for the best fit.

2.2.2 Second observation of the Beryllium Anomaly

After the first observation of the angular distribution anomaly, the ATOMKI apparatus underwent some upgrades to improve energy and angular resolutions, and to allow more reliable measurements on the ^{8}Be transition [26]. The new experiment was performed at the 2 MV Tandetron accelerator in Debrecen, which accelerated the protons to the resonant production energy of 1030 keV. The proton beam with the same current of the previous experiment impinged on a 300 μg/cm^2 thick Lithium target evaporated on a 20 μg/cm^2 thick Carbon foil. The target Alluminum support previously used, was replaced with a thinner one, made of ^{12}C and the number of telescopes was increased to 6 to improve the angular acceptance. The multiwire proportional counters were replaced with
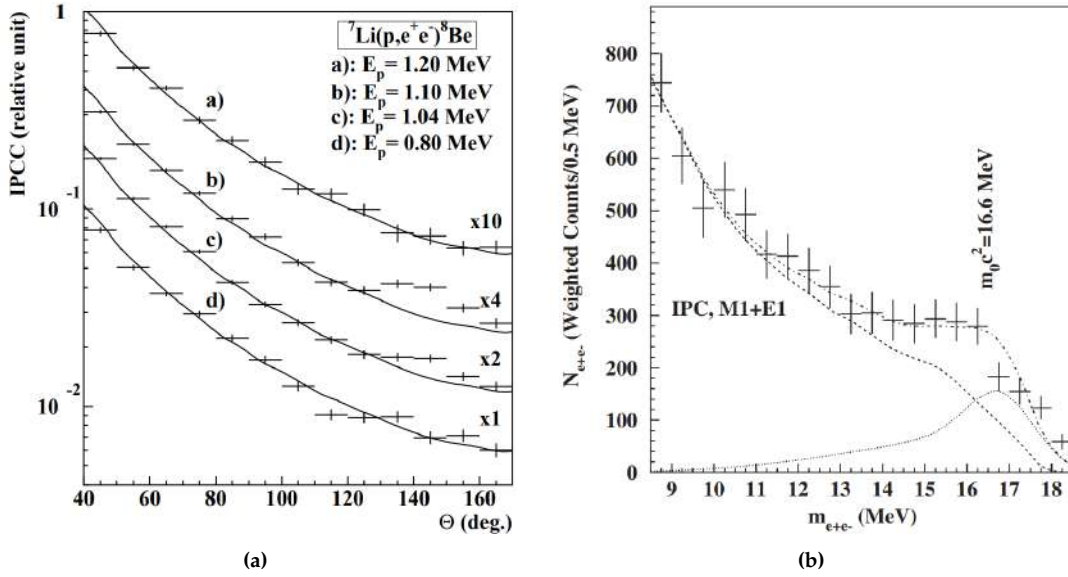
Figure 2.3: (a) The IPCC for each of the four different beam energies considered (E_p = 0.80, 1.04, 1.10, 1.20 MeV). The continuous lines are the simulated IPCC, taking into account M1+E1 mixed transitions. **(b)** The invariant mass distribution calculated from the measured energies and angles, and for the beam energy E_p = 1.10 MeV. The dots with error bars are the experimental results, the dashed line is the simulated distribution which takes into account M1+E1 mixing, the dotted line is the distribution of the decay of a particle with mass M = 16.6 MeV and the dash-dotted line is the sum of them [8].

double-sided silicon strip detectors (DSSD), with strips of width 3 mm. The plastic scintillator telescopes had dimensions $82 \times 86 \times 80$ mm^3 and they were installed orthogonally to the beam direction at azimuthal angles $0°$, $60°$ $120°$, $180°$, $240°$ and $300°$.

Fig. 2.4 shows the angular correlation of the electron-positron pairs resulting from the 18.15 MeV ^{8}Be excited state decay, measured in the previous (blue) and in the new (red) experiment. The black curve represents the background and the green one is the fit to the new experimental points also including a particle decaying e^+e^-. The second measurement confirms the signal of the new X17 particle and constrains its mass (M = 17.01(16) MeV). The branching ratio, compared to the γ-decay, is found to be $6(1) \cdot 10^{-6}$ [26].

Figure 2.4: Angular correlations of the e^+e pairs originated from the decay of the 18.15 MeV excited ^{8}Be state, of the first ATOMKI measurement (blue) and of the new one (red). The black line represents the background, while the green one is the fit to the red dots performed with a function considering both the signal and the background [26].

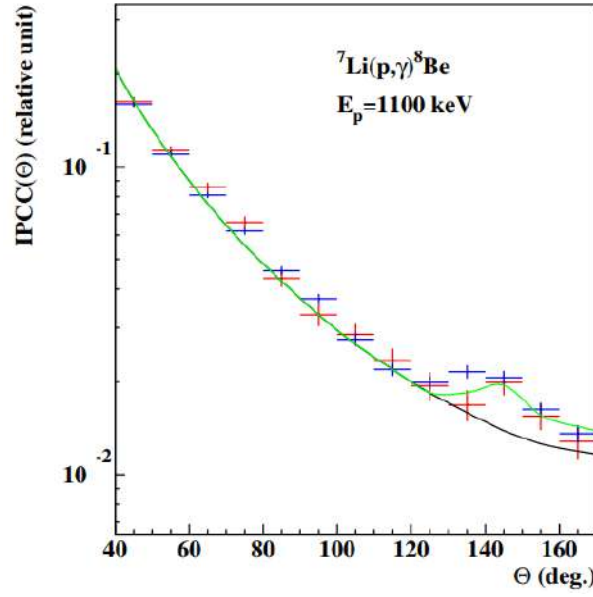## 2.2.3 The Helium Anomaly

More recently, the IPC anomaly was observed from the electro-magnetically forbidden M0 transition depopulating the 21.01 MeV $J^P = 0^- \to 0^+$ state in ^{4}He and 20.21 MeV $J^P = 0^+ \to 0^+$ state in ^{4}He. The transition was probed bombarding the target with a proton beam with energies $E_p = 510, 610, 900$. The IPC angular distribution showed enhancements in correspondence of each of the beam energies with consistent significance. The anomalies could be explained with the emission of a $M \simeq 17$ MeV vector boson ($J^P = 1^+$) or a pseudoscalar particle ($J^P = 0^-$), according with the results obtained by the ^{8}Be observation [9, 27].

The experiment was carried out by the ATOMKI group, with the same detector of the second ^{8}Be observation [26] and the same accelerator, the 2 MV Tandetron accelerator. The $E_p = 510, 610, 900$ KeV proton beam impinged on a ^{3}H target for about 100 hours for each bombarding energy. The ^{3}H was absorbed in a 4.2 g/cm^2 thick Ti layer evaporated onto a 0.4 mm thick Mo disc. The density of the ^{3}H atoms was $2.66 \cdot 10^{20}$ atoms/cm^2.

The bombarding energy was below the threshold of the (p, n) reaction ($E_p < E_{th} = 1.018$ MeV), and excited the ^{4}He nucleus to the $E = 20.49, 20.29, 20.21$ MeV intermediate states, which are between the first and second excited states. The second 0^- excited state in ^{4}He, located at $E = 21.01$ MeV, has a wide width ($\Gamma = 0.84$ MeV), and then it overlaps the first ^{4}He excited state ($J^P = 0^+$, $E =$

20.21 MeV and $\Gamma = 0.50$ MeV) [28]. Thus, the spectrum of the e^+e^- pairs comes from the de-excitation of all of the three intermediate states, that belong to the two different spin-parity states.

Fig. 2.5a shows the angular correlation of the electron-positron pairs emitted via IPC with each of the three beam energies (markers with error bars), and the respective background (histograms). The large angle enhancement is present for each beam energy. Fig. 2.5b shows the experimental angular distribution of the IPC emitted pairs at each positron energy considered after the subtraction of the associated background (the histogram in Fig. 2.5a). These results confirm the anomaly observed in the ^{8}Be analysis, namely the production and subsequent decay of a massive boson. The mass, the Branching Ratio and the significance of all three peaks in Fig.2.5 are collected in Table 2.1
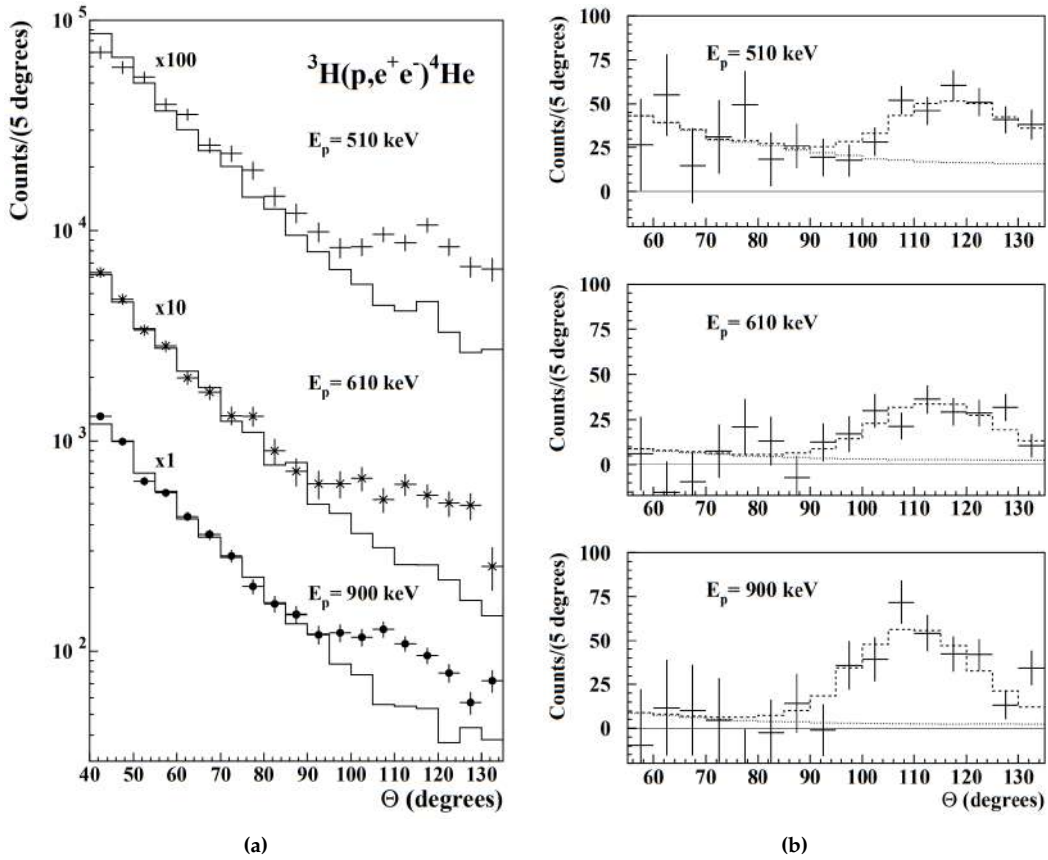
Figure 2.5: (a) The angular correlation of the e^-e^+ pairs emitted in the de-excitation of ^{4}He. The markers with the error bars are the experimental results of the ^{3}H$(p,\gamma)^4$He reaction at $E_p = 510, 610, 900$ KeV beam energy and the respective fitted background (continuous line histograms). **(b)** The angular correlation of the e^-e^+ pairs after the subtraction of the background showed in **(a)**. [27]

Recently, the anomaly has been further confirmed by a new study of the ^{7}Li$(p, e^-e^+)^8$Be direct proton-capture reaction [29] and by a preliminary results of the ^{12}C excited transitions study, reported in [30].

E_p [keV]	IPCC ($\times 10^{-4}$)	Br_{X17} ($\times 10^{-6}$)	Mass [MeV/c^2]	Confidence
510	2.5(3)	6.2(7)	17.01(12)	7.3σ
610	1.0(7)	4.1(6)	16.88(16)	6.6σ
900	1.1(11)	6.5(20)	16.68(30)	8.9σ
Averages		5.1(13)	16.94(12)	
^{8}Be		6	16.70(35)	

Table 2.1: The summarising results table. The Table shows the IPCC, the X17 branching ratio (with respect the photon production), the mass ocf the X17 particle and the confidence derived from the fits [27].

2.3   Nuclear physics explanations

After the ^{8}Be anomaly observation, possible nuclear physics based explanations of the phenomenon were explored by Zhang et al. [31]. The tempted approach was based on the presence of possible interference terms in the multi-polarity transitions, and on a model founded on the so-called Halo Effective Field Theory [32], which also includes Form Factors (FF) for the coupling vertex. The interference terms are originated, when evaluating the full Lagrangian of the e^+e^- pair production, by the M1, E1 and E2 multipole terms. The interference terms [31] caused a re-modulation of the angular distribution, and needed to be accounted for in the nuclear physics background estimate of the experiment. Two possible sets of Form Factors were considered in a simulated e^+e^- angular correlation which included M1 and E1 transitions, and both were not in agreement with the experimental results.

In the end, this nuclear physics analysis of the ^{8}Be anomaly did not justify the 18.15 MeV peak, but it pointed out that the correct multipolarity mixing for the transition was M1+50%E1, in contrast with the values quoted by ATOMKI in their 2016 analysis.

In 2020 an other possible nuclear physics explanation was provided to justify the results obtained by the ^{4}He anomaly observations, which carried out two possible interpretation of the X17. The nuclear physics model used, was based on the conjecture made in [33] that the vector boson must be protophobic (the protophobia concept will be explained in the next sections). The protophobic vector boson explanation was studied by deriving an isospin relation between photon and X17 couplings to nucleons (and quarks). The explanation led to the conclusion that the X17 production is dominated by direct capture transitions both in ^{8}Be and ^{4}He without going through any nuclear resonance. The explanation also predicted a smooth energy dependence that occurs for all proton beam energies above the threshold [10]. The Helium results at different beam energies agrees

with this nuclear explanation.

Even if some nuclear physics explanations were partially accounting for the anomalous effects observed, interpretations Beyond Standard Model were also carried out. We will discuss a few of them in the next section.

2.4 Beyond Standard Model explanation

The X17 boson interactions may respect chirality and requires a discussion on the parity symmetry. The nuclear processes involving the same spin states, but opposite parity, typically proceed trough different partial waves, and since the X17 is produced most semi-relativistically, the decay of a mixed state is likely to be dominated by a single parity component [9]. From this statement, the possible theoretical explanations of the X17 imply that this is a boson with a definite parity. The nuclear decays are labelled as $N_* \rightarrow N_0\ X17$ where N_* is the excited nucleus and N_0 is the ground state nucleus.

The spin-parity of N_*, N_0, and X17 are denoted by $J_*^{P_*}$, $J_0^{P_0}$ and $J_X^{P_X}$, respectively, and the parity and angular momentum conservation imply:

$$J_* = L \oplus J_0 \oplus J_X \tag{2.4}$$

$$P_* = (-1)^L P_0 P_X \tag{2.5}$$

where L is the final state orbital angular momentum, and $\oplus$ is used to sum the angular momentum.

The considered ^{8}Be excited state is a $J_*^{P_*} = 1^+$, with $E_p = 18.15$ MeV, and spin-parity conservation laws lead:

$$1 = L \oplus J_X \tag{2.6}$$

$$+1 = (-1)^L P_X. \tag{2.7}$$

These relations imply that if $J_X = 0$, then $L = 1$, and $P_X = 1$, the X17 can not be a scalar, but it can be a pseudoscalar produced in P-wave. If $J_X = 1$, then $L = 0,\ 1,\ 2$, and $P_X = +1,\ -1,\ +1$, respectively, and X17 can either be a vector produced in P-wave, or an axial vector produced in S- or D-wave. In the case of the ^{12}C [30], the excited state is characterised by $J_*^{P_*} = 1^-$ and $E = 17.23$ MeV, then the parity considerations are reversed with respect the ^{8}Be (scalar $\leftrightarrow$ pseudoscalar and vector $\leftrightarrow$ axial vector).

The considered ^{4}He excited states have $J^P = 0^-$ ^{4}He(21.01 MeV) and the $J^P = 0^+$ 4He(20.21 MeV), and they presented the anomalies coming from the 20.49 MeV intermediate state. For the 0^- excited state, the conservation laws require

$$0 = L \oplus J_X \tag{2.8}$$

$$-1 = (-1)^L P_X. \tag{2.9}$$

If $J_X = 0$, then $L = 0$, and $P_X = 1$: X17 cannot be a scalar, but it can be a pseudoscalar produced in S-wave. If $J_X = 1$, then $L = 1$, and $P_X = +1$: X17 can not be a vector, but it can be an axial vector produced in P-wave state. Note that if X17 can not be a vector gauge boson, then the symmetries also forbid decays to single photon for this transition. For the 0^+ excited state, the parity is reversed, then all the results obtained for the 0^- state must be reversed (scalar $\leftrightarrow$ pseudoscalar and vector $\leftrightarrow$ axial vector).

The spin-parity study results are synthesised in Table 2.2. All four J_*^P transitions up to spin 1 are considered and these results can be applied to many other nuclear decays. In principle, comparing results from different excited nuclei, one can determine if two signals can be attributed to the same X17 boson, and constrain the possible spin-parity assignments of the X17 boson.

N_*	J_*^P	Scalar X17	Pseudoscalar X17	Vector X17	Axial Vector X17
^{8}Be(18.15)	1^+	✗	✓	✓	✓
^{12}C(17.23)	1^-	✓	✗	✓	✓
^{4}He(21.01)	0^-	✗	✓	✗	✓
^{4}He(20.21)	0^+	✓	✗	✓	✗

Table 2.2: Nuclear excited states under study, with the associated spin-parity. The "✓" ("✗") defines whether it is possible (impossible) to explain the X17 particle, respecting the conservation of angular momentum and parity. The possibilities for X17 allowed are: scalar, pseudoscalar, vector and axial vector (for their full derivation, see [9, 23]).

In this thesis work I will focus on the vector boson explanation [9, 23, 33], showing some properties of the X17 boson, and focusing on the protophobia of the vector boson. This property is required to satisfy the limit on the coupling to the quark imposed by the experimental result of the NA48/2 experiment [34].

In order to claim that the X17 is a real new particle, one or more experiments are needed reproducing the ATOMKI results on the Beryllium and Helium anomaly. In many laboratories (LNL, LNGS, PSI) different nuclear physics collaborations

are preparing experimental campaigns. The most advanced is the MEG-II exper-
iment at PSI Institute in Zurich [35]. Meanwhile, if the X17 boson is a particle
with a strong lepton coupling, it must be produced in e^+e^- annihilations. The
PADME experiment is a suitable candidate to perform this measurement, since
the experiment studies electron-positron reactions, with the possibility to set the
initial state's energy in the desired resonant range with significant precision.

3 The PADME experiment at LNF

SUMMARY OF THE CHAPTER. PADME (Positron Annihilation into Dark Matter Experiment) is an experiment conceived to detect a signal of a dark photon A' produced in the annihilation of positrons with the electrons of a target. PADME is installed at the Beam Test Facility (BTF) of the Laboratori Nazionali di Frascati (LNF) that provides the positron beam. This thesis work aims at defining the possible outcomes of PADME *Run III*, starting beginning of September 2022, meant to produce the X17 boson resonantly via e^+e^- annihilation. In this chapter, I describe the apparatus, and I compare the X17 setup with that previously used to look for the dark photon.

3.1   The Beam Test Facility at LNF

The BTF provides beams of electrons or positrons coming from the LINAC of DAΦNE complex [36, 37]. These can have variable energy, multiplicity and pulse time duration. Positrons are produced from the interaction of the electrons with high Z converters. The position of the converters along the beam line sets the beam and its specifics:

- a Tungsten-Rhenium (T-Re) target of $2X_0$ thickness, located after the first five accelerating sections, produces the so-called "primary positron beam";

- a Copper (Cu) target of $1.7X_0$ thickness, located on the BTF extraction beam-line, produce the so-called "secondary positron beam".

A scheme of the beam line is shown in Fig. 3.1 and the specifics of the beam are collected in Table. 3.1.

PADME is installed in BTF hall 1 (BTF-1). The positron beam of the experiment can be either primary or secondary. In the second case the maximum energy is $E_{beam} = 550$ MeV. The positron bunch length is ~ 250 ns and the repetition rate is 50 Hz. Actually, one of the 50 bunches is sent to a hodoscope for energy measurement.

Specifics	e$^-$	primary e$^+$	secondary e$^+$
Maximum beam energy [MeV]	800	490	550
RF frequency [MHz]	2856	2856	2856
Beam pulse lenght [ns]	1-300	1-300	1-300
RMS energy spread	0.56	< 0.96	0.96
LINAC repetition rate [Hz]	1-50	1-50	1-50
Emittance [mm mrad]	1	~ 1	~ 1
Divergence [mrad]	1-1.5	1-1.5	1-1.5

Table 3.1: BTF beam specifics [38].
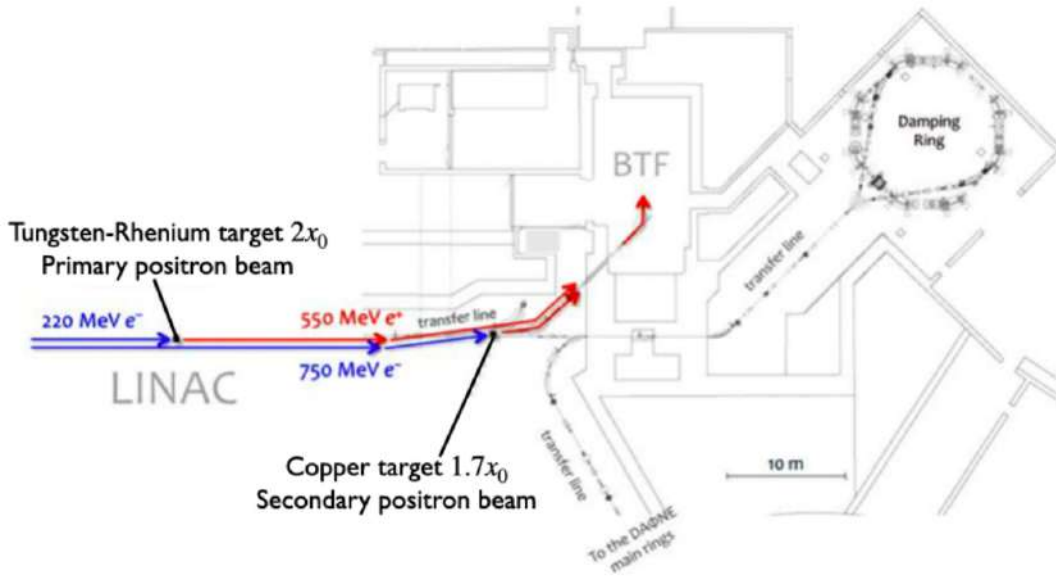
Figure 3.1: The BTF transfer line with the two positron beam configurations: LINAC primary positron beam from the Tungsten-Rhenium converter and the secondary positron beam from the BTF Copper target [38].

3.2 The PADME apparatus

The goal of the PADME experiment is to search for a dark photon A', produced in the annihilation of the positrons with the electrons of a fixed target, together with a recoil photon [39]. The reaction under study is $e^+e^- \to \gamma A'$. The production of an A' is searched in final states with a single photon studying the missing mass distribution, which is given by:

$$MM(A')^2 = (P_{e+} + P_{e-} - P_\gamma)^2 \tag{3.1}$$

where P_i are the four-momenta of the visible particles. The missing mass will show a peak in correspondence of the A' mass. This method does not make any assumption on the A' decay modes (visible or invisible) therefore it is model independent. The PADME detector consists of the following components [38]:

- The **Active Diamond Target** able to determine the multiplicity and the impinging position of the positron beam;

- The **dipole magnet** bending out of the calorimeters the non-interacting positrons and those interacting in the acceptance of the veto system;

- The **charged particle veto system** to detect charged particles resulting from the beam-target interaction. The veto system is composed by three stations: the positron veto (PVeto), the electron veto (EVeto) and the high energy positron veto (HEPVeto);

- The **Vacuum chamber** to avoid the interaction of initial and final particles with the air molecules;

- The **Electromagnetic Calorimeter** (**ECAL**) to measure the energy and direction of photons from annihilation processes. ECAL has a central hole to allow Bremmstrahlung photons to pass through;

- The **Small Angle electromagnetic Calorimeter** (**SAC**) placed behind the central hole of ECAL. Its main goal is to reject the Bremmstrahlung background photons which are emitted at small angle.

Fig. 3.2 shows a schematic top view of the experiment with all the components previously mentioned. The positron beam, coming from BTF, is lying on the z axis, and enters from the left side of the figure. The picture also shows the trajectories of positrons, that having lost energy for Bremmstrahlung, are bent by the dipole magnetic field. During PADME *Run III* the dipole magnet will be turned off to allow the detection with ECAL of e^+e^- pairs resulting from X17 decay. Furthermore, to distinguish these pairs form 2γ events, a new detector consisting of scintillator slabs (ETagger), will be installed in front of ECAL. Further details on ETagger are given in section 3.3.

3.2.1 The Active Diamond Target

The PADME target is a full carbon device, made of a policrystalline diamond film (thickness $100~\mu$m and area of 2×2 cm^2). It has been realised at the Universitá del Salento in collaboration with INFN Lecce. The target material has been chosen because the main background contribution to the experiment is represented by Bremmstrahlung proportional to Z^2. Then, a material with low Z maximise the signal-to-noise ratio. The target has also to be thin to reduce the pile-up events.
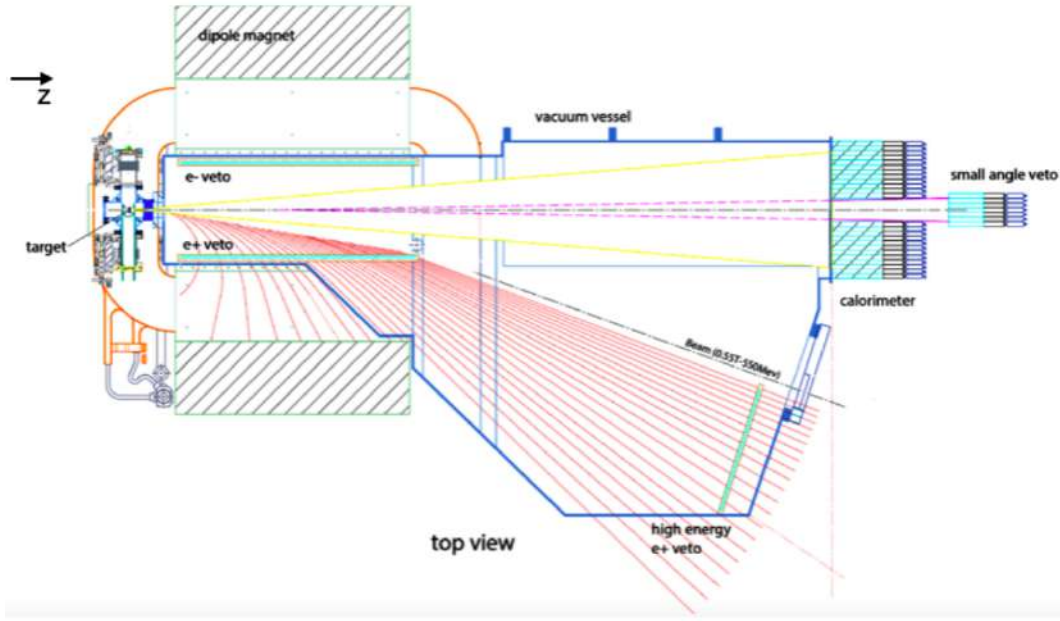
Figure 3.2: Schematic representation of the PADME apparatus used during *Run I* and *II* [40].

The denomination "active" is due to its capability to measure the beam interaction point and multiplicity performed through 16 strip electrodes, realised with a laser technique on both target surfaces. The strips (width 0.85 mm, pitch 1 mm) realised on the opposite target sides are oriented in orthogonal directions to allow bi-dimensional measurements [40, 41].

3.2.2 The dipole magnet

The dipole magnet is placed after the target and has the task of bending out of the detector acceptance, the positrons that do not interact with the target. The magnet has a length of 1 m, a width of 52 cm, and a gap of 23 cm. The magnet has been obtained from CERN where it was a spare part for SPS transfer line [42]. The relation between the current I and the magnetic field central value B is:

$$B\,[\mathrm{G}] = 19.44I\,[\mathrm{A}] + 32.801. \tag{3.2}$$

3.2.3 The charged particle veto system

PADME needs a veto system to reject background events due to charged particles produced in the beam-target interaction. Since the background is dominated by positron Bremmstrahlung in the target, the veto is designed to identify mainly this processes. The detector consists of plastic scintillator bars (184 mm long and with 10×10 mm^2 transverse area) arranged in 3 stations:

- positron veto (PVeto): array of 90 scintillating units;

- electron veto (EVeto): array of 96 scintillating units;

- high energy positron veto (HEPVeto): array of 16 scintillating units.

The scintillating material is polystyrene-based with $1.5\,\%$ concentration of $C_{24}H_{16}N_2O_2$ (POPOP). Each bar hosts a wavelength shifter fibre glued along its length. The bars are placed vertically, with respect the beam direction, and their scintillating light is readout by means of silicon photomultipliers, from one side for the PVeto and EVeto, from both sides for the HEPVeto. The veto stations are located inside the vacuum chamber: the PVeto and EVeto are installed inside the magnet symmetrically with respect to the beam axis; the HEPVeto is placed transversely to the bent positron beam. The veto bars time resolution is 0.67 ns, small enough to resolve interactions occurring in the same bunch [43].

3.2.4 The Vacuum chamber

The energy range of the particles of the PADME experiment is quite low (< 500 MeV). Therefore, particle's interaction with air can compromise the success of the experimental measurements. The radiation length of air at normal temperature and pressure is $X_0 = 285$ m and the distance target-calorimeter is $\Delta L = 3.5$ m, then the atmospheric air thickness is $1.2\,\%X_0$, much larger than the thickness of the target itself ($0.04\,\%X_0$). The PADME vacuum chamber is attached to the BTF beam line and contains the target and all the three veto detectors.

3.2.5 The Electromagnetic Calorimeter (ECAL)

The main detector of PADME is the electromagnetic calorimeter (ECAL), shown in Fig. 3.3. Its main purpose is to detect the photons coming from the beam-target interaction. It measures their energy and impact position. ECAL has an energy resolution of about $\sim 3\,\%$ for photons with energy between 100 MeV and 1000 MeV and a cluster position resolution of 3 mm. It is a segmented calorimeter, made of 616 Bismuth Germanate (BGO) crystals, with a mass density $\rho = 7.13$ g/cm^3, a radiation length $X_0 = 7.97$ g/cm^2 and a Moliere radius $R_M = 2.23$ cm. Each crystal has dimension $2.1 \times 2.1 \times 23$ cm^3 and they are arranged in a cylindrical shape with a central squared hole of 5×5 cm^2 area and an external radius of ~ 30 cm (see Fig. 3.3a). Considering the geometry of ECAL the electromagnetic shower is fully contained along the longitudinally direction,

but only $\sim 70\%$ is contained along the transversal plane due to the dimension of the crystal [44, 45].

The central square hole is needed to avoid the overwhelm of the central crystals with photons produced in the forward direction (mainly via Bremmstrahlung). These particles are detected using the Small Angle Calorimeter installed behind the ECAL and covering its hole. To minimise the light crosstalk each crystal is covered by a reflective white paint and by a $50~\mu$m thick sheet of black Tedlar. The scintillation light is converted in an electronical signal by a photomultiplier with diameter 19 mm.

BGO material is sensitive to temperature changes: the amount of light collected changes of $-0.9~\%/$°C, then to record the temperature of the detector 40 temperature sensors are attached to some scintillating units [44, 45].
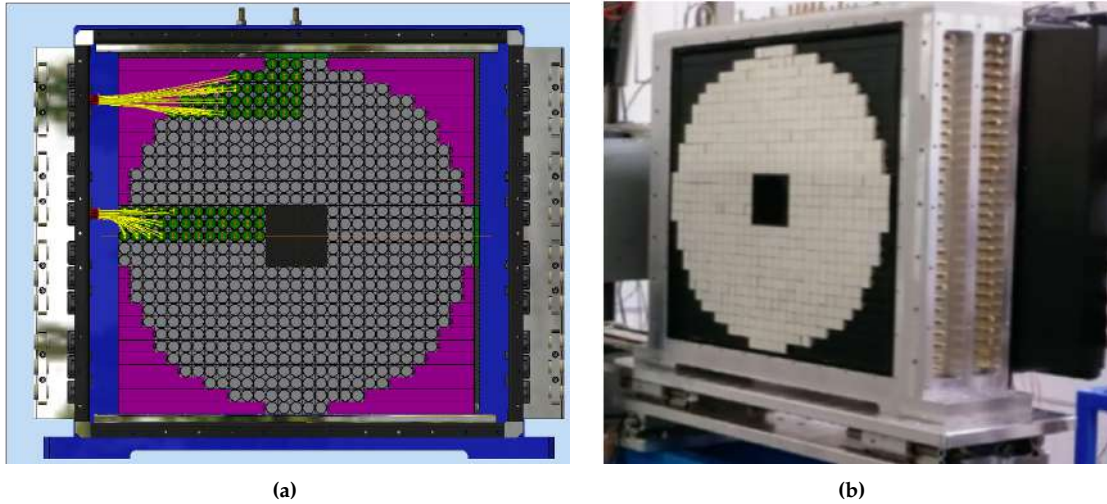
Figure 3.3: (a) The PADME electromagnetical calorimeter CAD drawing. **(b)** A pictur of the PADME electromagnetical calorimeter during the mounting phase [38].

3.2.6 The Small Angle electromagnetic Calorimeter

The Small Angle electromagnetic Calorimeter (SAC) is needed to detect background photons produced in the forward direction. Their expected rate of $\sim$MHz can not be stand by the main ECAL since BGO has a light decay time of ~ 300 ns. The SAC is installed behind the central hole of ECAL and it is a 5×5 PbF$_2$ matrix of crystals, each with a length of 140 mm and area 30×30 mm^2. It is covered by a $50~\mu$m thick sheet of Tedlar to screen it from external light. The PbF$_2$ has a decay time constant ~ 10 ns sufficient to reject background photons [46].

3.2.7 The beam monitor

PADME has two silicon pixel detectors to monitor the beam: MIMOSA and TimePix3. The first has a dimension of 1.921×1.987 cm^2 and it is based on a monolithic detector consisting of 928×960 pixels of 20.07 μm pitch [47]. The MIMOSA detector is placed in the same vacuum of the target and works at low bunch multiplicity. The TimePix3 is a hybrid Silicon pixel detector [48] and it is placed outside the vacuum chamber to monitor the non-interacting positrons. The detector consists of 12 sensors, each made of a 256×256 pixels matrix with an area of 14×14 mm^2.

3.3 Introduction to *Run III*

The PADME *Run III* is approved to begin in September 2022 and it is dedicated to the search of the X17 boson. The X17 production (shown in Fig. 3.4) is expected to occur via the positron annihilation with an electron of the target, and will be detected measuring its decay in e^+e^-

$$e^+e^- \rightarrow X17 \rightarrow e^+e^-. \tag{3.3}$$

Since the X17 mass is supposed to be around ~ 17 MeV, the X17 resonant production can occur setting the beam energy at ~ 282 MeV, corresponding to an invariant mass $\sqrt{s} = \sqrt{2m_e E_{beam}} = M_{X17}$. Actually, an invariant mass scan will be done varying the beam energy in steps of few MeV, and looking for an enhancement of the annihilation cross section, in correspondence to the centre of mass energy of the X17.
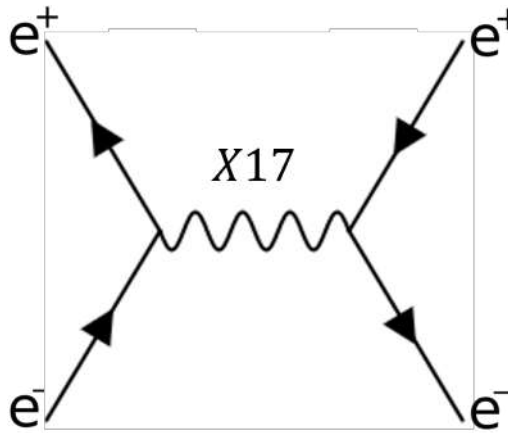
Figure 3.4: Feynman diagram of electron-positron annihilation producing a X17 boson, subsequently decaying into e^+e^-.

To do this measurement, the PADME apparatus undergoes some changes:

- the dipole magnet is switched off to allow the e^+e^- pairs coming from the annihilation process to enter into the geometrical acceptance of ECAL;

- in front of the electromagnetic calorimeter a new detector (Electron Tagger) made of plastic scintillators is installed;

- the SAC is replaced by the TimePix3 detector.

The new ETagger, made of scintillating material BC-408 [49], consists of 12 long slabs 660×44 mm^2 and 6 short slabs 265×44 mm^2. They are arranged to have a central hole 132×132 mm^2 which is slightly bigger than the calorimeter's hole. Fig. 3.5 shows the ETagger geometry and mechanical frame. The new detector is needed to distinguish the final states with an electron-positron pair, before they enter into ECAL where energy and impact position are measured. The calorimeter can measure e^+e^- energies and angles with an accuracy of 3 %, to allow precise reconstruction of the invariant mass pair.

(a)

(b)

Figure 3.5: (a) Picture of the ETagger scintillating matrix during the installation phase and **(b)** the scheme of its mechanical structure.

4 The SM background events

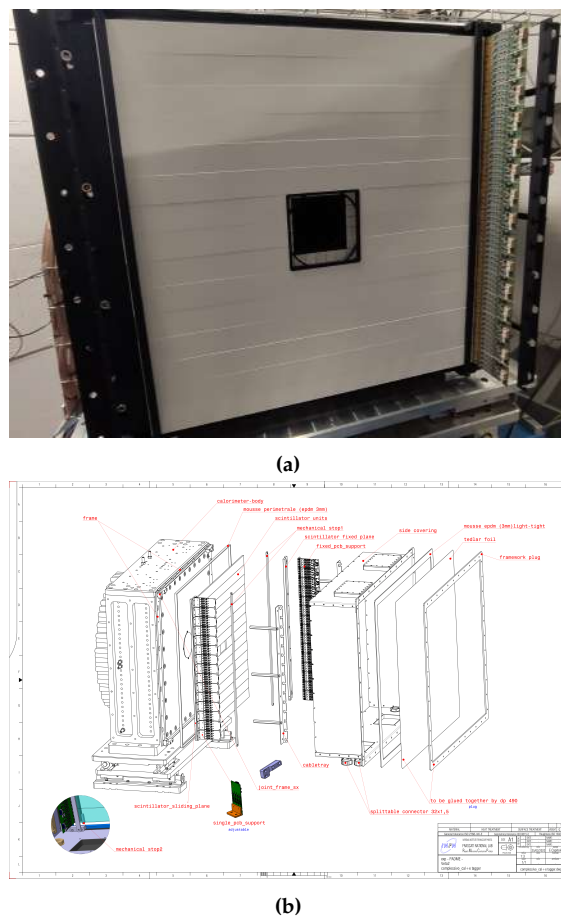SUMMARY OF THE CHAPTER. In this chapter I study analytically the SM background to the X17 resonant production. The positron electron interaction results mainly in two different processes: the Bhabha Scattering, characterised by the same particles of the initial state, and the $\gamma\gamma$ production. The Bhabha scattering occurs through an annihilation process and a scattering process, both mediated by a photon, which is virtual in the second case. I show how to derive the analytic cross sections and I compare them with the obtained through CalcHEP simulations.

4.1 The Bhabha scattering

The Bhabha scattering is a tree level QED process involving a positron and an electron:

$$e^+ + e^- \to e^+ + e^- \tag{4.1}$$

it occurs through two different channels, the *T-channel*, which is the scattering process, and *S-channel*, the annihilation one. *T* and *S* are referred to the Mandelstam variables, which are the squared sum of the combination of two of the four-momenta in a two bodies scattering process. In Fig. 4.1 is represented a generic two bodies scattering process with initial four-momenta p_1 and p_2 and final four-momenta k_1 and k_2. Since there are three different combinations of sums of these four-momenta, the Mandelstam variables are three, one for each combination. They are s, t and u and their definitions are:

$$
\begin{aligned}
s &= (p_1 + p_2)^2 = (k_1 + k_2)^2 \\
t &= (p_1 - k_1)^2 = (p_2 - k_2)^2 \\
u &= (p_1 - k_2)^2 = (p_2 - k_1)^2.
\end{aligned}
\tag{4.2}
$$

During the analysis, I want to treat the two Bhabha channels as two different and independent processes. In principle this could not be done because there is an interference term that appears when calculating the total cross-section, but I will show in later chapters, this is negligible. Also, I am interested to the Bhabha
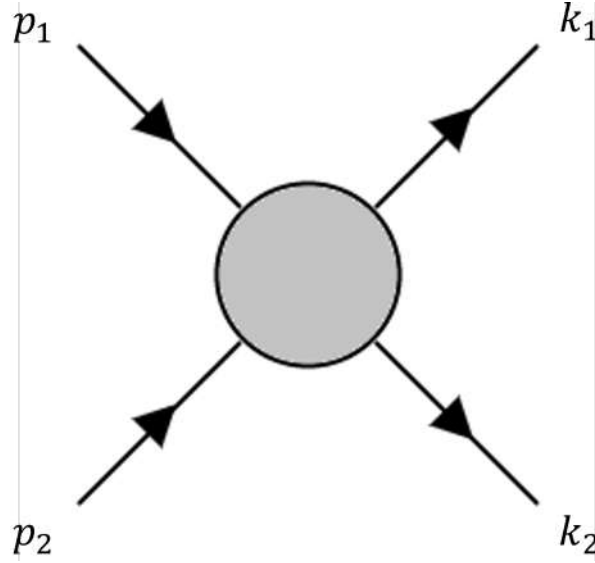
Figure 4.1: Two bodies in two bodies process. p_1 and p_2 are the initial four-momenta and k_1 and k_2 are the final four-momenta.

T- and S- channel cross section separately, since I want to understand how the particles are distributed in the PADME calorimeter as a function of the type of process that produced them. Furthermore, I am interested in the behaviour of the S-channel process, since at a given invariant mass, it will be similar to a heavy boson production such as the X17. I derive the tree level analytic cross section of each process considering the Feynman rules, associating all Feynman propagators with the respective components of the diagrams, that are needed to make perturbative calculations. Introducing the Feynman rules (see Appendix A), I can derive the transition matrix element of each process, including the allowed $e^+e^- \to \gamma\gamma$ process, which will be studied in next sections.

The cross section of two-bodies in N-bodies scattering or annihilation process is:

$$d\sigma = \frac{1}{4\sqrt{(p_1 \cdot p_2)^2 - m_1^2 m_2^2}} |\mathcal{M}|^2 d\Pi_{LIPS} \tag{4.3}$$

The square root at the denominator is the relative velocity between the two initial particles, whose four-momenta and masses are p_1, m_1 and p_2, m_2. In my case, the masses are both equal to the electron mass, then $m_1^2 m_2^2 = m_e^4$. $d\Pi_{LIPS}$ is the *Lorentz Invariant Phase Space*, where are encoded the energy and four-momentum conservation laws, and whose expression is:

$$d\Pi_{LIPS} = \prod_{f=1}^{N} \frac{d\boldsymbol{p_f}}{(2\pi)^3} \frac{1}{2E_f} (2\pi)^4 \delta^4 \left(\sum_f p_f - \sum_i p_i \right). \tag{4.4}$$

(for the full derivation of this expression, I referred to *The Quantum theory of Fields* of S. Weinberg [50, p. 134-141]).

To be noticed: I will consider $c = \hbar = 1$ during all of the calculations.

Finally, I will show how CalcHEP works, and I will compare the analytic results with the one obtained through CalcHEP simulations. I do this check, not only for the energy range associated with this study, but also for those related to previous experiments [51]. Using this software, I get also simulated events that are needed for my analyses.

4.1.1 The Scattering process

The *T-channel* is a process mediated by a virtual photon, it is represented in Fig. 4.2 where p_i are the initial four-momenta, k_i are the final four-momenta and s_i, r_i are the spin polarization of the particles. *T* refers to the Mandelstam variable of
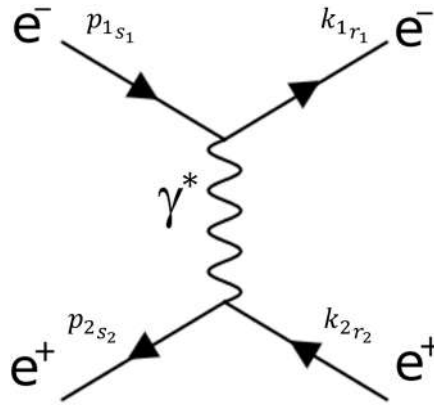
Figure 4.2: Feynman diagram of Bhabha scattering's T-channel

equation 4.2, which corresponds to:
$$t = (p_1 - k_1)^2 = 2m_e^2 - 2p_1 \cdot k_1 = 2m_e^2 - 2p_2 \cdot k_2 = (p_2 - k_2)^2$$
for this process.

I derive the transition matrix element related to the Fig. 4.2 using the Feynman rules (see Appendix A).

$$\imath\mathcal{M}_T = \bar{u}_{r_1}(k_1)(-\imath e\gamma_\mu)u_{s_1}(p_1)\frac{-\imath g^{\mu\nu}}{q^2}v_{s_2}(p_2)(\imath e\gamma_\nu)\bar{v}_{r_2}(k_2) \tag{4.5}$$

The $u(p_k)$, $\bar{u}(p_k)$ are the fermions spinors, $v(p_k)$, $\bar{v}(p_k)$ are antifermions spinors, q is the four-momentum of the mediator photon and it is equal to $q^2 = (p_1 - k_1)^2$. I rewrite the equation 4.5, introducing the *lepton currents* L_μ. There are an electron

current E_μ and a positron current P^μ.

$$\imath\mathcal{M}_T = \frac{\imath e^2}{t} E_\mu P^\mu \tag{4.6}$$

The first is $E_\mu = \bar{u}_{r_1}(k_1)\gamma_\mu u_{s_1}(p_1)$, while the second is $P^\mu = \bar{v}_{s_2}(p_2)\gamma^\mu v_{r_2}(k_2)$. The ν index vanishes because it is contracted with the metric tensor and I rewrite the q^2 at the denominator as $t = q^2 = (p_1 - k_1)^2$.

Actually, the T-channel has an infrared divergence due to the virtual photon, which can also transmit negative q^2 but cannot be at rest. This manifests itself physically in the impossibility of producing a particle that is at rest and one that has $E = E_i$. To eliminate this divergence, I make an *hard cut-off*, fixing a minimum energy value during the momentum-integration. This is one of the possible choices of regularisation of physical processes, but it is reasonable since CalcHEP makes the same *hard cut-off*, selecting only final particles with energy greater than this value. This problem is not present in the S-channel since the produced photon is real.

The squared transition matrix element of the process is $|\mathcal{M}|^2 = \mathcal{M}\mathcal{M}^*$:

$$|\mathcal{M}_T|^2 = \frac{e^4}{t^2}(E_\mu P_\nu)(E^\mu P^\nu)^* = \frac{e^4}{t^2} E_{\mu\nu} P^{\mu\nu} \tag{4.7}$$

where

$$\begin{aligned}
E^{\mu*} &= (\bar{u}_{r1}(k_1)\gamma^\mu u_{s1}(p_1))^* \\
&= [(u_{r1}(k_1)^\dagger \underbrace{\gamma^0\gamma^\mu\gamma^0}_{\gamma^{\mu\dagger}} \gamma^0 u_{s1}(p_1))^\dagger]^T \\
&= \bar{u}_{s1}(p_1)\gamma^\mu u_{r1}(k_1)
\end{aligned} \tag{4.8}$$

and $P^{\nu*} = \bar{v}_{s_2}(p_2)\gamma^\nu v_{r_2}(k_2)$ (To have a better understanding of these identies, see Appendix B).

Considering unpolarized states, I average the initial states and sum over final states, thus the square of the transition matrix element becomes:

$$|\mathcal{M}_T|^2 \rightarrow \frac{1}{4} \sum_{s_1,s_2,r_1,r_2} |\mathcal{M}_T|^2, \tag{4.9}$$

and I introduce the completeness relations for fermions and anti-fermions, related to the Dirac's equation:

$$\sum_s u_s(p)\bar{u}_s(p) = \not{p} + m \tag{4.10}$$

$$\sum_s v_s(p)\bar{v}_s(p) = \not{p} - m \tag{4.11}$$

where $\not{V} = \gamma^\alpha V_\alpha$. Then, using the Feynman trace technology (see Appendix B), I write the transition matrix element as a function of momenta and masses. By multiplying for the complex conjugate of the transition matrix element, I evaluate the trace because the polarization indices are contracted, then

$$\frac{1}{4}\sum_{s_1,s_2,r_1,r_2}|\mathcal{M}_T|^2 \to \frac{e^4}{4t^2}\text{Tr}[(\not{k}_1+m_e)\gamma^\mu(\not{p}_1+m_e)\gamma^\nu]\text{Tr}[(\not{p}_2-m_e)\gamma_\mu(\not{k}_2-m_e)\gamma_\nu]. \tag{4.12}$$

Making explicit the slashed four-vectors, I obtain traces depending on γ-matrices only.

$$\frac{e^4}{4t^2}\left\{k_{1B}p_{1A}\text{Tr}[\gamma^B\gamma^\mu\gamma^A\gamma^\nu] + m_e^2\text{Tr}[\gamma^\mu\gamma^\nu]\right\} \\ \times\left\{p_2^C k_2^D\text{Tr}[\gamma_C\gamma_\mu\gamma_D\gamma_\nu] + m_e^2\text{Tr}[\gamma_\mu\gamma_\nu]\right\} \tag{4.13}$$

The traces with three gammas vanish (as shown in Appendix B). I obtain the square matrix element as a function of Lorentz invariant quantities only:

$$\frac{8e^4}{t^2}\left\{(p_1 \cdot p_2)(k_1 \cdot k_2) + (p_1 \cdot k_2)(k_1 \cdot p_2) + m_e^2 t\right\} = \frac{8e^4}{t^2}\mathcal{A}^2. \tag{4.14}$$

I put equation 4.14 into equation 4.3 and then I integrate it.

$$\sigma_T = \frac{8e^4}{4\sqrt{(p_1 \cdot p_2)^2 - m_e^4}}\int\frac{d\boldsymbol{k_1}}{(2\pi)^3}\frac{d\boldsymbol{k_2}}{(2\pi)^3}\frac{(2\pi)^4}{2E_1 2E_2}\delta^4(k_1 + k_2 - p_1 - p_2)\frac{\mathcal{A}^2}{t^2}. \tag{4.15}$$

Simplifying constants and writing $d\boldsymbol{k_2}$ in its Lorentz invariant 4-dimensional form:

$$\sigma_T = 2\pi K\int\frac{d\boldsymbol{k_1}}{(2\pi)^3 2E_1}d^4k_2\vartheta(E_2)\delta(k_2^2 - m_e^2)\delta^4(k_1 + k_2 - p_1 - p_2)\frac{\mathcal{A}^2}{t^2} \tag{4.16}$$

$\frac{4e^4}{s\sqrt{1-\frac{4m_e^2}{s}}} = K$. The ϑ and δ functions have the role of determining positive final energy and its conservation. Namely, they fix the final state to be on-shell. Now, I can integrate $\delta^4(k_1 + k_2 - p_1 - p_2)$ and $\vartheta(E_2) = 1$ because the final energy E_2 is

positive.

$$\sigma_T = 2\pi K \int \frac{d\mathbf{k_1}}{(2\pi)^3 2E_1} \delta[2k_1(p_1 + p_2) - s]\frac{\mathcal{A}^2}{t^2} \tag{4.17}$$

Where I substituted $s = 2m_e^2 + 2p_1 \cdot p_2$.

To conclude the calculation, I change the reference frame moving to the Centre of Mass frame (CoM frame), where this integral is easier to derive and the four four-momenta are:

$$\begin{aligned} p_1 = (E, \mathbf{p}) \ , \ p_2 = (E, -\mathbf{p}) \\ k_1 = (\tilde{E}, \mathbf{k}) \ , \ k_2 = (\tilde{E}, -\mathbf{k}). \end{aligned} \tag{4.18}$$

In the CoM frame, $s = 4E^2$ and $(p_1 + p_2) \cdot k_1 = 2E\tilde{E} = \sqrt{s}\tilde{E}$, then the cross section becomes:

$$\sigma_T = \frac{2\pi K}{2\sqrt{s}} \int \frac{d\Omega dk k^2}{(2\pi)^3 2\tilde{E}} \delta(\tilde{E} - \frac{\sqrt{s}}{2})\frac{\mathcal{A}^2}{t^2}. \tag{4.19}$$

Considering $\tilde{E}^2 = m_e^2 + \mathbf{k}^2 \Rightarrow \tilde{E}d\tilde{E} = kdk$, I can change the integration variable to integrate the energy and the Dirac's delta function. Afterwards, I take into account the full expression of $\frac{\mathcal{A}^2}{t^2}$.

$$\sigma_T = \frac{e^4}{8\pi^2 s} \int d\varphi \, d\cos\vartheta \, \frac{\mathcal{A}^2(t, s, m_e^2, \vartheta)}{t^2} \tag{4.20}$$

Where ϑ is the scattering angle in Centre of Mass frame and φ is the azimuthal angle. To evaluate the last integral, I have to change the integration variable, moving from $\cos\vartheta$ to t-Mandelstam variable

$$t = 2m_e - 2p_1 \cdot k_1 = 2(\frac{s}{4} - m_e^2)(\cos\vartheta - 1) \tag{4.21}$$

so $dt = 2(\frac{s}{4} - m_e^2)d\cos\vartheta$. I performed all of the substitution in $\mathcal{A}^2$, taking into account that I have fixed the final energy with the delta of Dirac, so the cross section becomes:

$$\sigma_T = \frac{4\pi\alpha^2}{s\left[2(\frac{s}{4} - m_e^2)\right]} \int dt \Big[\underbrace{\frac{1}{4}}_{\text{I}} + \underbrace{\frac{1}{t}(\frac{s}{2})}_{\text{II}} + \underbrace{\frac{1}{t^2}(\frac{s^2}{2} + 2m_e^4 - 2sm_e^2)}_{\text{III}} \Big], \tag{4.22}$$

where $\alpha = \frac{e^2}{4\pi}$ is the fine structure constant. I evaluate the three terms indipendently to show the previously mentioned IR divergence in II and III. To solve this problem, I make an *hard cut-off* imposing, in the laboratory frame, the scattering angle to be greater than the one associated with the production of a particle with a certain minimum value of energy, to exclude the production of a particle

at rest. To derive ϑ_R, I evaluate the scattering angle as a function of the initial four-momenta and masses in laboratory frame. Considering the s-Mandelstam variable, I have

$$p_1 \cdot p_2 = k_1 \cdot k_2 \tag{4.23}$$

and, since $k_2 = p_1 + p_2 - k_1$, it becomes

$$p_1 \cdot p_2 = k_1 \cdot (p_1 + p_2 - k_1). \tag{4.24}$$

The four-momenta, in this reference frame, are:

$$
\begin{aligned}
p_1 &= (m_e, 0, 0, 0) \ , \ p_2 = (E_2, 0, 0, p_{2_z}) \\
k_1 &= (E_1', k_{1_x}', k_{1_y}', k_{1_z}') \ , \ p_2 = (E_2', k_{2_x}', k_{2_y}', k_{2_z}')
\end{aligned}
\tag{4.25}
$$

where the primated four-vector are related to the final particles. I derive $\cos \vartheta_R$ as a function of the initial energy, the masses and the final energy E', whose value is fixed by the *hard cut-off*. CalcHEP energy cut is $E' = 1$ MeV, I impose the same. I will show how the CalcHEP cut-off works in the section 4.3.

$$\vartheta_R^{LabF} = \arccos \left(\frac{E'E + m_e E' - m_e E - m_e^2}{\sqrt{E_1'^2 - m_e^2}\sqrt{E^2 - m_e^2}} \right) = 0.964 \text{ rad} \tag{4.26}$$

Moving to the Centre of Mass frame, where the variables of the cross section in equation 4.22 are defined

$$\sin \vartheta_R^{CM} = \frac{|\boldsymbol{k}_1^{LabF}|}{|\boldsymbol{k}_1^{CM}|} \sin \vartheta_{R^{LabF}} \rightarrow \vartheta_R^{CM} = 0.833 \text{ rad}, \tag{4.27}$$

then I integrate each terms of the eq. 4.22. The first integral is not divergent and I integrate it from -1 to 1 as follow:

$$\text{I} = \frac{1}{4} \int dt = \frac{1}{2} [2(\frac{s}{4} - m_e^2)], \tag{4.28}$$

the second is

$$\text{II} = \int \frac{dt}{t} \left(\frac{s}{2}\right) = \left(\frac{s}{2}\right) \int \frac{dx}{x - 1} = \left(\frac{s}{2}\right) \ln \frac{1 - \cos \vartheta_R}{2} \tag{4.29}$$

and the third

$$
\text{III} = \left(\frac{s^2}{2} + 2m_e^4 - 2sm_e^2\right) \int \frac{dt}{t^2} = \frac{\frac{s^2}{2} + 2m_e^4 - 2sm_e^2}{2(\frac{s}{4} - m_e^2)} \int \frac{dx}{(x-1)^2} =
$$
$$
= \frac{\frac{s^2}{2} + 2m_e^4 - 2sm_e^2}{2(\frac{s}{4} - m_e^2)} \left[\frac{1}{1 - \cos\vartheta_R} - \frac{1}{2}\right]. \tag{4.30}
$$

The final expression of the cross section is:

$$
\sigma_T = \frac{4\pi\alpha^2}{s}\left[\frac{1}{2} + \frac{1}{1 - \frac{4m_e^2}{s}}\ln\frac{1 - \cos\vartheta_R}{2} + \frac{\frac{s^2}{2} + 2m_e^4 - 2sm_e^2}{(\frac{s}{2} - 2m_e^2)^2}\left(\frac{1}{1 - \cos\vartheta_R} - \frac{1}{2}\right)\right] \tag{4.31}
$$

which depends on the $\cos\vartheta_R$ regularising term, that is evaluated in equation 4.27 and multiplying the cross section for $(\hbar c)^2$, I get the physical value:

$$
\sigma_T = 5.26 \cdot 10^{10} \text{ pb} \tag{4.32}
$$

4.1.2 The Annihilation process

The annihilation process called *S-channel*, is mediated by a real photon and it is represented in Fig. 4.3 where p_i are the initial four-momenta with s_i spin polarizations and k_i are the final four-momenta with r_i spin polarizations.
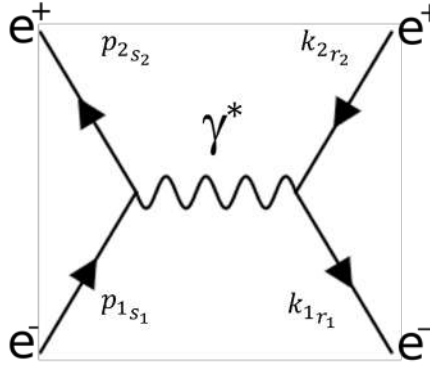

Figure 4.3: Feynman diagram of Bhabha scattering's S-channel

The expression of the *s*-Mandelstam variable is:

$$
s = (p_1 + p_2)^2 = 2m_e^2 + 2p_1 \cdot p_2 = 2m_e^2 + 2k_1 \cdot k_2 = (k_1 + k_2)^2, \tag{4.33}
$$

which is equal to the invariant mass of the process. I derive the transition matrix element with similar algebra of the T-channel process, so $\mathcal{M}_S$ is:

$$\imath\mathcal{M}_S = \bar{v}_{s_2}(p_2)(\imath e\gamma_\mu)u_{s_1}(p_1)\frac{-\imath g^{\mu\nu}}{q^2}\bar{u}_{r_1}(k_1)(\imath e\gamma_\nu)v_{r_2}(k_2) \tag{4.34}$$

I introduce the *lepton currents* $E_\mu^{i,f}$, where i and f correspond to the initial and final state respectively, thus the equation 4.34 becomes:

$$\imath\mathcal{M}_S = \frac{\imath e^2}{q^2}E_\mu^i E^{f\mu}. \tag{4.35}$$

The electron currents are $E_\mu^i = \bar{v}_{s_2}(p_2)\gamma_\mu u_{s_1}(p_1)$ and $E^{f\mu} = \bar{u}_{r_1}(k_1)\gamma^\mu v_{r_2}(k_2)$, and the ν index vanishes because contracted with the metric tensor $g_{\mu\nu}$.

The squared transition matrix element is:

$$|\mathcal{M}_S|^2 = \frac{e^4}{s^2}(E_\mu^i E_\nu^f)(E^{i\mu}E^{f\nu})^* = \frac{e^4}{s^2}E_{\mu\nu}^i E^{f\mu\nu} \tag{4.36}$$

where $q^2 = (p_1+p_2)^2 = s$, $E_\mu^{i\,*} = \bar{u}_{s_1}(p_1)\gamma_\mu v_{s_2}(p_2)$ and $E^{f\mu\,*} = \bar{v}_{r_2}(k_2)\gamma^\mu u_{r_1}(k_1)$ (to demonstrate these identities, refer to Appendix B).

For unpolarized states, I evaluate the transition matrix element averaging the initial spin polarization states and summing over the final ones. Then, $|\mathcal{M}_S|^2$ becomes:

$$|\mathcal{M}_S|^2 \to \frac{1}{4}\sum_{s_1,s_2,r_1,r_2}|\mathcal{M}_S|^2 \tag{4.37}$$

using relations 4.10 and 4.11, and the Feynman trace technology, I write down the transition matrix element as a function of momenta and masses.

$$\frac{1}{4}\sum_{s_1,s_2,r_1,r_2}|\mathcal{M}_S|^2 \to \frac{e^4}{4s^2}\text{Tr}[(\slashed{p}_2-m_e)\gamma^\mu(\slashed{p}_1+m_e)\gamma^\nu]\text{Tr}[(\slashed{k}_1+m_e)\gamma_\mu(\slashed{k}_2-m_e)\gamma_\nu] \tag{4.38}$$

Doing similar calculations of T-channel, I obtain traces depending on γ matrices only:

$$\frac{e^4}{4s^2}\left\{p_{2B}p_{1A}\text{Tr}[\gamma^B\gamma^\mu\gamma^A\gamma^\nu] - m_e^2\text{Tr}[\gamma^\mu\gamma^\nu]\right\}$$
$$\times\left\{k_1^C k_2^D\text{Tr}[\gamma_C\gamma_\mu\gamma_D\gamma_\nu] - m_e^2\text{Tr}[\gamma_\mu\gamma_\nu]\right\}, \tag{4.39}$$

and substituting s with the equation 4.33, I obtain the square transition matrix element as a function of Lorentz invariant quantities

$$\frac{8e^4}{s}\left[\frac{(p_1 \cdot k_1)(p_2 \cdot k_2)}{s} + \frac{(p_1 \cdot k_2)(p_2 \cdot k_1)}{s} + m_e^2\right] = \frac{8e^4}{s}\mathcal{B}^2. \tag{4.40}$$

Putting this last expression into equation 4.3, I get the total cross section.

$$\sigma_S = \frac{4e^4}{s^2\sqrt{1 - \frac{4m_e^2}{s}}}\int \frac{d\boldsymbol{k_1}}{(2\pi)^3}\frac{d\boldsymbol{k_2}}{(2\pi)^3}\frac{(2\pi)^4}{2E_1 2E_2}\delta^4(k_1 + k_2 - p_1 - p_2)\mathcal{B}^2 \tag{4.41}$$

I call $K = \frac{4e^4}{s^2\sqrt{1-\frac{4m_e^2}{s}}}$, and in the same way I did in the equation 4.16, I write the integration volume in Lorentz invariant form to integrate the $\delta^4(k_1 + k_2 - p_1 - p_2)$ term:

$$\sigma_S = 2\pi K \int \frac{d\boldsymbol{k_1}}{(2\pi)^3 2E_1}d^4k_2\vartheta(E_2)\delta(k_2^2 - m_e^2)\delta^4(k_1 + k_2 - p_1 - p_2)\mathcal{B}^2. \tag{4.42}$$

Since $E_2 > 0$, the ϑ-function is equal to 1 and the cross section becomes:

$$\sigma_S = 2\pi K \int \frac{d\boldsymbol{k_1}}{(2\pi)^3 2E_1}\delta[(p_1 + p_2 - k_1)^2 - m_e^2)]\mathcal{B}^2. \tag{4.43}$$

I change the reference frame moving to the Centre of Mass one (CoM frame), where the four four-momenta are:

$$p_1 = (E, \boldsymbol{p}) , \; p_2 = (E, -\boldsymbol{p})$$
$$k_1 = (\tilde{E}, \boldsymbol{k}) , \; k_2 = (\tilde{E}, -\boldsymbol{k}) \tag{4.44}$$

In the CoM frame, $s = 4E^2$ and $(p_1 + p_2) \cdot k_1 = 2E\tilde{E} = \sqrt{s}\tilde{E}$, so the cross section becomes:

$$\sigma_S = \frac{2\pi K}{2\sqrt{s}}\int \frac{d\Omega dk k^2}{(2\pi)^3 2\tilde{E}}\delta(\tilde{E} - \frac{\sqrt{s}}{2})\mathcal{B}^2. \tag{4.45}$$

Considering $\tilde{E}^2 = m_e^2 + k_1^2 \Rightarrow 2\tilde{E}d\tilde{E} = 2k_1dk_1$ I can integrate the energy from 0 to ∞ obtaining an integral over solid angle only:

$$\sigma_S = \frac{e^4}{8\pi^2 s^2}\int d\Omega \; \mathcal{B}^2 = \frac{2\alpha^2}{s^2}\int d\Omega \; \mathcal{B}^2. \tag{4.46}$$

$\mathcal{B}^2$ depends on the ϑ scattering angle between final particles, so I evaluate it considering the following identity in the CoM frame:

$$p_1 \cdot k_1 = (E, \boldsymbol{p}) \cdot (\tilde{E}, \boldsymbol{k}) = E\tilde{E} - cos\vartheta|\boldsymbol{p}||\boldsymbol{k}|$$

where $E\tilde{E} = \frac{s}{4}$, $|\boldsymbol{p}| = \sqrt{E^2 - m_e^2}$ and $|\boldsymbol{k}| = \sqrt{\tilde{E}^2 - m_e^2}$ and since the four-momentum is conserved

$$(p_1 - k_1)^2 = (p_2 - k_2)^2 \Rightarrow 2m_e^2 - 2p_1 \cdot k_1 = 2m_e^2 - 2p_2 \cdot k_2. \tag{4.47}$$

The last equation is true even if I switch $k_1 \leftrightarrow k_2$, then I obtain the $\mathcal{B}^2$ term as a function of constants and the scattering angle ϑ.

$$\mathcal{B}^2 = \frac{s}{8}\left[1 - \cos^2\vartheta(1 - \frac{4m_e^2}{s})^2\right] + m_e^2 \tag{4.48}$$

where the $\cos\vartheta$ term vanish because it is an odd function integrated in a even range. I substitute this term into the cross section formula

$$\sigma_S = \frac{2\alpha^2}{s^2}2\pi\int_{-1}^{1} d(\cos\vartheta)\,\frac{s}{8}\left[1 - \cos^2\vartheta(1 - \frac{4m_e^2}{s})^2\right] + m_e^2 \tag{4.49}$$

and I integrate the last equation to get the total cross section:

$$\sigma_S = \frac{4\pi\alpha^2}{3s^2}(s + 4m_e^2 + 4\frac{m_e^4}{s}) = 3.0207 \times 10^8\text{pb} \tag{4.50}$$

where I multiplied for $(\hbar c)^2$ to get a physical value.

4.2 $e^+e^- \to \gamma\gamma$ process

The $e^+e^- \to \gamma\gamma$ reaction is a process that occurs at the leading-order and it is mediated by a virtual fermion. It is characterised by two identical photons as final state particles. The $\gamma\gamma$-production involves two different Feynman diagrams as shown in Fig. 4.4, where p_i are the initial four-momenta with spin polarization s_i, the polarization vectors of the photons are $\varepsilon^{\mu*}(k_i)$ whose complex conjugate is due to the photons being outgoing.

I write the transition matrix element referring to the Appendix A. In this case $|\mathcal{M}_{\gamma\gamma}|$ involves two terms, one for each diagram.

$$\imath\mathcal{M}_{\gamma\gamma} = \bar{v}_{s_2}(p_2)(\imath e\gamma_\mu)\varepsilon_2^\mu(k_2)^*\frac{\imath(\not{p}_1 - \not{k}_1) + m_e}{(p_1 - k_1)^2 - m_e^2}(\imath e\gamma_\nu)u_{s_1}(p_1)\varepsilon_1^\nu(k_1)^*$$
$$+ \bar{v}_{s_2}(p_2)(\imath e\gamma_\nu)\varepsilon_1^\nu(k_1)^*\frac{\imath(\not{p}_1 - \not{k}_2) + m_e}{(p_1 - k_2)^2 - m_e^2}(\imath e\gamma_\mu)u_{s_1}(p_1)\varepsilon_2^\mu(k_2)^* \tag{4.51}$$

where $\varepsilon_{\mu,\nu}^*$ are the polarization vectors of the outgoing photons. Before going
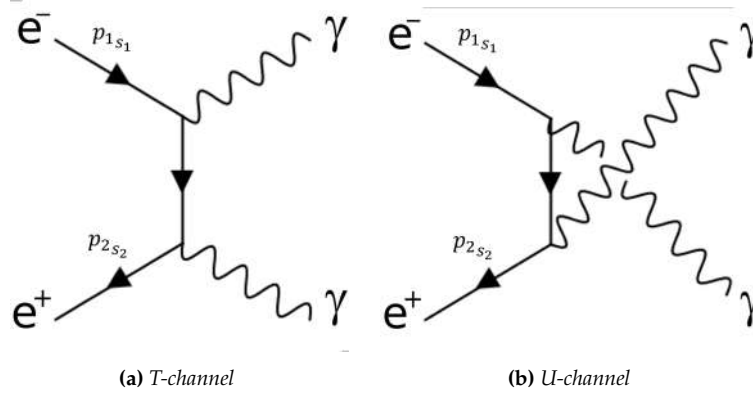
(a) *T-channel* **(b)** *U-channel*

Figure 4.4: Feynman diagrams of $\gamma\gamma$-production.

through similar calculations as for the Bhabha scattering, I make some algebra, based on the Dirac's equation [52]. I rewrite the 4.51 as follow:

$$\imath \mathcal{M}_{\gamma\gamma} = \imath e^2 \varepsilon_1^\nu(k_1)^* \varepsilon_2^\mu(k_2)^* \bar{v}_{s_2}(p_2) \left[\frac{\gamma_\mu(\not{p}_1 - \not{k}_1 + m_e)\gamma_\nu}{(p_1 - k_1)^2 - m_e^2} + \frac{\gamma_\nu(\not{p}_1 - \not{k}_2 + m_e)\gamma_\mu}{(p_1 - k_2)^2 - m_e^2} \right] u_{s_1}(p_1)$$

(4.52)

and I can make a few semplifications before squaring this expression. Since $p_1^2 = m_e^2$ and $k_1^2 = k_2^2 = 0$, the denominator of the lepton propagators are

$$\begin{aligned}
(p_1 - k_1)^2 - m_e^2 &= -2p_1 \cdot k_1 \\
(p_1 - k_2)^2 - m_e^2 &= -2p_1 \cdot k_2
\end{aligned}$$

(4.53)

while, to simplify the numerator, I consider the anticommutation rule of the gamma matrices (B.1) and the Dirac equation:

$$(\not{p} - m_e)u(p) = 0.$$

(4.54)

With these algebraic steps I obtain the following expression of the transition matrix element:

$$\imath \mathcal{M}_{\gamma\gamma} = \imath e^2 \varepsilon_1^\nu(k_1)^* \varepsilon_2^\mu(k_2)^* \bar{v}_{s_2}(p_2) \left[\frac{\gamma_\mu \not{k}_1 \gamma_\nu - 2\gamma_\mu p_{1\nu}}{2p_1 \cdot k_1} + \frac{\gamma_\nu \not{k}_2 \gamma_\mu - 2\gamma_\nu p_{1\mu}}{2p_1 \cdot k_2} \right] u_{s_1}(p_1).$$

(4.55)

I have to introduce rules for the sum of the photon polarization vectors. They play for the photon polarization vectors the same rule of the completeness relations of the Dirac spinors in equation 4.10 and 4.11. The sum over photon polarization vectors is defined as:

$$\sum_{polarizations} \varepsilon_\mu^* \varepsilon_\nu = -g_{\mu\nu},$$

(4.56)

(for the full derivation of this identity, refer to "*An Introduction to quantum field theory*" of M.J. Peskin and D.V. Schroeder [52, p. 159-161]).

I can finally write the squared transition matrix element

$$
\begin{aligned}
|\mathcal{M}_{\gamma\gamma}|^2 = {} & e^4 \varepsilon_1^\nu(k_1)^* \varepsilon_1^\alpha(k_1) \varepsilon_2^\mu(k_2)^* \varepsilon_2^\beta(k_2) \times \\
& \times \left\{ \bar{v}_{s_2}(p_2) \left[\frac{\gamma_\mu \slashed{k}_1 \gamma_\nu - 2\gamma_\mu p_{1\nu}}{2p_1 \cdot k_1} + \frac{\gamma_\nu \slashed{k}_2 \gamma_\mu - 2\gamma_\nu p_{1\mu}}{2p_1 \cdot k_2} \right] u_{s_1}(p_1) \right\} \times \\
& \times \left\{ \bar{u}_{s_1}(p_1) \left[\frac{\gamma_\alpha \slashed{k}_1 \gamma_\beta - 2\gamma_\beta p_{1\alpha}}{2p_1 \cdot k_1} + \frac{\gamma_\beta \slashed{k}_2 \gamma_\alpha - 2\gamma_\alpha p_{1\beta}}{2p_1 \cdot k_2} \right] v_{s_2}(p_2) \right\}.
\end{aligned}
\tag{4.57}
$$

I sum over photon polarization states and I apply the completeness relation of the Dirac's spinors, in a similar way I did for the Bhabha scattering, to obtain the following expression of the equation 4.57:

$$
\begin{aligned}
\frac{1}{4} \sum_{spins} |\mathcal{M}_{\gamma\gamma}|^2 = {} & \frac{e^4}{4} g^{\nu\alpha} g^{\mu\beta} \mathrm{Tr}\left\{ (\slashed{p}_2 - m_e) \left[\frac{\gamma_\mu \slashed{k}_1 \gamma_\nu - 2\gamma_\mu p_{1\nu}}{2p_1 \cdot k_1} + \frac{\gamma_\nu \slashed{k}_2 \gamma_\mu - 2\gamma_\nu p_{1\mu}}{2p_1 \cdot k_2} \right] \times \right. \\
& \left. \times (\slashed{p}_1 + m_e) \left[\frac{\gamma_\alpha \slashed{k}_1 \gamma_\beta - 2\gamma_\beta p_{1\alpha}}{2p_1 \cdot k_1} + \frac{\gamma_\beta \slashed{k}_2 \gamma_\alpha - 2\gamma_\alpha p_{1\beta}}{2p_1 \cdot k_2} \right] \right\} \\
\equiv {} & \frac{e^4}{4} \left[\frac{A}{(2p_1 \cdot k_1)^2} + \frac{B}{(2p_1 \cdot k_1)(2p_1 \cdot k_2)} + \frac{C}{(2p_1 \cdot k_2)(2p_1 \cdot k_1)} + \frac{D}{(2p_1 \cdot k_2)^2} \right]
\end{aligned}
\tag{4.58}
$$

where A, B, C e D are complicated traces with many gamma matrices. Considering the relations in the Appendix B I can notice: A and D have the same expression if $k_1 \rightarrow k_2$ and also, since I can reverse the order of the gamma matrices inside a trace, B = C. Therefore I will compute only A and B.

I calculate the first trace:

$$
A = \mathrm{Tr}[(\slashed{p}_2 - m_e)(\gamma_\mu \slashed{k}_1 \gamma_\nu - 2\gamma_\mu p_{1\nu})(\slashed{p}_1 + m_e)(\gamma^\nu \slashed{k}_1 \gamma^\mu - 2\gamma^\mu p_1^\nu)]
\tag{4.59}
$$

where there are 16 traces, but half have odd number of gamma matrices, then vanish. I have to calculate traces like this one:

$$
\begin{aligned}
p_2^A p_1^C k_1^B k_1^D \mathrm{Tr}[\gamma_A \gamma_\mu \gamma_B \gamma_\nu \gamma_C \gamma^\nu \gamma_D \gamma^\mu] &= 4 p_2^A p_1^C k_1^B k_1^D \mathrm{Tr}[\gamma_A \gamma_B \gamma_C \gamma_D] \\
&= 16 p_2^A p_1^C k_1^B k_1^D (g_{AB} g_{CD} + g_{AD} g_{BC} - g_{AC} g_{BD}) \\
&= 32(p_1 \cdot k_1)(p_2 \cdot k_1)
\end{aligned}
\tag{4.60}
$$

where I considered the properties of the γ matrices in Appendix B. Without show each step of the calculation, I get the result of the first trace:

$$A = 16\left\{-4m_e^4 + 4m_e^2(p_1 \cdot k_1) - 2m_e^2(p_1 \cdot p_2) + 2m_e^2(p_2 \cdot k_1) + 2(p_1 \cdot k_1)(p_2 \cdot k_1)\right\} \quad (4.61)$$

therefore the fourth trace is:

$$D = 16\left\{-4m_e^4 + 4m_e^2(p_1 \cdot k_2) - 2m_e^2(p_1 \cdot p_2) + 2m_e^2(p_2 \cdot k_2) + 2(p_1 \cdot k_2)(p_2 \cdot k_2)\right\}. \quad (4.62)$$

Now I reintroduce the Mandelstam variables associated to this process, including the u variable, which is related to the process in Fig. 4.4b

$$\begin{aligned}
s &= (p_1 + p_2)^2 = 2m_e^2 + 2p_1 \cdot p_2 \\
t &= (p_1 - k_1)^2 = m_e^2 - 2p_1 \cdot k_1 \\
u &= (p_1 - k_2)^2 = m_e^2 - 2p_1 \cdot k_2
\end{aligned} \quad (4.63)$$

and I sobstitute s, t and u in the squared matrix element to semplify the expression before integration, so the A trace becomes:

$$A = 16[-m_e^4 + -\frac{3}{2}m_e^2 t - \frac{1}{2}m_e^2 u + \frac{1}{2}ut] \quad (4.64)$$

and exchanging $k_1 \to k_2$, I derive the expression of the trace D:

$$D = 16[-m_e^4 + -\frac{3}{2}m_e^2 u - \frac{1}{2}m_e^2 t + \frac{1}{2}ut]. \quad (4.65)$$

I make similar calculation for B and C deriving the following expressions:

$$B = C = 8m_e^2(s - 4m_e^2). \quad (4.66)$$

Putting all into the 4.58, rewriting s, t and u as a function of the four-momenta, I finally obtain the transition matrix element of the process:

$$\frac{1}{4}\sum_{spins}|\mathcal{M}_{\gamma\gamma}|^2 = 2e^4\left[\frac{p_1 \cdot k_2}{p_1 \cdot k_1} + \frac{p_1 \cdot k_1}{p_1 \cdot k_2} + 2m_e^2\left(\frac{1}{p_1 \cdot k_1} + \frac{1}{p_1 \cdot k_2}\right) - m_e^4\left(\frac{1}{p_1 \cdot k_1} + \frac{1}{p_1 \cdot k_2}\right)^2\right] \quad (4.67)$$

I recall the terms into the squared braked as $\mathcal{C}^2$ and I substitute the 4.67 in the equation 4.3 writing down the cross section:

$$\sigma_{\gamma\gamma} = \frac{e^4}{s\sqrt{1 - \frac{4m_e^2}{s}}}\int \frac{d\mathbf{k}_1}{(2\pi)^3}\frac{d\mathbf{k}_2}{(2\pi)^3}\frac{(2\pi)^4}{2E_1 2E_2}\delta^4(k_1 + k_2 - p_1 - p_2)\mathcal{C}^2, \quad (4.68)$$

and I integrate the $d\boldsymbol{k}_2$ as I did above

$$\sigma_{\gamma\gamma} = K \int \frac{d\boldsymbol{k}_1}{(2\pi)^3 2E_1} \delta[(p_1 + p_2 - k_1)^2] \mathcal{C}^2 \tag{4.69}$$

where $K = \frac{2\pi e^4}{s\sqrt{1 - \frac{4m_e^2}{s}}}$. Now I specialise to the centre of Mass frame, where the four-momenta are:

$$\begin{aligned} p_1 &= (E, \boldsymbol{p}) \,, \; p_2 = (E, -\boldsymbol{p}) \\ k_1 &= (E, E\cos\vartheta, 0, E\sin\vartheta) \,, \; k_2 = (E, E\sin\vartheta, 0, -E\cos\vartheta) \end{aligned} \tag{4.70}$$

The second components of the photons four-momenta are 0 because the process occurs in a plane, then the process is manifestly invariant with respect to the azimuthal angle φ. In this frame $4E^2 = s$ the equation 4.69 becomes:

$$\sigma_{\gamma\gamma} = \frac{K}{2\sqrt{s}} \int \frac{d\Omega E^2 dE}{(2\pi)^3 2E} \delta(E - \frac{\sqrt{s}}{2}) \mathcal{C}^2 = \frac{\pi\alpha^2}{s\sqrt{1 - \frac{4m_e^2}{s}}} \int d(\cos\vartheta)\, \mathcal{C}^2(s, \vartheta) \tag{4.71}$$

the $\mathcal{C}^2$ term depends only on the s-Mandelstam variable and the ϑ angle, due to the selection of the reference frame and to the massless nature of the final photons, so I now make explicit the $\mathcal{C}^2$:

$$\sigma_{\gamma\gamma} = \frac{2\pi\alpha^2}{s\sqrt{1 - \frac{4m_e^2}{s}}} \int d\cos\vartheta \left[\underbrace{\frac{\frac{s}{4} + p^2\cos^2\vartheta}{m_e^2 + p^2\sin^2\vartheta} + \frac{2m_e^2}{m_e^2 + p^2\sin^2\vartheta}}_{\text{I+II}} - \underbrace{\frac{2m_e^4}{(m_e^2 + p^2\sin^2\vartheta)^2}}_{\text{III}} \right] \tag{4.72}$$

where $p = \frac{s}{4} - m_e^2$. Now I want to underline that since the two final photons are indistinguishable, I count all final states by integrating only over $0 \leq \vartheta \leq \frac{\pi}{2}$. I evaluate the first two integrals together because they have the same denominator

$$\text{I + II} = -1 + \frac{1 + \frac{4m_e^2}{s}}{\sqrt{1 - \frac{4m_e^2}{s}}} \ln \frac{1 + \sqrt{1 - \frac{4m_e^2}{s}}}{1 - \sqrt{1 - \frac{4m_e^2}{s}}}, \tag{4.73}$$

while the third term is:

$$\text{III} = -\frac{8m_e^4}{s^2\sqrt{1 - \frac{4m_e^2}{s}}} \left[\frac{s\sqrt{1 - \frac{4m_e^2}{s}}}{2m_e^2} + \ln \frac{1 + \sqrt{1 - \frac{4m_e^2}{s}}}{1 - \sqrt{1 - \frac{4m_e^2}{s}}} \right] \tag{4.74}$$

and finally I obtain the cross section as a function of s and the electron mass m_e, that is, in physical units:

$$\sigma_{\gamma\gamma} = \frac{2\pi\alpha^2}{s\sqrt{1 - \frac{4m_e^2}{s}}} \times \{\text{I} + \text{II} + \text{III}\} = 2.7477 \cdot 10^9 \text{pb} \tag{4.75}$$

4.3 CalcHEP cross section and events generator

CalHEP is a package for Feynman diagrams calculations and integration over multi-particle phase space [53]. It derives cross sections and produces simulated events for particle physics processes. I used CalcHEP to compute the cross sections values for the different processes of interest and to produce the kinematic of the final states for events which I analyse in the following sections. CalcHEP was designed as a software for high energy physics simulations at the scale of hundreds of GeV. To get reliable results at the energy scale of the PADME experiment I modified the Standard Model parameters, introducing a non zero electron mass and modifying the electromagnetic fine structure constant value α_{EM}. I moved the α_{EM} value, from the one used to reproduce high energy processes $\alpha_{EM} \simeq \frac{1}{128}$ to the proper low energies (LE) value:

$$\alpha_{EM}^{LE} \simeq \frac{1}{137} \tag{4.76}$$

which corresponds to the value of the coupling that I used during the analytic calculations. I underline the coupling α_{EM} is actually a running coupling, so it depends strictly on the energy of the processes, but I neglect its variation considering it as a constant in the studied energy range.

I also modified the value of electron mass, which was set to zero being negligible in high energy processes, to

$$m_e = 0.511 \, \text{MeV}. \tag{4.77}$$

A non zero value of the electron mass is required in fixed target experiment simulation, being one of the particle at rest, in fact it's energy its equal to its mass. To have a better understanding of CalcHEP's characteristics and behaviour, but also to understand how the parameters were modified, one can refer to [53].

After setting the correct experimental physical parameters, I set the initial state

characteristics by setting the electron momentum at zero and the positron momentum at 282 MeV directed along the Z axis.

$$P_{e_i^-} = (m_e, 0, 0, 0)$$
$$P_{e_i^+} = (E_i, 0, 0, p_{z_i})$$
(4.78)

where $p_{z_i} = 282$ MeV. All the diagrams mediated by the Z boson have been removed from the model to have only processes mediated by photon. At so low energies the z mediated contribution to the cross section is negligible. Fixing the processes to be a Bhabha scattering or $\gamma\gamma$-production I obtained Feynman diagrams like those in Fig. 4.2, 4.3, 4.4 and their square Feynman diagrams. Selecting only S-channel, T-channel and $\gamma\gamma$ square diagrams, without the interference ones, I produce sets of simulated events setting the number of events from which CalcHEP derives the cross sections. CalcHEP results are affected by a systematic error up to $\sim 5\%$, since CalcHEP is able to compute only tree level processes neglecting all of the next to leading order diagrams.

This is not a serious issue for this analysis because I'm using the cross section values just to derive an estimate of the exclusion limits. For the final experimental result more precise calculations will performed.

The simulated events are stored into a file `.txt` like the one in Fig 4.5, where the relevant information about the process are collected.

Referring to the section 4.1.1, I had to impose the *hard cut-off* to cure the T-channel infrared divergence: I required the minimal energy of the electron and positron to be greater than zero, namely

$$E_{min} > 1 \text{ MeV}.$$
(4.79)

This cut selects only particles with energy greater than zero, so it neglects processes which involve final states with $E \simeq E_i$.

In the equations below, I report the cross sections values derived by CalcHEP at the X17 resonance with the associated statistic errors:

$$\sigma_T = (5.155 \pm 0.04) \times 10^{11} \text{ pb}$$
(4.80)

$$\sigma_S = (3.022) \times 10^8 \text{ pb}$$
(4.81)

$$\sigma_{\gamma\gamma} = (2.734) \times 10^9 \text{ pb}$$
(4.82)

The errors associated to the Bhabha S-channel and γ-production are 5 orders of magnitude smaller than the values, so they will be neglected.

In Fig. 4.5, as an example, I shows few lines from one of `.txt` the events files produced by CalcHEP. In the fist lines "Headers" the following information are collected:

1. CalcHEP software version;

2. Type of process: two bodies in two bodies;

3. Properties of initial state: momentum (p_3) of both initial particles and `StrFun1` and `2` is "OFF" because electron and positron do not have structure functions;

4. The `PROCESS` line tells us which are the particles of the process. In this case "11" and "-11" are electron and positron codes; the γ's code is "22" [5];

5. The masses of each particle in [GeV];

6. The cross section of the process. In this case is an annihilation Bhabha scattering, so σ is equal to equation 4.81;

7. The total number of events;

8. The rest of the table is the real output of the CalcHEP simulation. It gives the particles momenta and other details of the process.

Each row is a different event while the columns represents one kinematical quantity of the described event final state.

```
#CalcHEP  3.8.9
#Type 2 -> 2
#Initial state
      P1_3=2.820000E-01   P2_3=-0.000000E+00
StrFun1="OFF"
StrFun2="OFF"
#PROCESS   -11(E) 11(e) -> 11(e) -11(E)
#MASSES  5.110000000E-04  5.110000000E-04  5.110000000E-04  5.110000000E-04
#Cross_section(Width)  3.022191E+08
#Number_of_events   1000000
#Sum_of_weights   1.0000E+06   1.0000E+06
#Events
```

P1_3 [Gev]	P2_3 [Gev]	P3_1 [Gev]	P3_2 [Gev]	P3_3 [Gev]	P4_1 [Gev]	P4_2 [Gev]	P4_3 [Gev]	Q_factor	alpha_QCD	Color chains
2.820000000E-01	1.3552527156E-20	2.7033735408E-03	-2.9586013235E-03	2.6526224530E-01	-2.7033735408E-03	2.9586013235E-03	1.6737775470E-02	1.000E+00	5.211E-01	
2.820000000E-01	1.3552527156E-20	8.4372496991E-03	-8.3988857639E-04	1.4378022837E-01	-8.4372496991E-03	8.3988857639E-04	1.3821977163E-01	1.000E+00	5.211E-01	
2.820000000E-01	1.3552527156E-20	9.6615016514E-04	5.7118206141E-03	2.4397799637E-01	-9.6615016514E-04	-5.7118206141E-03	3.8022003633E-02	1.000E+00	5.211E-01	
2.820000000E-01	1.3552527156E-20	6.7008172541E-03	-5.0972565591E-03	1.5793572125E-01	-6.7008172541E-03	5.0972565591E-03	1.2406427875E-01	1.000E+00	5.211E-01	
2.820000000E-01	1.3552527156E-20	4.0521255003E-03	-1.7555293177E-03	2.6137512816E-01	-4.0521255003E-03	1.7555293177E-03	2.0624871843E-02	1.000E+00	5.211E-01	
2.820000000E-01	1.3552527156E-20	-8.5266150872E-04	1.3153854584E-03	2.4296687817E-01	8.5266150872E-04	-1.3153854584E-03	2.7957033122E-01	1.000E+00	5.211E-01	
2.820000000E-01	1.3552527156E-20	-6.9304556371E-03	-2.8271142880E-03	7.4710155990E-02	6.9304556371E-03	2.8271142880E-03	2.0728984401E-01	1.000E+00	5.211E-01	
2.820000000E-01	1.3552527156E-20	-7.4017566068E-03	1.1805159965E-03	2.0696414017E-01	7.4017566068E-03	-1.1805159965E-03	7.5035859833E-02	1.000E+00	5.211E-01	
2.820000000E-01	1.3552527156E-20	-5.0880624991E-04	-2.5112151227E-03	2.7541061521E-01	5.0880624991E-04	2.5112151227E-03	6.5893847899E-03	1.000E+00	5.211E-01	
2.820000000E-01	1.3552527156E-20	3.6634432936E-03	1.1452700441E-03	2.6673188129E-01	-3.6634432936E-03	-1.1452700441E-03	1.5268118709E-02	1.000E+00	5.211E-01	
2.820000000E-01	1.3552527156E-20	-4.6498087664E-03	7.0549612014E-03	1.2892615389E-01	4.6498087664E-03	-7.0549612014E-03	1.5307384611E-01	1.000E+00	5.211E-01	
2.820000000E-01	1.3552527156E-20	5.2458192310E-03	-5.8886843104E-04	3.0645247391E-02	-5.2458192310E-03	5.8886843104E-04	2.5135475261E-01	1.000E+00	5.211E-01	
2.820000000E-01	1.3552527156E-20	5.1200424804E-03	-5.0831427839E-03	2.5308482573E-01	-5.1200424804E-03	5.0831427839E-03	2.8915174271E-02	1.000E+00	5.211E-01	
2.820000000E-01	1.3552527156E-20	8.3180005089E-04	4.4884759216E-03	2.2169588833E-02	-8.3180005089E-04	-4.4884759216E-03	2.5983041117E-01	1.000E+00	5.211E-01	
2.820000000E-01	1.3552527156E-20	7.6782214692E-03	-5.2079210003E-04	2.0023741331E-01	-7.6782214692E-03	5.2079210003E-04	8.1762586688E-02	1.000E+00	5.211E-01	
2.820000000E-01	1.3552527156E-20	3.0424449448E-03	5.7469968305E-03	2.3151138643E-01	-3.0424449448E-03	-5.7469968305E-03	5.0488613567E-02	1.000E+00	5.211E-01	
2.820000000E-01	1.3552527156E-20	-3.2493327536E-03	-7.1768445230E-03	8.8805174421E-02	3.2493327536E-03	7.1768445230E-03	1.9319482558E-01	1.000E+00	5.211E-01	
2.820000000E-01	1.3552527156E-20	2.0017099896E-03	6.0050894138E-03	4.7164938615E-02	-2.0017099896E-03	-6.0050894138E-03	2.3493506139E-01	1.000E+00	5.211E-01	
2.820000000E-01	1.3552527156E-20	5.9608610838E-03	4.9476468106E-03	1.9837716173E-01	-5.9608610838E-03	-4.9476468106E-03	8.3622838272E-02	1.000E+00	5.211E-01	
2.820000000E-01	1.3552527156E-20	-2.3005254891E-03	-5.1763439225E-03	2.4593428054E-01	2.3005254891E-03	5.1763439225E-03	3.6065719465E-02	1.000E+00	5.211E-01	
2.820000000E-01	1.3552527156E-20	7.7533905742E-03	2.2575831944E-03	1.8406409769E-01	-7.7533905742E-03	-2.2575831944E-03	9.7935902306E-02	1.000E+00	5.211E-01	

Figure 4.5: First lines of `.txt` file generated by CalcHEP.

4.3.1 Analytic and numerical results comparison

To test the agreement between the cross section values obtained using the analytic cross sections and the numerical calculations, I compare the analytical results with the one obtained using CalcHEP.

Fig. 4.6 shows the comparison between the analytic cross sections of the Bhabha scattering and the $e^+e^- \to \gamma\gamma$, with the simulated results produced by CalcHEP. Continuous line represents the analytic Bhabha T-channel cross section derived in equation 4.31, the dotted line the analytic Bhabha S-channel cross section derived in equation 4.50, and the dashed line the analytic $\gamma\gamma$-production cross section derived in the equation 4.75. Green squares show to the simulated Bhabha T-channel cross section values, red dots the simulated S-channel cross section values, and cyan triangles the simulated $\gamma\gamma$-production cross section.

The obtained values are in excellent agreement for all processes. The Bhabha T-channel scattering processes shows no dependence from $\sqrt{s}$ while the S-channel has a descending trend similar to the one of the $\gamma\gamma$-production. The absolute value of the T-channel cross section strongly depends on the infrared energy cut-off used for the calculation due to the infrared divergence. In the calculations reported in the following table an hard cut-off of 1 MeV has been used.
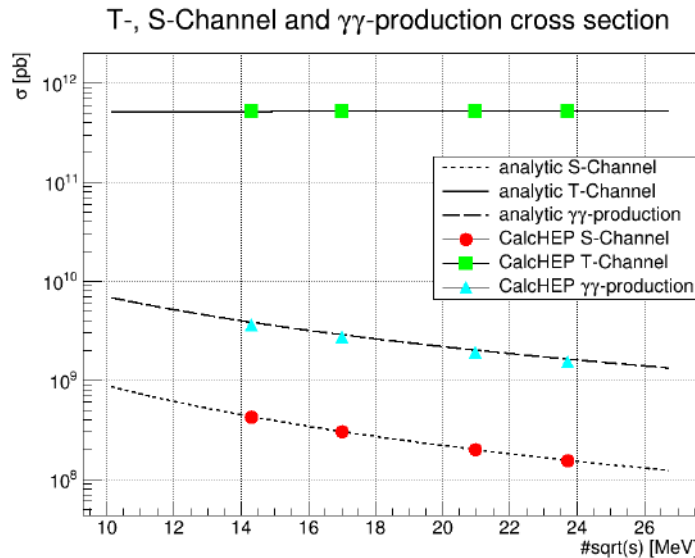

Figure 4.6: The analytic cross section versus the simulated. The plot shows the analytic Bhabha T-channel (continuous line) and the simulated (green square), the analytic Bhabha S-channel (dotted line) and the simulated (red points), and the analytic $\gamma\gamma$-production (dashed line) and the simulated (cyan triangle).

The four simulated cross sections for each processes are calculated at $\sqrt{s} = 14.31, 17, 20.98, 23.72$ MeV and they summarised in Tab. 4.1. The $\sqrt{s} = 17$ MeV is

the expected mass resonance of the X17 vector boson, the $\sqrt{s} = 20.98$ MeV and $\sqrt{s} = 22.72$ MeV correspond to the beam positron energy of $E_{beam} = 430$ MeV and $E_{beam} = 550$ MeV which are the ones considered during the Run I and II of the experiment [51]. The first value of $\sqrt{s} = 14.31$ MeV is chosen smaller than the other three to have a value for lower energies.

I test the $\sqrt{s}$ range between $\simeq 10$ MeV and $\simeq 25$ MeV where the mass of X17 is expected to be. The analytical trends work fine for the even much larger energy range, considering that I'm studying the process at the leading order only. It is possible to improve the results considering the next-to-leading order contributions. Each statistical error associated to the S-channel and $\gamma\gamma$-production

$\sqrt{s}$ [MeV]	σ_T [pb] $\times 10^{11}$	σ_S [pb] $\times 10^{8}$	$\sigma_{\gamma\gamma}$ [pb] $\times 10^{9}$
14.31	5.14 $\pm$0.02	4.26	3.64
17	5.16 $\pm$0.04	3.02	2.73
20.98	5.18 $\pm$0.04	1.98	1.91
23.72	5.18 $\pm$0.05	1.55	1.53

Table 4.1: CalcHEP simulated cross sections with its uncertainties. The errors of the S-channel and $e^+e^- \rightarrow \gamma\gamma$ cross sections are negligible.

processes are smaller by 5-order of magnitude with respect to the results, and they are not reported. Of course the described uncertainties are only statistical and the actual precision of the calculation is far from being that good. Next-to-leading order contributions are in fact expected to be order $\sim 5\%$ of the CalcHEP simulated values. For this reason to all the numbers in the table an absolute systematic uncertainty of $\sim 5\%$ needs to be assigned. Nevertheless, being both the analytical cross section and the CalcHEP calculation leading order ones, the agreement of the two, shown in Fig.4.6, is not significantly affected.

5 X17 and SM Background at PADME

SUMMARY OF THE CHAPTER. In this chapter I study the production of the X17 boson and I evaluate the SM background at PADME. I assume that the production process of the X17 particle is the same of the Bhabha S-channel, since both occur via annihilation processes. I study the three-momentum of the decay products and the energy distributions produced by CalcHEP to select geometrical and energy cuts to produce the best signal to background ratio.

5.1 X17 production with positron beams

The PADME experiment aims to produce the X17 boson exploiting the resonant production mechanism [54].

A low energy positron beam colliding on the electrons of a fixed Carbon thin target will be used. Following the experimental results of the ^{8}Be and ^{4}He anomaly [8, 26, 27, 29, 30, 55] different theoretical explanations have been carried out. From of the original ATOMKI measurement some features of the signal, which are model independent can be extracted:

- The mass of the new X17 particle is close to 17 MeV.

- X17 must decay mainly into e^+e^- and the electron coupling has only a lower limit

- The decay length should be smaller than $\sim$ cm, otherwise the anomaly would not be measured at ATOMKI escaping the apparatus.

Additional conclusions more model dependent are extracted in [9, 23, 33]:

- The X17 must have a strong couplings to the quarks to fit the strength of the excess, but the combination of the coupling to the up/down quarks (g_u

and g_d) must lead to pion-phobia to justify the absence of signal from the π^0 decay [34]

- The X17 interactions with the electron neutrino is constrained from the $\nu - e$ scattering experiment.

5.1.1   The X17 resonant production cross section

As a consequence of the previously listed constraints the X17 width for an electromagnetic-like decay into electron-positron pairs needs to be tiny. In this work I'll consider for X17 only the vector boson hypothesis, indicated by the subscript V. The width for the vector boson case is:

$$\Gamma_V = \frac{m_V \alpha_{EM} \varepsilon^2}{3} \simeq 0.5 \text{ eV} \left(\frac{g_{Ve}}{0.001} \right)^2 \tag{5.1}$$

where ε is the coupling constant of the new $U'(1)$ symmetry. The X17 production cross section can be expressed using a Breit-Wigner distribution as follow:

$$\sigma_{res} = \sigma_{peak} \frac{\Gamma_V^2/4}{(m_V - \sqrt{s})^2 + \Gamma_V^2/4} \tag{5.2}$$

where $\sigma_{peak} \equiv \frac{12\pi}{m_V^2}$ and $s = 2m_e E_{beam}$ is the centre of mass energy. The expression of the cross section in equation 5.2 is derived in [11]. Due to the tiny value of the ratio $\frac{\Gamma_V}{m_V} \ll 1$ equation 5.2 can be written introducing Dirac's delta function[1]:

$$\sigma_{res} = \sigma_{peak} \frac{\Gamma_V}{2m_V} \delta(1 - \frac{\sqrt{s}}{m_V}). \tag{5.3}$$

Using the resonant energy $E_{res} = \frac{m_V^2}{2m_e}$ and the explicit expressions for both Γ_V and σ_{peak}, the resonant cross section reads:

$$\sigma_{res} = \frac{2\pi \alpha \varepsilon^2}{m_e} \delta(E_{res} - E_{beam}). \tag{5.4}$$

The use of the the Dirac's delta function in the Breit-Wigner is allowed if the positron beam energy distribution is "dense" enough to be considered uniform on the scale of the width Γ_V. Moving to the laboratory frame the equation 5.3

---

[1]The δ of Dirac can be represented as a limit of the Cauchy succession: $\pi \delta(x) = \lim_{n \to 0^+} \frac{n}{x^2 + n^2}$ [56]

transforms into:

$$N_{tot} \int_{E_{res}-\frac{\Gamma_V m_V}{4m_e}}^{E_{res}+\frac{\Gamma_V m_V}{4m_e}} f(E)\, dE \simeq N_{tot} \frac{\Gamma_V m_V}{2m_e} f(E_{res}) \gg 1 \tag{5.5}$$

where $f(E)$ is the differential energy distribution of incoming positrons, $E_{res} = \frac{m_V^2}{m_e}$ and $\frac{m_V}{2m_e}$ comes out changing the energy interval of the Γ_V in the laboratory frame. From these assumptions and considering a thin target, the peak cross section is appreciably large

$$\sigma_{peak} \simeq 50\text{b} \times \left(\frac{17\,\text{MeV}}{m_V}\right). \tag{5.6}$$

5.1.2 The number of produced X17 using PADME like setup

In this section I estimate the number of produced X17 considering an experimental setup like the one adopted for the PADME *Run III* in 2022. To assume that the cross section is close to the resonance value, the target thickness needs to be small to avoid significant energy losses by primary positrons. In a Carbon target of $\simeq 100\ \mu$m (see chapter 3.2.1) the energy loss for an incoming positron is ~ 0.1 MeV. For the X17 particle the width at the resonance in terms of the laboratory frame positron energy has the following expression:

$$\frac{\Gamma_V m_V}{2m_e} \sim 10\ \text{eV} \times \left(\frac{g_{Ve}}{0.001}\right), \tag{5.7}$$

a positron having the exact resonant energy will keep that value of energy only for a lenght L of the order

$$L \sim 10\ \text{nm} \times \left(\frac{g_{Ve}}{0.001}\right). \tag{5.8}$$

Therefore considering a target of thickness δl, the probability of creating an X17 boson implies that the positron energy is $E' \pm \delta E$, being δE related to Γ_V. For each positron in the beam, the probability is given by:

$$\text{P}(E') = \frac{\delta E}{\Delta E}\,\text{P}^{X17}(E') \tag{5.9}$$

where ΔE is the beam energy spread (order of one MeV) and the $\text{P}^{X17}(E')$ is the creation probability, defined as:

$$\text{P}^{X17}(E') = 1 - e^{-Ln_e^{tar}\sigma_{full}(E')} \tag{5.10}$$

where $n_e^{tar} = \frac{N_a \rho Z}{A}$ corresponds to the target electron density. The actual cross section value for the X17 production ($\sigma_{full}(E')$) is a more complex function, since it also includes NLO order effects (see [54]).

Being this study aimed to estimate a preliminary experiment sensitivity NLO are beyond the scope of this work and only tree level processes will be considered.

Including total number of impinging positrons (N_{tot}), the probability that a X17 is produced in a thickness L of the Carbon target, by a positron having energy in the range δE centred around the resonance energy, is given by the following Poisson distribution

$$N_{tot} \frac{\delta E}{\Delta E} \times \mathrm{P}_{X17}(E') \simeq \frac{\delta E}{\Delta E} N_{tot} n_e^{tar} \sigma_{full}. \tag{5.11}$$

Since for each thickness of target of typical length L (see 5.8) the positron energies are essentially randomly re-shifted by straggling, I can sum the Poisson distribution for each thickness in the target and for each energy range δE.

The integration over the entire target and over all possible positron energies leads to the total number of produced X17, which follows the Poisson distribution. The mean expected number of events is then:

$$N_V = N_{tot} \frac{N_a \rho Z}{A} \delta l \int dE \frac{df(E_{beam})}{dE} \sigma_{full}(E) \tag{5.12}$$

where the $\frac{df(E_{beam})}{dE}$ is the full differential distribution of the beam energy, which is not modified significantly, because for the PADME case $L = 100 \mu m \ll$ of the Carbon radiation length.

The last equation can be integrated assuming that the positron beam energy is close to the resonant energy $E' = E_{res} = 282$ MeV, and that the beam energy spread is Gaussian. The result of this integration is:

$$N_{tot}^{X17} \simeq \mathrm{N}^{PoT} 3.8 \cdot 10^{-7} \times \left(\frac{g_{V_e}}{3 \cdot 10^{-4}}\right)^2 \left(\frac{\delta l}{100 \ \mu\mathrm{m}}\right) \left(\frac{N_a \rho Z}{A \ 10^{24}}\right) \left(1 \ \mathrm{MeV} \times \sqrt{2\pi} \frac{\partial f(E_{beam})}{\partial E}\right). \tag{5.13}$$

The last term of 5.13 depends on a single parameter which represents the beam energy spread δE. The Gaussian variance is:

$$\frac{\partial f(E_{beam})}{\partial E} = \frac{1}{\sqrt{2\pi}\delta E} e^{\frac{(E_{res} - E_{beam})^2}{2\delta E^2}}. \tag{5.14}$$

This expression is valid at the level of few percent over the full parameter's range

relevant for PADME and provided that the width of the resonance is very small compared to the beam energy spread and that the dominant mode of production is resonant production (in particular, the pure off-shell component is not included).

5.2   The background events

The main background source to the X17 resononat production process $e^+e^- \to X17 \to e^+e^-$ is the Standard Model Bhabha scattering and two photons annihilation. The former has a final state identical to the signal while for the latter the identification of photons allows complete rejection.

Both reactions have been simulated using the CalcHEP package (see section 4.3). Samples of 10^6 events for the Bhabha T- and S-channel, respectively, and for the $\gamma\gamma$-process have been generated. Being the process ad $2 \to 2$ the four-momenta of final state particles are indicated with the 3 and 4 subscript indices:

$$p_3 = (E_3, P3_1, P3_2, P3_3) \,, \; p_4 = (E_4, P4_1, P4_2, P4_3) \tag{5.15}$$

where Pi_j are the three-momentum component given by CalcHEP, and $i = 3, 4$ refers to the first and second final state particle, namely the electron and the positron or one of the two photons. $j = 1, 2, 3$ are the spatial components and I label them p_x, p_y, p_z. By definition, the final three-momentum is $\boldsymbol{p} = \sqrt{p_x^2 + p_y^2 + p_z^2}$, and the energy is $E = \sqrt{m_e^2 + \boldsymbol{p}^2}$.

The three-momentum and energy distributions for both T- and S-channel Bhabha scattering and for the $\gamma\gamma$-production are shown in Fig. 5.1. Fig. 5.1a shows the distributions of the final three-momentum normalised to the total number of events of all three processes: the green histogram is refers to the T-channel, the red to the S-channel and the cyan to the $\gamma\gamma$-production.

Fig. 5.1b shows the distributions of the final energies normalised to the total number of events of the same processes, according to the same colour convention.

It is possible to see that in the middle part of the graphs the T-channel number of events is lower by a factor ~ 15 with respect to the S-channel and $\gamma\gamma$ production as expected. The $\gamma\gamma$-production has a symmetric trend due to the identical final state particles.
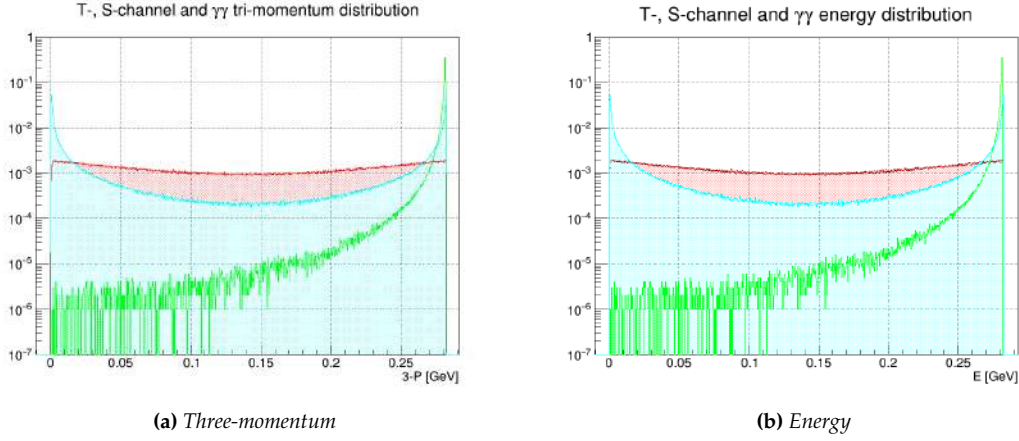
(a) *Three-momentum*   **(b)** *Energy*

Figure 5.1: The final three-momentum and energy distribution. T-channel (green), S-channel (red), $\gamma\gamma$-production (cyan).

In the laboratory the ϑ emission angle of each particle can be obtained as follow:

$$\tan(\vartheta_{x,y}) = \frac{p_{x,y}}{p_z} \tag{5.16}$$

where p_z lies on the beam axis. The impact point of the particle on the PADME calorimeter can be extrapolated:

$$X_{ECAL}, Y_{ECAL} = \tan(\vartheta_{x,y})\Delta Z \tag{5.17}$$

where $\Delta Z = 3500$ mm, is the distance between the target and the calorimeter along the beam direction. A convenient variable to define ECAL acceptance cut is the impact radius of a particle define as:

$$R = \sqrt{X_{ECAL}^2 + Y_{ECAL}^2} \tag{5.18}$$

I will use this variable to determine the geometry cuts.

The impact point position is defined by the equation 5.18. Fig. 5.2 shows six different graphs, two for each process. They represent the number of events of each process as a function of R in mm. Each pair of graphs in Fig. 5.2 are associated to the positron and electron of the Bhabha scattering and the two photons of the $\gamma\gamma$-production. The top left green histogram represents the distribution of the T-channel positrons and the bottom represents that of the T-channel electrons; the top centre red histogram represents the distribution of the S-channel positrons and the bottom is that of the S-channel electrons; the top right cyan histogram represents the distribution of the first photon produced in the $e^+e^- \rightarrow \gamma\gamma$ reaction and the bottom is that of the second photon. The positrons produced by the

scattering process occupy the centre of the calorimeter, as anticipated in the section 4.1.1 while the electrons are evenly spread. The distribution of the positrons and electrons coming from the annihilation process is almost the same and it is almost flat; both photons have almost the same distribution.
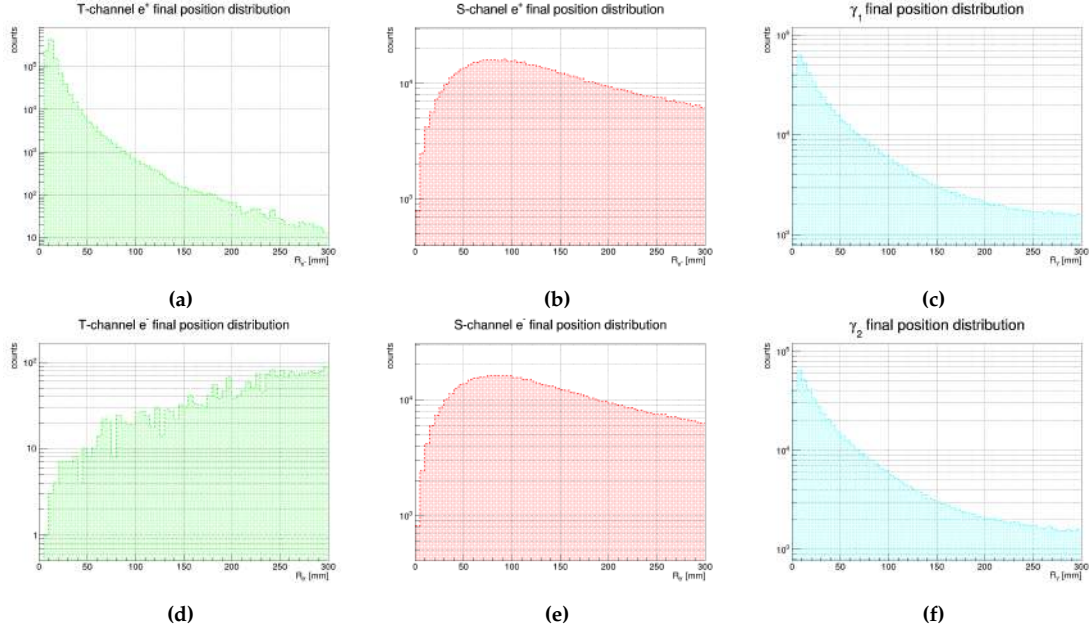

Figure 5.2: The events number as a function of $R_{e^+,e^-,\gamma}$ for all of three processes considered. The number of T-channel positron (top left green histogram) and electron (bottom left green histogram); the number of S-channel positron (top centre red histogram) and electron (bottom centre red histogram); the number of the first γ produced by the $e^+e^- \to \gamma\gamma$ reaction (top right cyan histogram) and the second (bottom right cyan histogram).

5.3 Calorimeter coordinates distributions

To reconstruct the X17 the invariant mass of the four momentum of both e^+e^- final states particles is needed. This condition requires that both final state particles impact on the ECAL fiducial volume.

To study the distribution of the impact point positions of the e^+e^- on the calorimeter surface for the different background sources, we produced the corresponding scatter plots.

Fig. 5.3 shows the impact position of each final particle at a distance $\Delta L = 3500$ mm from the target. Fig. 5.3 is composed by six different graphs, two for the T-channel processes (on the left), two for the S-channel (centre) and two for the $\gamma\gamma$-production (on the right). The first and the second graphs are related to the impact position of the positrons coming from the Bhabha scattering, the fourth and the fifth to the impact position of the electrons. The impact position of the

photons are shown in the last column. Being identical particles, they are labelled γ_1 and γ_2. From these graphs one notices that the final tracks distribution is similar for Bhabha S-channel and $\gamma\gamma$-production, since both are annihilation processes. The T-channel shows a hole in the centre of the calorimeter due to the energy cut which excludes events at forward angles.

Analysing these graphs, I can determine geometry and energy cuts. My goal is to find a set of cuts which minimise the background, but at the same time, I want to evaluate the T- and, especially, the S-channel acceptance separately. This is due to the fact that the production of X17 occurs through an annihilation process. I define the geometry cut considering ECAL dimensions that are $R_{min} = 90$ mm and $R_{max} = 270$ mm. and scanning on the bigger R_{max} and viceversa, scanning on R_{min} and fixing $R_{max} = 270$ mm. I look for the portion of calorimeter which satisfy what I guessed above, so I require the radiuses R_{e+} and R_{e-} both will be greater than R_{min} and smaller than R_{max}. This condition has to be fulfilled simultaneously by both tracks because during the experiment the magnet is turned off, contrary to previous runs [51], therefore I can not distinguish electrons by positrons. Hence the geometry cut is:

$$R_{min} < R_{e+} < R_{max} \text{ and } R_{min} < R_{e-} < R_{max} \tag{5.19}$$

where 180 mm $< R_{max} <$ 280 mm and 80 mm $< R_{min} <$ 235 mm. The R_{max} range is 100 mm and it is divided in 21 equal intervals of 5 mm, while the R_{min} range is 155 mm and it is divided in 32 equal intervals of 5 mm. Fig. 5.4 shows the occupancy after a geometry cut, characterised in this case by $R_{min} = 90$ mm and $R_{max} = 270$ mm. The figure is composed by six different graphs, collected according to the same convention in Fig. 5.3. Each graph has a hole in the centre true to the calorimeter and it is possible to see, after this first cut, how the occupancy of the T-channel events is descreasead significantly.

Now I add an energy cut, which requires particles have a minimal value of the final energy. I require each particle to have energy greater than E_{min}, until $E_{min} = 140$ MeV, which is imposed by the kinematics. The E_{min} is considered between 70 MeV and 140 MeV divided in 28 equal intervals of 2.5 MeV. Fig. 5.5 shows the occupancy of the calorimeter after a geometry cut with $R_{min} = 90$ mm, $R_{max} = 270$ mm and after an energy cut with $E_{min} = 100$ MeV. The figure is composed by six different graphs, collected according to the same convention in Fig. 5.3. The magnitude of the occupancies after this cut are almost the same of the ones in Fig. 5.4: I will analyse this behaviour in the next sections, anyway, with these graphs

I will be able to study which is the best acceptance of the calorimeter, maximising the number of possible candidates and minimising the SM background.
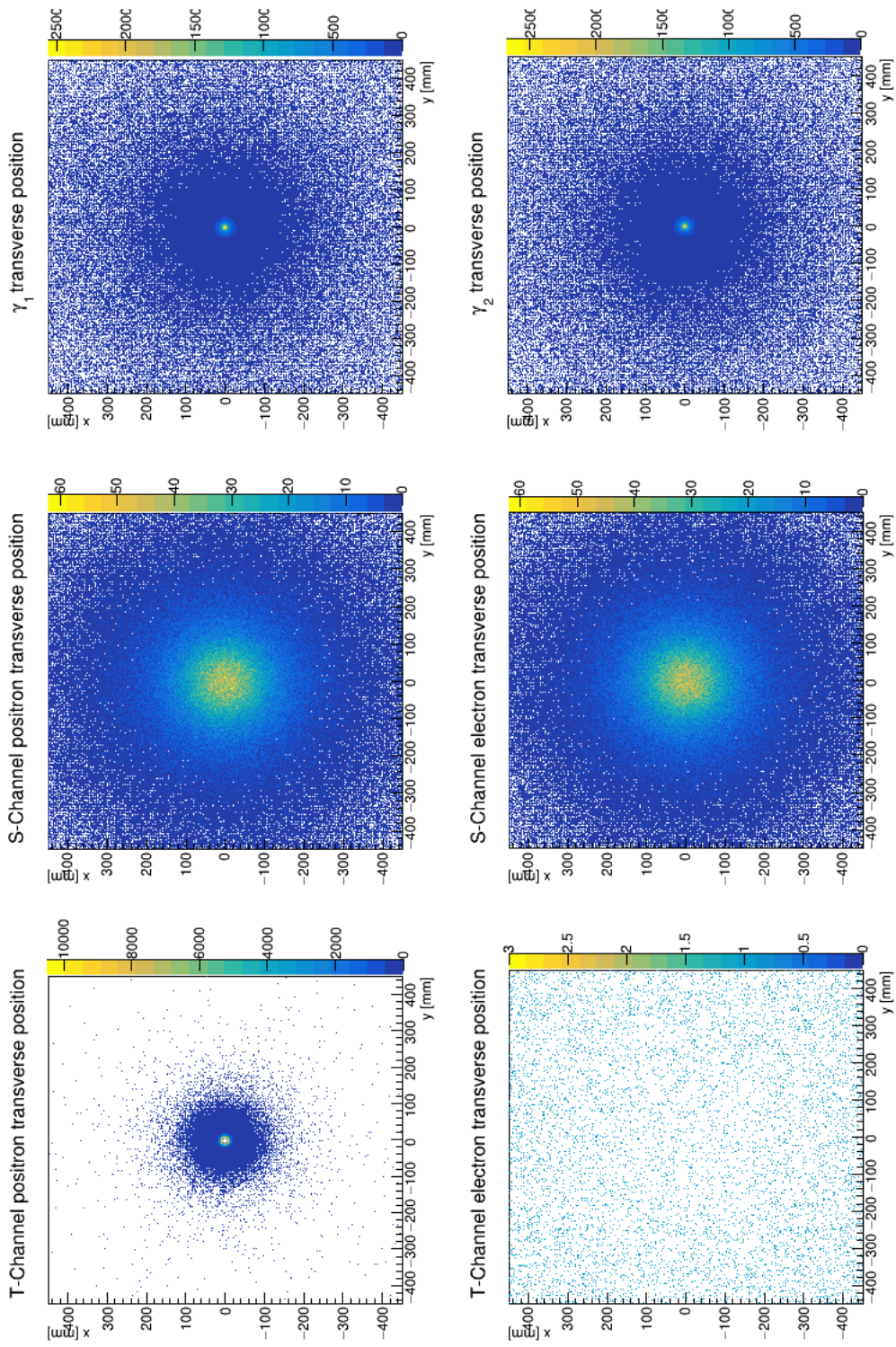
Figure 5.3: The calorimeter occupancy for all of three processes. Each graph corresponds to one channel: S-channel (first column), T-channel (second column), $e^+e^- \rightarrow \gamma\gamma$ (third column). For the S- and T-channel there is the occupancy of the positron in first line and the electron one in the second. For the $\gamma\gamma$-production I identify the two photons as γ_1 (top right plot) and γ_2 (bottom right plot).
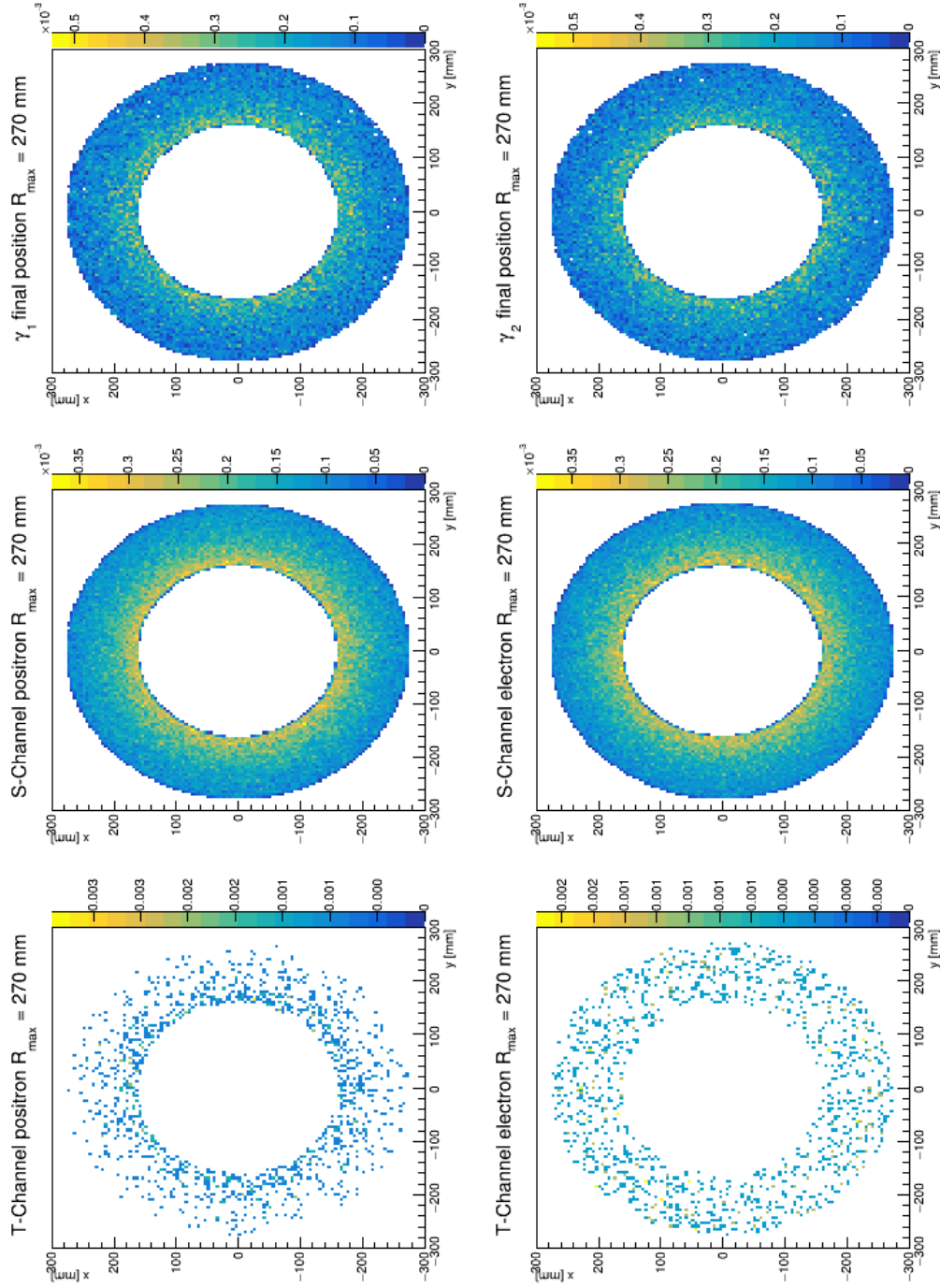
Figure 5.4: The calorimeter occupancy for all of three processes into a ring with $R_{min} = 90$ mm and $R_{max} = 270$ mm. Each graph corresponds to one channel: S-channel (first column), T-channel (second column), $e^+e^- \to \gamma\gamma$ (third column). For the S- and T-channel there is the occupancy of the positron in first line and the electron one in the second. For the $\gamma\gamma$-production I identify the two photons as γ_1 (top right plot) and γ_2 (bottom right plot).
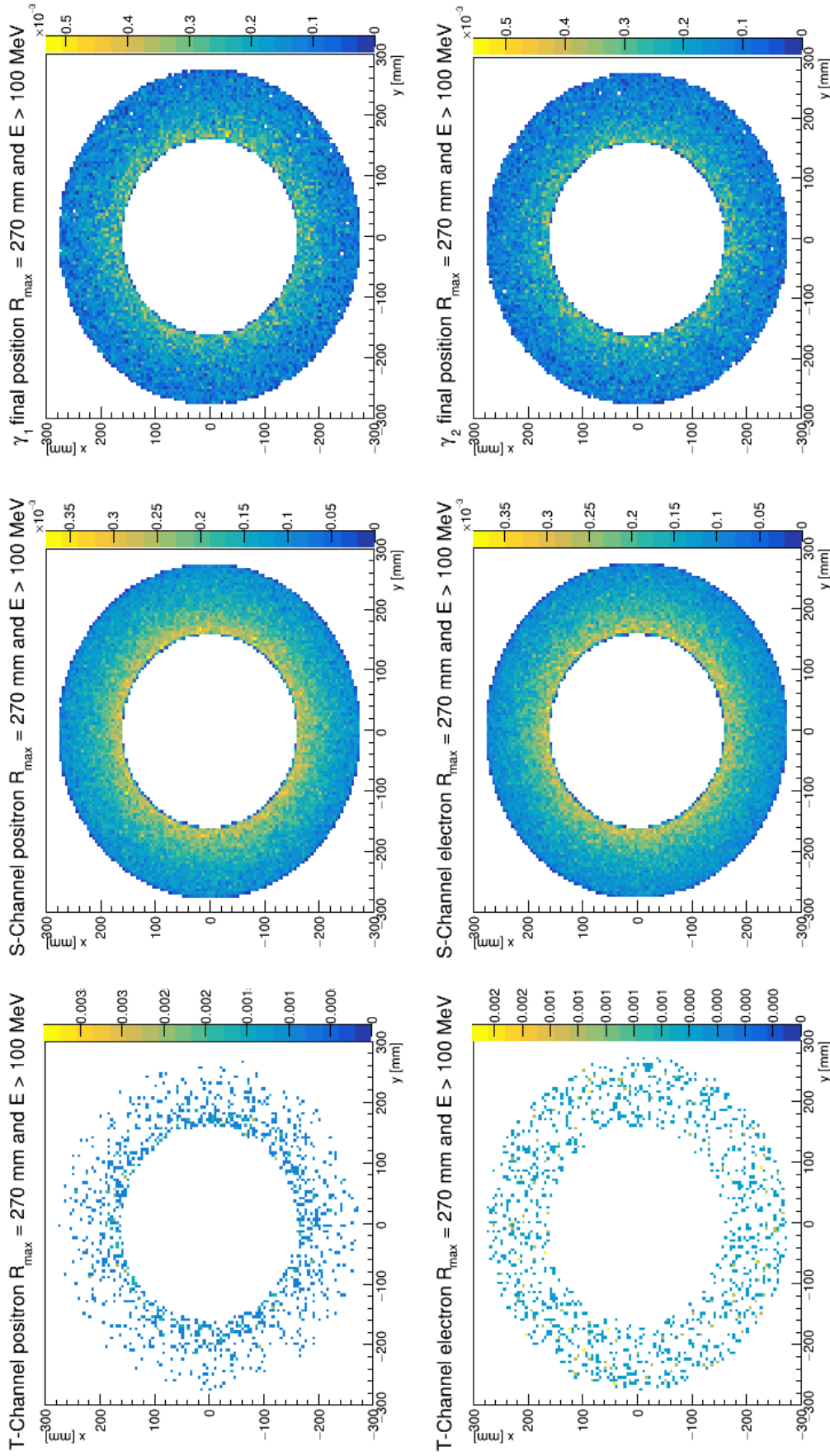
Figure 5.5: The calorimeter occupancy for all of three processes into a ring with $R_{min} = 90$ mm and $R_{max} = 270$ mm and $E_{e+,e-} > 30$ MeV. Each graph corresponds to one channel: S-channel (first column), T-channel (second column), $e^+e^- \rightarrow \gamma\gamma$ (third column). For the S- and T-channel there is the occupancy of the positron in first line and the electron one in the second. For the $\gamma\gamma$-production I identify the two photons as γ_1 (top right plot) and γ_2 (bottom right plot).

5.4 Acceptance of each process

In this section I evaluate the acceptance of the calorimeter as a function of E_{min}, R_{min} and R_{max} combining different sets of cuts. I calculate the ratio between the number selected events (N_{det} cut), over the total number of simulated events N_{tot}. The acceptance is defined as follow:

$$Acc(R_{max}, R_{min}, E_{min}) = \frac{N_{det}}{N_{tot}}. \tag{5.20}$$

I test the acceptance in the range of R_{max}, R_{min} and E_{min} illustrated in the previous section and I do it for T-, S-channel and the $\gamma\gamma$-production separately.

To compare background rejection factors for the two dominant background contributions, at the chapter I make the ratio between the S-channel and T-channel acceptances. This parameter is used to evaluate what is the best possible set of cuts. The ratio is defined as follow:

$$\mathcal{Q}_{Acc} = \frac{Acc_S\,(R_{max}, R_{min}, E_{min})}{Acc_T\,(R_{max}, R_{min}, E_{min})} \tag{5.21}$$

5.4.1 T-channel acceptance

Fig. 5.6 shows three 2-D histograms with the T-channel acceptance of the calorimeter as a function of R_{max}, R_{min} and E_{min}. In the top histogram I scan on R_{max} and E_{min} and I keep fixed $R_{min} = 90$ mm, in the bottom left histogram I scan on R_{min} and E_{min} and I keep fixed $R_{max} = 270$ mm and in the bottom right histograms I scan on R_{max} and R_{min} I keep fixed $E_{min} = 100$ MeV. The R_{max} range tested in these graphs is a bit smaller than the introduced in the previous chapter, because at those angles there are not any selected tracks. This is due to the constraint imposed by the kinematic. Namely, the R_{max} range considered in these graphs is 220 mm $< R_{max} < 280$ mm. The R_{min} range is smaller than the introduced above for the same reason, namely 80 mm $< R_{max} < 215$ mm.

The light yellow areas are characterised by the higher acceptance, while the dark blue by the lower. I look for the lowest possible T-channel acceptance to minimise the SM background, so I am interested to the dark areas, which are characterised by $Acc_T \simeq 0.02\%$, anyway, the lightest have $Acc_T \simeq 0.12\%$, that is only greater than a factor 6, but in that areas the statistics is much larger.
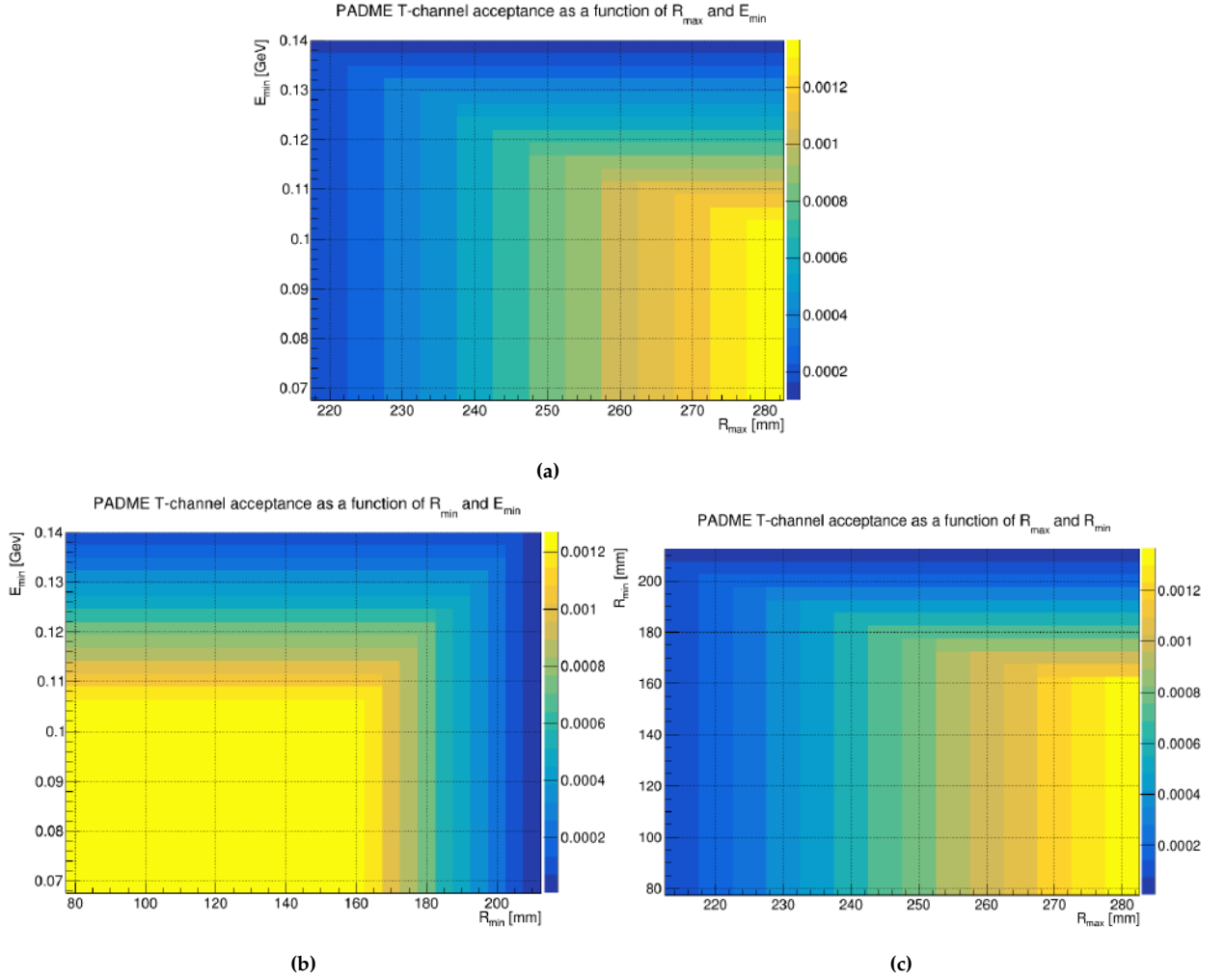
Figure 5.6: The calorimeter T-channel acceptance. The top centre histogram is a scan on R_{max} and E_{min} with $R_{min} = 90$ mm; the bottom left is a scan on R_{min} and E_{min} with $R_{max} = 270$ mm; the bottom right is a scan on R_{min} and R_{max} with $E_{min} = 100$ MeV.

5.4.2 S-channel acceptance

Fig. 5.7 shows three 2-D histograms with the S-channel acceptance of the calorimeter as a function of R_{max}, R_{min} and E_{min} collected according to the same convention in Fig. 5.6. The R_{max} and R_{min} range tested in these graphs are the same of the previous section for the same reason above.

In this case I am interested to the yellow areas, which are the ones that reproduce the production mechanism of X17. In this areas the acceptance is bigger than the T-channel by a factor of ~ 150.
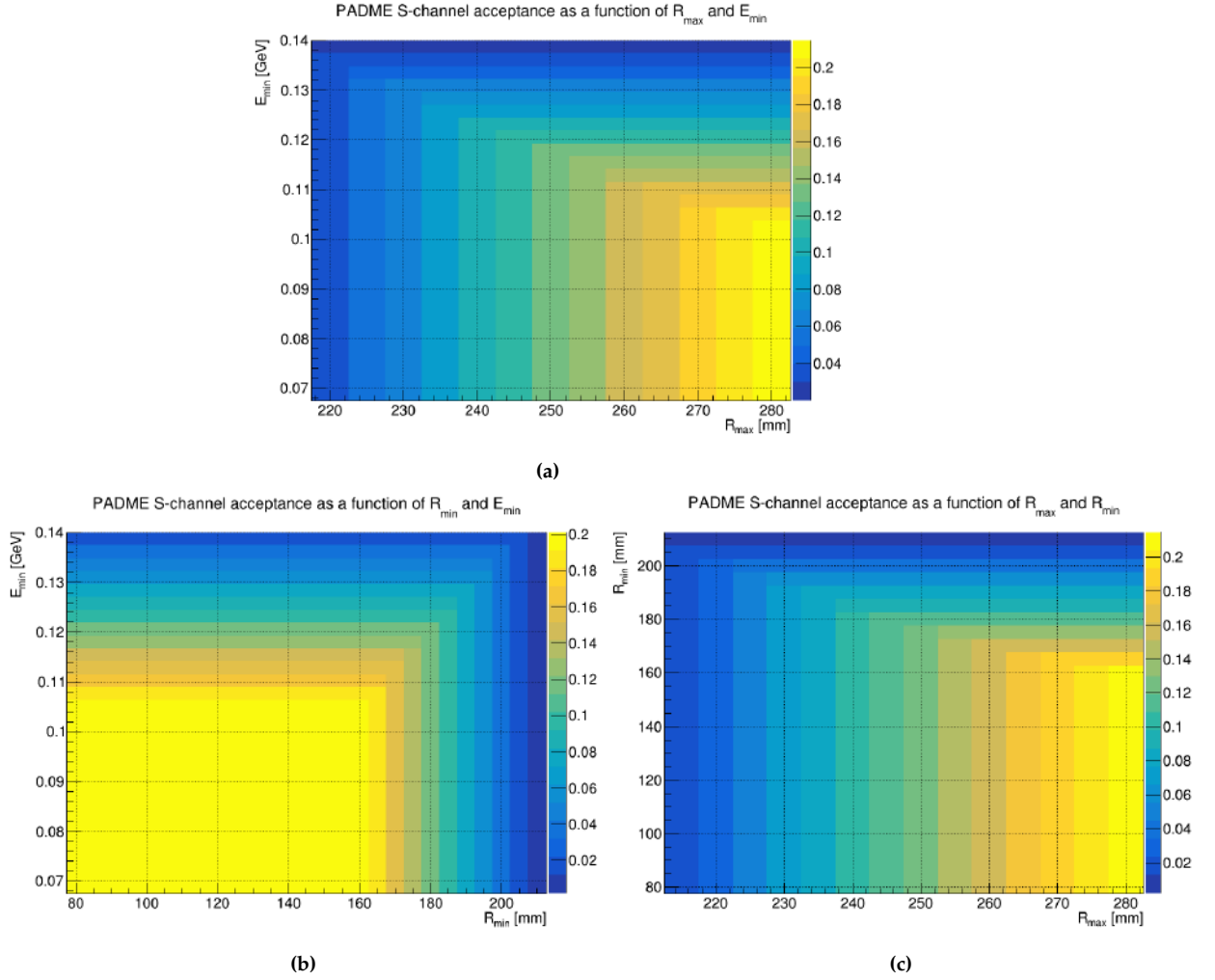
(a)

(b)   (c)

Figure 5.7: The calorimeter S-channel acceptance. The top centre histogram is a scan on R_{max} and E_{min} with $R_{min} = 90$ mm; the bottom left is a scan on R_{min} and E_{min} with $R_{max} = 270$ mm; the bottom right is a scan on R_{min} and R_{max} with $E_{min} = 100$ MeV.

5.4.3 $e^+e^- \rightarrow \gamma\gamma$ acceptance

Fig. 5.8 shows three 2-D histograms with the $\gamma\gamma$-production acceptance of the calorimeter as a function of R_{max}, R_{min} and E_{min} collected according to the same convention in Fig. 5.6. The R_{max} and R_{min} range tested in this graphs are the same of the previous section for the same reason above.

The acceptance of the two photons is meaningful but assembling the electron tagger (see chapter 3.3) in front of the calorimeter it is possible to distinguish the photon by the electrons. This component of the apparatus eliminates almost all of the background coming from the $e^+e^- \rightarrow \gamma\gamma$ process. Since the radiation length of the plastic scintillator is $X_0 = 430$ mm and its thickness is $l = 5$ mm, a photon impinging on the ETagger decays into a electron-positron pair with

probability:

$$P(\gamma \to e^+ e^-) = 1 - e^{-\frac{l}{X_0}} \simeq 0.011 \tag{5.22}$$

and this decay must occur simultaneously for each emitted photon, then the probability that a $e^+ e^- \to \gamma\gamma$ is detected as a pair of leptons is the convolution of the probability

$$P(\gamma \to e^+ e^-) \times P(\gamma \to e^+ e^-) \simeq 0.01\%. \tag{5.23}$$

So therefore, the $\gamma\gamma$-production background contribution is suppressed by a factor 10^{-4} making absolutely negligible, due to the presence of the Etagger.
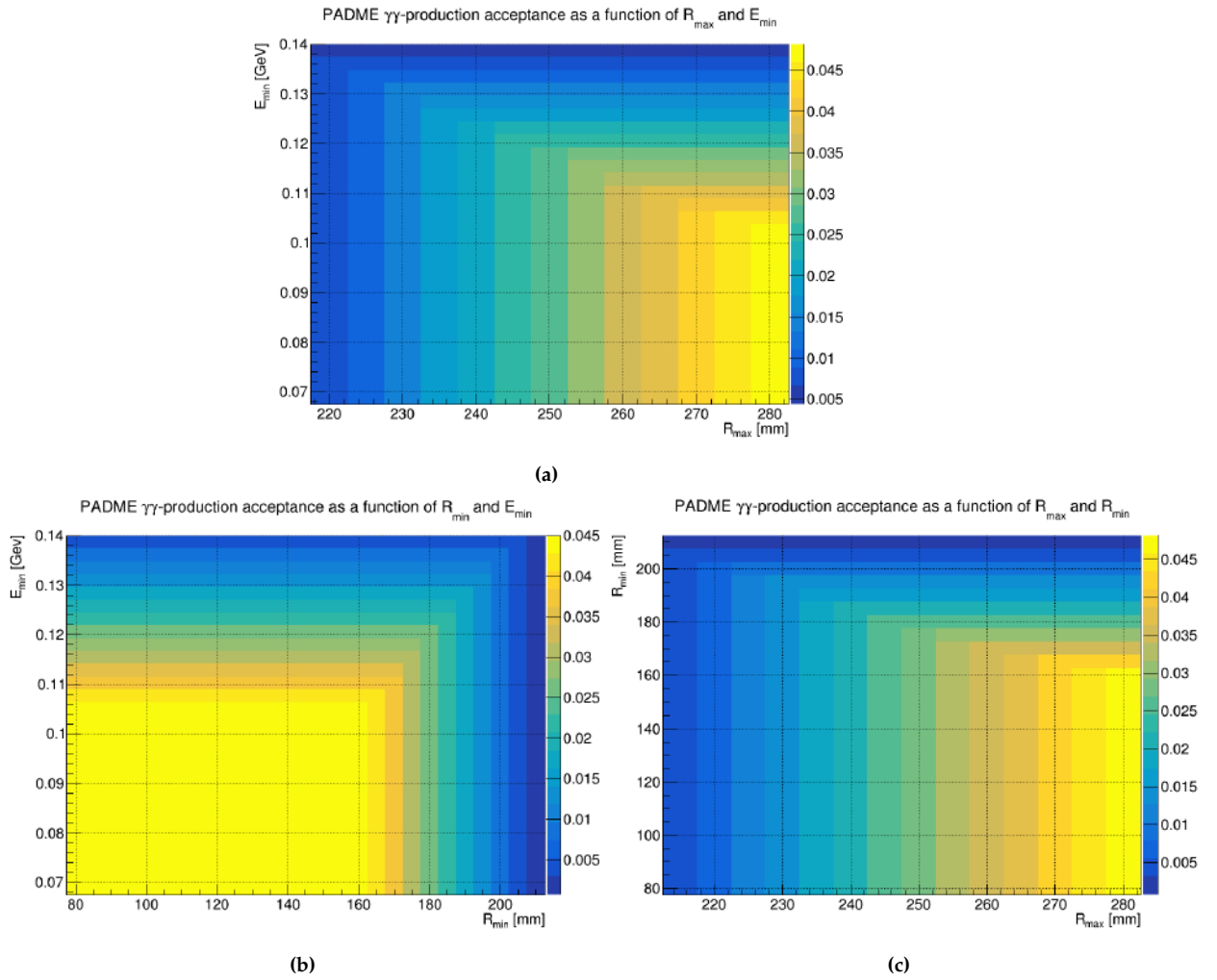
(a)

(b)

(c)

Figure 5.8: The calorimeter $\gamma\gamma$ acceptance. The top centre histogram is a scan on R_{max} and E_{min} with $R_{min} = 90$ mm; the bottom left is a scan on R_{min} and E_{min} with $R_{max} = 270$ mm; the bottom right is a scan on R_{min} and R_{max} with $E_{min} = 100$ MeV.

5.4.4 S-channel and T-channel acceptances comparison

To identify the best set of geometry and energy cuts, I evaluate the ratio $\mathcal{Q}_{Acc}$ between S-channel and T-channel acceptance, defined in the equation 5.21, as a function of R_{max}, R_{min} and E_{min}. Fig. 5.9 shows three 2-D histograms with the $\mathcal{Q}_{Acc}$ as a function of all of three possible pair of set of cut considered above, according to the same convention in Fig. 5.6. The range of the variables are the same which I considered in Fig. 5.6.

The $\mathcal{Q}_{Acc}$ variable has the higher values at high values of minimal energy, at small R_{max} and big R_{min}. The yellow areas at high values of minimal energy would represent the best choice of energy cut, but it would involve a poor statistics, so I guess the best energy choice is about $E_{min} = 100$ MeV, as fixed in the third histogram in Fig. 5.9. Focusing on this histogram, I exclude the area corresponding to small R_{min} and big R_{max} because there is a large contribution of the T-channel events to the background, since to also avoid issue due to the statistics , I guess a good choice of geometry cut is the one characterised by $R_{min} = 190$ mm and $R_{max} = 270$ mm. Since these suggestions I will study the sensitivity of PADME to the production of X17 boson vector with two different acceptance choices, the one done above and one with R_{min} smaller. I will study the sensitivity with two different choices of acceptance, since the quantities which will be analysed in the next sections will depend on the acceptance in a competitive mode.
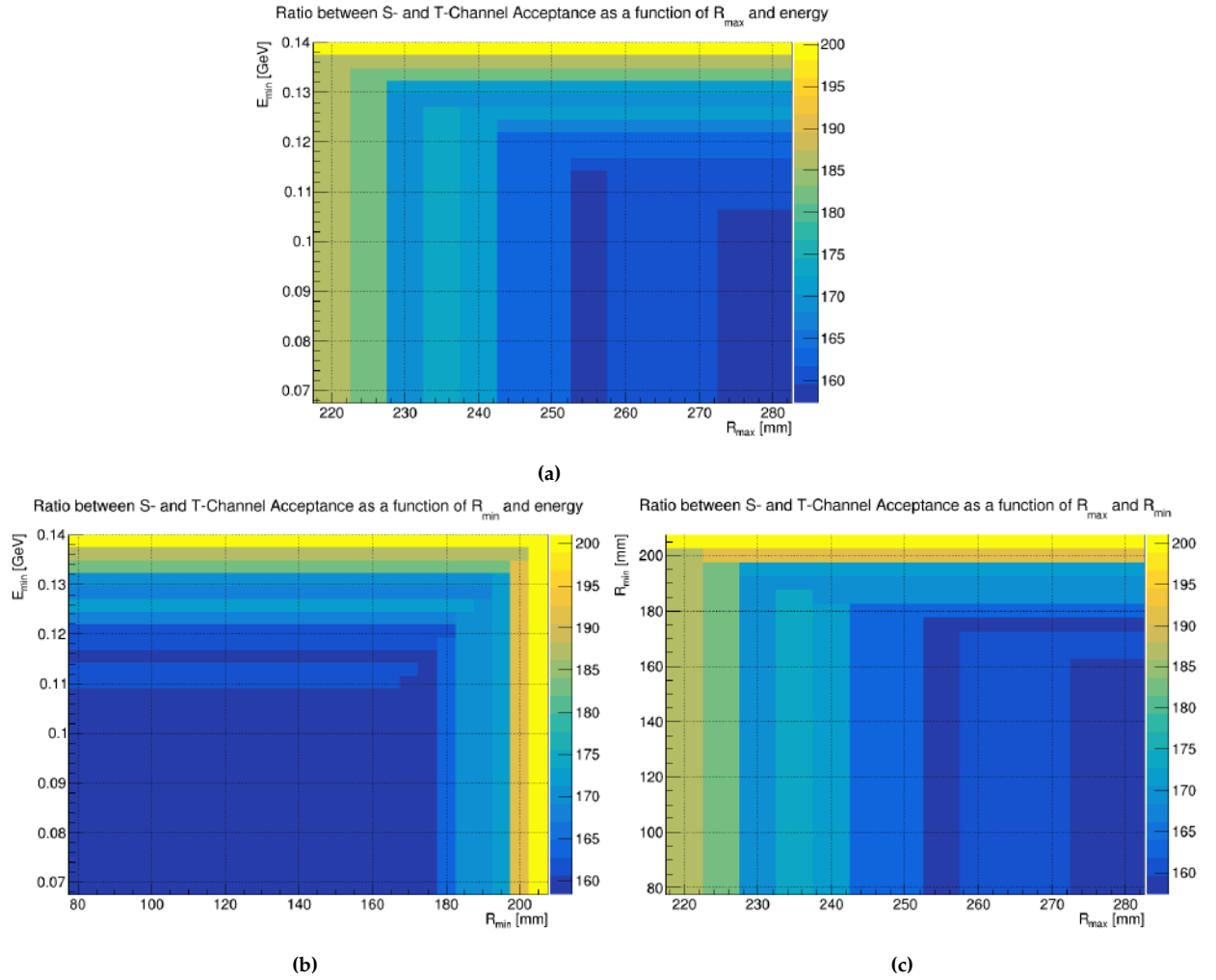
(a)

(b)

(c)

Figure 5.9: The ratio Q_{Acc} as a function of R_{max}, R_{min} and E_{min}. The top centre histogram is a scan on R_{max} and E_{min} with $R_{min} = 90$ mm; the bottom left is a scan on R_{min} and E_{min} with $R_{max} = 270$ mm; the bottom right is a scan on R_{min} and R_{max} with $E_{min} = 100$ MeV.

6 PADME sensitivity in resonant mode

SUMMARY OF THE CHAPTER. In this chapter I'll derive the total number of detected background and signal events. After estimating PADME experiment's luminosity and the total number of produced events, they are scaled for the acceptances obtained in the previous chapter. I study the sensitivity, which depends on the production with respect to the background. Since the production and the background are related to the acceptance in a competitive way, I take into account two different choices of cuts to evaluate the significance of the X17 boson vector production. Therefore, I make exclusion plots to try to understand the total number of Positron on Target needed to have enough statistic and, as conclusion of the chapter, I evaluate what is the magnitude of the coupling that is possible to discover with experimentally.

6.1   Estimating the number of background events

To evaluate the sensitivity of the experiment and produce the exclusion plots, the total number of candidate events detected by the calorimeter within a defined set of the geometry and energy cuts is needed.

We consider as a candidate event an electron positron pair detected in the calorimeter fiducial region, generated by a SM process or mediated by X17 boson. The equation used to derive the total number produced candidate events is:

$$N_{tot}^{prod} = \sigma \, \mathcal{L} \, \mathrm{N}^{PoT} \qquad (6.1)$$

where the $\mathcal{L}$ is the absolute luminosity of the experiment and the N^{PoT} is the total number of Positron on Target collected during a data taking point. To compute the number of detected events, equation 6.1 is scaled for the acceptance of each different candidate source. The detected candidate events number is then simply:

$$N_i^{det} = N_{tot}^{prod_i} \times Acc_i \qquad (6.2)$$

This quantity is derived separately for the Bhabha T-channel and S-channel, and for the $\gamma\gamma$-production.

The luminosity per single positron on target $\mathcal{L}$ is:

$$\mathcal{L} = \frac{N_a Z \rho \delta l}{A} K = 0.01054 \, \text{b}^{-1} \tag{6.3}$$

where $N_a = 6.022 \cdot 10^{23}$ is the Avogadro number, $\delta l = 0.01$ cm is the target's thickness and $Z = 6$, $A = 12 \, \text{g}^{-1}$, $\rho = 3.5 \, \frac{\text{g}}{\text{cm}^3}$ are the number of protons, the mass number and the mass density of the target respectively. I used the constant $K = 10^{-24}$ to convert the units from cm^{-2} to b^{-1}.

The total number of Positron on Target collected, N^{PoT}, is defined as:

$$\text{N}^{PoT} = \text{N}_{bunch}^{PoT} N_{bunch} t \tag{6.4}$$

where N_{bunch}^{PoT} is the number of Positron on Target for each bunch of the beam, N_{bunch} is the number of bunch and t is the time, measured in seconds. In standard running conditions $N_{bunch} = 49$, while the value of N_{bunch}^{PoT} will be decided after beam commissioning test and is assumed in this work to be order of few thousands. In this chapter I will study the number of Positron on Target needed to explore the X17 allowed parameter space.

6.2 PADME discovery potential

To explore the experiment discovery potential is necessary to compare the number of potential X17 signal events to the number of expected SM background events. The discovery potential is defined as the ratio between the number of X17 produced by the experiment, over the square root of the sum of background and X17 candidates as follow:

$$\tilde{S} = \frac{N_{X17}}{\sqrt{N_{X17} + N_{BG}}} \tag{6.5}$$

where $N_{BG} = N_{Sch} + N_{Tch}$ and the number of the T- and S-channels are computed in the equation 6.1.

It's important to stress that the assumption that $N_{BG} = N_S + N_T$ produces a slightly overestimated background value. In fact the complete Bhabha cross section actually includes an interference term which happens to be negative. Therefore the total cross section would result to be lower than the sum of S- and T-

channels contribution. In fact, the sum of the cross section of the T- and S-channels at $\sqrt{s} = 17$ MeV in Table 4.1 is greater than the $\sigma_{Bhabha} = (5.11 \pm 0.03) \cdot 10^{11}$ pb (calculated with CalcHEP). The overestimation is in any case of order few percent and is not an issue for the purpose of this analysis. Moreover the effect is partially compensated by the fact that the cross section obtained by CalcHEP is a tree level calculation, actually smaller with respect to the full next to leading order calculation.

The cross section for the resonant production of X17 has been derived in [54]. The number of produced X17, as a function of the total number of Positron on Target, is described by equation 5.13:

$$N_{tot}^{X17} = \text{N}^{PoT} 3.8 \cdot 10^{-7} \times \left(\frac{g_{V_e}}{3 \cdot 10^{-4}}\right)^2 \left(\frac{\delta l}{100\mu\text{m}}\right) \left(\frac{N_a \rho Z}{A 10^{24}}\right) \left(1 \text{ MeV} \times \sqrt{2\pi} \frac{\partial f(E_{beam})}{\partial E}\right) \tag{6.6}$$

where $\frac{\partial f(E_{beam})}{\partial E}$ is defined in equation 5.14 and the Gaussian variance is $\delta E = 0.7$ MeV.

I will study the discovery potential at the resonant energy $E_{res} = E_{beam}$ as a function of N^{PoT} and the coupling g_{Ve} of X17 with electrons into a fixed range. I will show the discovery potential in terms of coupling for each collected N^{PoT} to guide the data taking luminosity request.

During data taking there is no way of identify the X17 events from the SM produced $e^+ e^-$ pairs, therefore N_{X17} will be obtained as the deviation of the number of measured candidates N_{Cand} with respect the expected SM background N_{BG}.

$$N_{X17} = N_{Cand} - N_{BG} \tag{6.7}$$

If there is no new physics effect the measured $N_{X17} = 0$ due to $N_{Cand} = N_{BG}$, on the contrary we need to establish if the estimated N_{X17} is or not compatible with 0. The error on the number of candidates $N_{Cand} = N_{BG} + N_{X17}$ is assumed to be Poissonian so that its RMS is the square root of the N_{Cand} itself. The error on N_{BG} is assumed to be negligible being the MC statistics much higher than the one on the data sample.

To simulate the experimental conditions the acceptance of each process is computed separately as described in chapter 5. Concerning the X17 acceptance, it is assumed to be identical to the one of the Bhabha S-channel because the kinematic of the two processes is the same: X17 is a vector boson of 17 MeV mass produced

via the annihilation process, exactly as the mediator photon of the SM S-channel Bhabha scattering process.

Introducing the acceptance corrections the equation 6.5 transforms into the following:

$$\tilde{S} = \frac{N_{X17} \times Acc_{X17}}{\sqrt{N_{X17} \times Acc_{X17} + N_{Tch} \times Acc_{Tch} + N_{Sch} \times Acc_{Sch}}} \tag{6.8}$$

where $\tilde{S}$ represents the signal significance expressed in number of σs.

Fig. 6.1 shows two 2-D histogram with the significance as a function of the total number of Positron on Target N^{PoT}, in the range of $2 \cdot 10^{10} < N^{PoT} < 2 \cdot 10^{11}$, and the X17 coupling with the electrons g_{Ve}, in the range $10^{-4} < g_{Ve} < 10^{-3}$, which is the unexplored range (see Fig. 7.1). Both of the variables considered are divided in 10 equal intervals. The condition $\tilde{S} \geq 5$ is considered as a discovery and used as border for the discovery potential (red line). For every coupling greater than the one crossed by the red line, the X17 can be discovered by PADME using a data sample as big as the value on the X axis.

Fig. 6.1a is characterised by $R_{min} = 90$ mm, $R_{max} = 270$ mm and $E_{min} = 100$ MeV, while fig. 6.1b by $R_{min} = 190$ mm, $R_{max} = 270$ mm and $E_{min} = 100$ MeV. In particular, the first choice includes almost the entire surface of the calorimeter, while the second is aimed at reducing the BG contribution. The obtained discovery potential for the two set of cuts is similar. Despite the higher R_{min} allows minimising the background, the lower minimum radius set of the cuts reaches the best discovery potential. This is the result of the linear dependence of the significance from the number of X17 detected events. Rejecting the BG on the other hand only improves the significance as the square root of N_{BG}. On the contrary the significance strongly depends on the value of g_{Ve} as the number of produced X17 i proportional to g_{Ve}^2
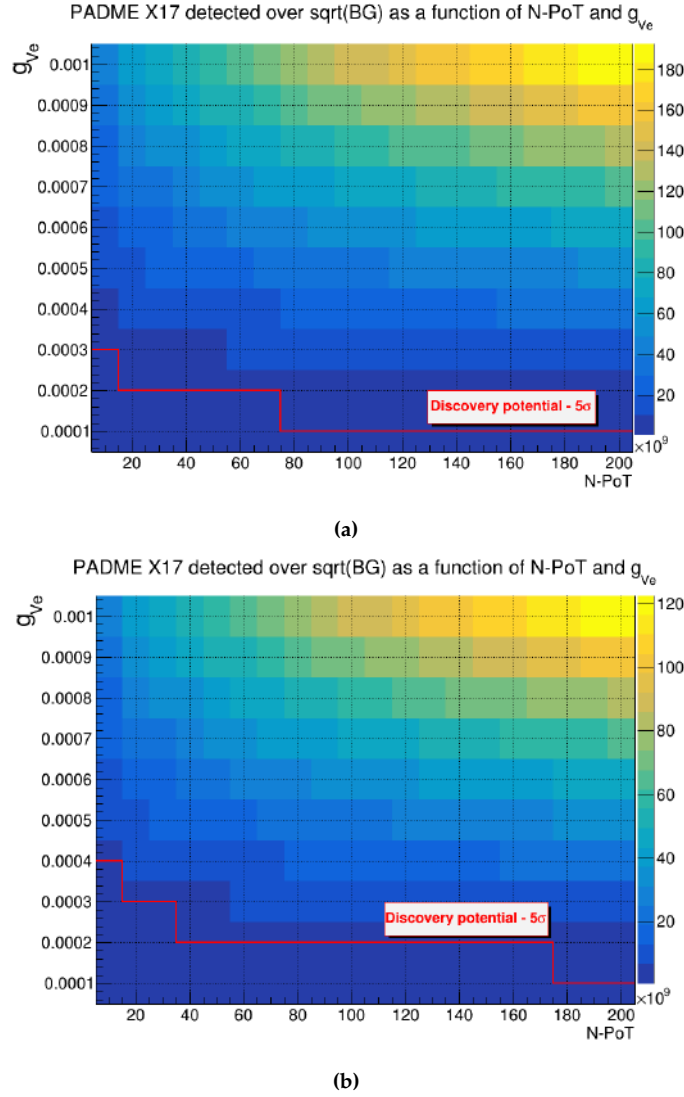
(a)

(b)

Figure 6.1: The PADME discovery potential as a function of the total Number of Positron on Target N^{PoT} and the X17 coupling with the electrons g_{Ve}. **(a)** It is shown the histogram characterised by $R_{min} = 90$ mm, $R_{max} = 270$ mm and $E_{min} = 100$ MeV. **(b)** It is shown the histogram characterise by $R_{min} = 190$ mm, $R_{max} = 270$ mm and $E_{min} = 100$ MeV.

6.3   PADME exclusion power

In this section I compute the PADME exclusion power for the X17 electron coupling g_{V_e}. To estimate how many N^{PoT} are needed to touch unexplored X17 parameter space regions, I start calculating the minimum number of detected X17 needed to reach the 90% Confidence Level.

$$N^{X17}(90\%CL) > 1.2\,\sigma_{BG} \tag{6.9}$$

where $\sigma_{BG} = \sqrt{N_{Sch} + N_{Tch}}$ and $N_{Sch,Tch}$ are the number of detected S- and T-channels background events at the end of the selection cuts. The number of

detected events follow the Poissonian statistics, therefore the uncertainty on the value of N_{BG} can be estimated as $\sigma_{N_{BG}} = \sqrt{N_{BG}}$.

Fig. 6.2 shows the number of detected X17 needed to reach the 90% Confidence Level as a function of the N^{PoT} in the same range considered in Fig. 6.1. This number only depends on the total number of PoT acquired being the error on N_{BG} proportional to $\sqrt{N_{PoT}}$.

The continuous line represents the selection with $R_{min} = 90$ mm, while the dashed one the selection with $R_{min} = 190$ mm. The latter (dashed line) requires as expected smaller number of detected events having higher background rejection factor.
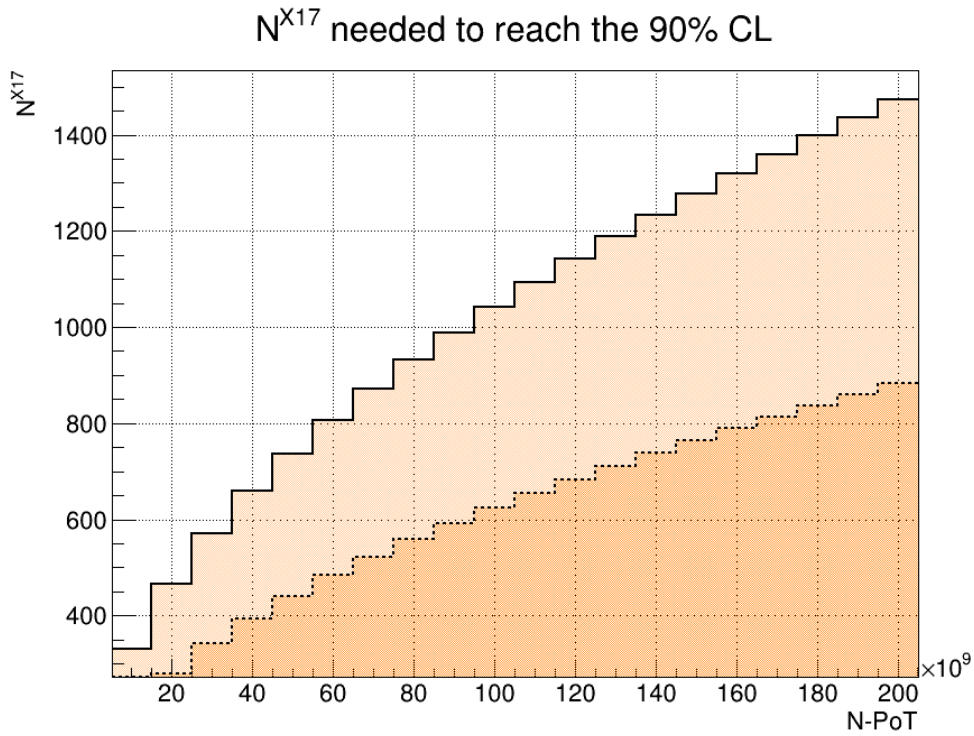

Figure 6.2: The number of detected X17 candidates needed to reach the 90% Confidence level exclusion as a function of the total number of Positron on Target N^{PoT}. The continuous line is associated to the selection with $R_{min} = 90$ mm while the dashed one to the selection with $R_{min} = 190$ mm.

Starting from equation 6.9, I can compute the minimum value of the X17 to electron coupling g_{Ve} able to provide enough detected X17 to allow the exclusion. To obtain the number of detected events N_{det}^{X17} as a function of the coupling, I multiply the total number of X17 bosons produced according to equation 5.13 N_{prod}^{X17} for the S-channel acceptance:

$$N_{det}^{X17} = N_{prod}^{X17} \times Acc_{Sch}. \tag{6.10}$$

In doing this, I assume that the lifetime of X17 is small compared to the detector resolution on the vertex position so that the X17 decay into e^+e^- can be considered prompt. By definition, the lifetime associated to the width in equation 5.1 is:

$$\tau = \frac{\hbar}{\Gamma_V} \left(\frac{0.001}{g_{Ve}} \right)^2 \simeq 1.3 \times 10^{-6} \left(\frac{0.001}{g_{Ve}} \right)^2 \text{ ns.} \tag{6.11}$$

Using N_{det}^{X17} I can compute the accessible g_{Ve} values to reach the 90% CL and the total number of Positron on Target N^{PoT}.

Fig. 6.3 shows the exclusion power of the electron coupling as a function of the total number of Positron on Target N^{PoT}, in the same range in Fig. 6.1 and according with the same convention in Fig. 6.2.

The red line is the actual upper bound of the unexplored g_{Ve} region imposed by the NA64 experiment [18].
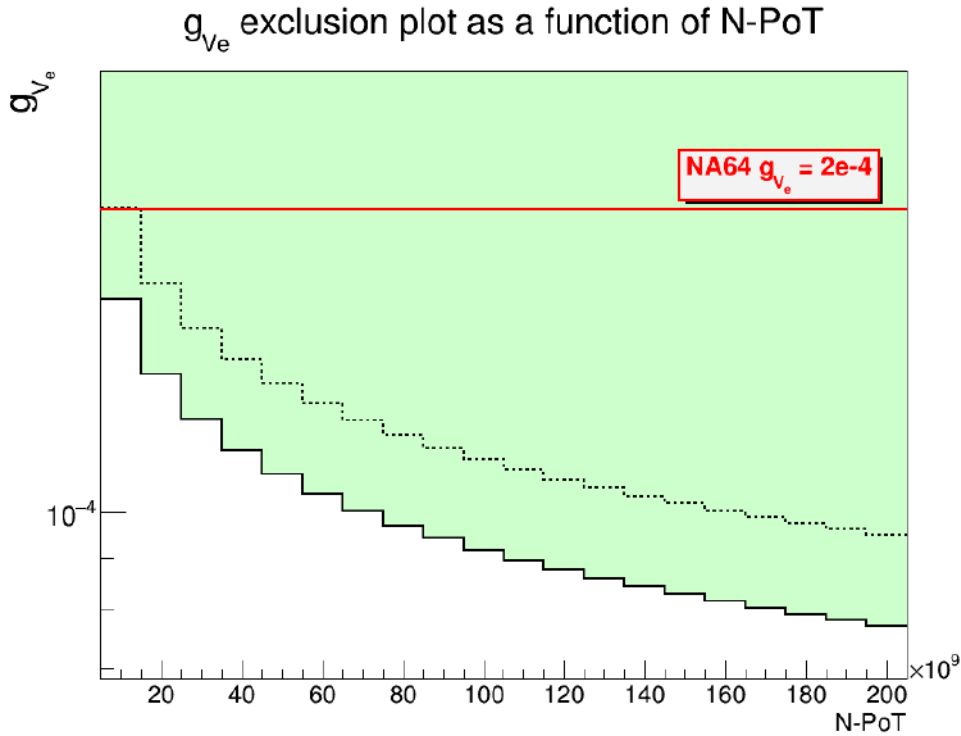

Figure 6.3: The exclusion g_{Ve} plot as a function of the total number of Positron on Target N^{PoT}. The continuous line is associated to the set of cuts with $R_{min} = 90$ mm and the dashed line to the one with $R_{min} = 190$ mm. The red line is the NA64 upper bound [18].

The continuous line allows to explore smaller couplings values overcoming the NA64 bound even with $N^{PoT} = 10^{10}$, representing the best choice of cuts. So far I

studied the sensitivity of the experiment at the exact resonant energy, in the next section I will introduce the X17 production derived in 5.1.

6.4 The X17 search using cross section scan

Due to the tiny width of the X17 resonance, caused by the very small coupling of X17 to SM particles, the limit presented in the previous section are only valid very close to the actual mass of the X17. Since the X17 mass is known with limited precision, $\sigma \sim 0.2 \ MeV$ a strategy to explore a mass region of scale 1 MeV is needed. Thanks to the unique possibility of changing the beam positron energy almost continuously in the range 100-500 MeV, the LNF BTF allows PADME to cover the entire desired interval of masses. Changing the positron beam energy is in fact equivalent to scanning the invariant mass region, since:

$$\sqrt{s} = M_{X17} = \sqrt{2E_{beam}m_e}. \tag{6.12}$$

To optimise the X17 production cross section a low energy spread beam is also needed so that many positrons can reach the exact resonant energy and profit by the cross section enhancement. Studies performed on PADME Run II data set, demonstrated that the beam energy spread can be pushed down to the level of $\sim 0.25\%$ [57]. At the resonance energy ~ 290 MeV the beam energy spread will be 0.7 MeV, which translates into a mass region covered at $\pm 1\sigma$ of the order of 50 keV in mass.

To scan the whole X17 allowed mass range, I change the energy of the positron beam, then I consider 21 resonant masses between $\simeq 16$ MeV and $\simeq 17.5$ MeV, which correspond to the beam energy interval 260 MeV $< E_{beam} < 300$ MeV. The 21 energy steps are obtained dividing the beam energy range of 40 MeV in 21 equal steps of 2 MeV each, which is a bit larger with respect the considered energy resolution of the Gaussian $\delta E = 0.7$ MeV. Precisely compute the number of X17 and BG events produced for each mass value I used 21 gaussian, one for each resonance and I defined each point of the distribution in Fig. 6.4 as the sum of the contribution coming from two neighbour Gaussian.

Fig. 6.4 shows the number of candidates N_{tot}^{X17} as a function of the X17 mass M_{X17} with two different choices of N^{PoT}. The continuous lines represent the mass scan studied, each peak of the distribution is produced through the interaction of the target with 10^{11} (teal) and 10^{10} (blue) Positron on Target. The continuous lines represent the number of produced X17 using the mass scan technique while the
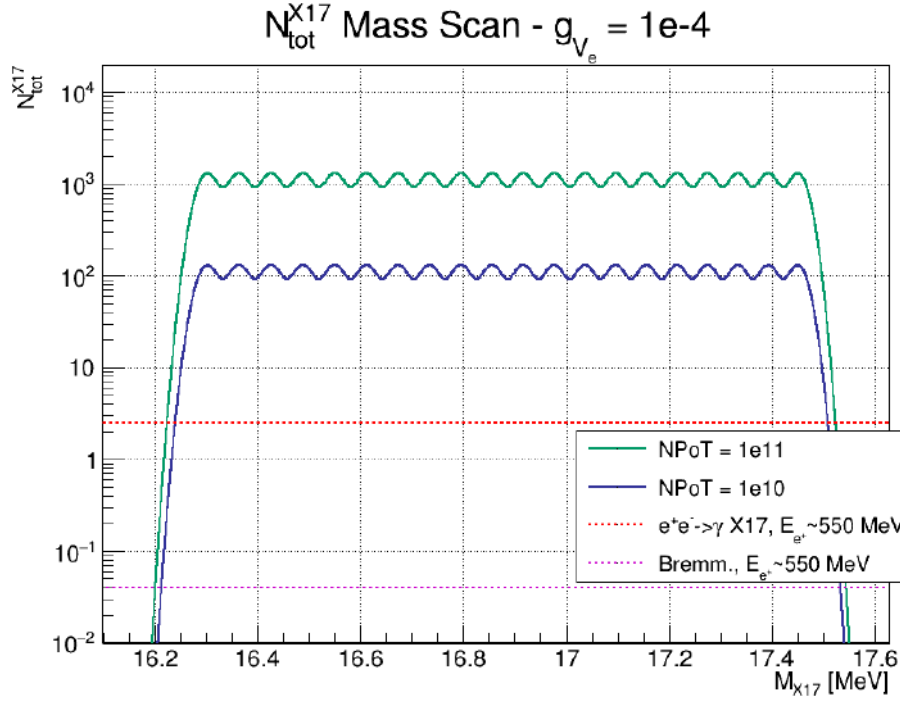
Figure 6.4: The mass scan of the X17 resonant production with coupling $g_{Ve} = 10^{-4}$. The teal continuous line is the distribution of the X17 produced with $N^{PoT} = 10^{11}$, the blue with $N^{PoT} = 10^{11}$, the dashed red line represents the X17-production via the $e^+e^- \rightarrow X17\gamma$ process with $E_{beam} = 550$ MeV [51] and the dashed magenta line represents the X17 Bremsstrahlung-like production with $E_{beam} = 550$ MeV [51].

two dashed lines correspond to the X17-production via Bremsstrhalung and associated production at energies close to the PADME Run II. All of the lines are obtained using the same value of the electron coupling $g_{Ve} = 10^{-4}$. I considered two different values of N^{PoT} to understand exactly how many candidates can be produced. The red dashed line is the distribution of the X17 produced through $e^+e^- \rightarrow X17\gamma$ process and the magenta dashed line is the distribution of the candidates emitted via a radiative process (Bremsstrahlung-type). These processes are studied in the Run I e II of the PADME experiment [51] with $E_{beam} = 550$ MeV. Both off-resonance distribution are derived with $N^{PoT} = 10^{11}$. The difference in between teal line and the dashed lines demonstrates the big advantage of using the resonant production.

Using the same procedure defined in the previous chapter I obtain from Fig. 6.5 the corresponding achievable 90% CL limit on the g_{Ve}.

The Fig. 6.5 shows the X17 electron coupling g_{Ve} as a function of the X17 mass for two different values of the total number of Positron on Target $N^{PoT} = 10^{10}$ and $N^{PoT} = 10^{11}$. Each of the peak in the distribution corresponds to the resonant

mass of one of the 21 beam energy used for the scan in Fig. 6.4. The limits are represented by the two continuous lines, the teal line is produced with $N^{PoT} = 10^{11}$ for each energy point, while the blue with $N^{PoT} = 10^{10}$. The red line represents the actual upper bound of $g_{Ve} = 2 \cdot 10^{-4}$, set by the NA64 experiment [18].

The results in Fig. 6.5 show that the production of X17 with $N^{PoT} = 10^{11}$ allows to test all the range of the coupling still unexplored in Fig. 7.1, going deepen into the lower bound given by the previous results [18].
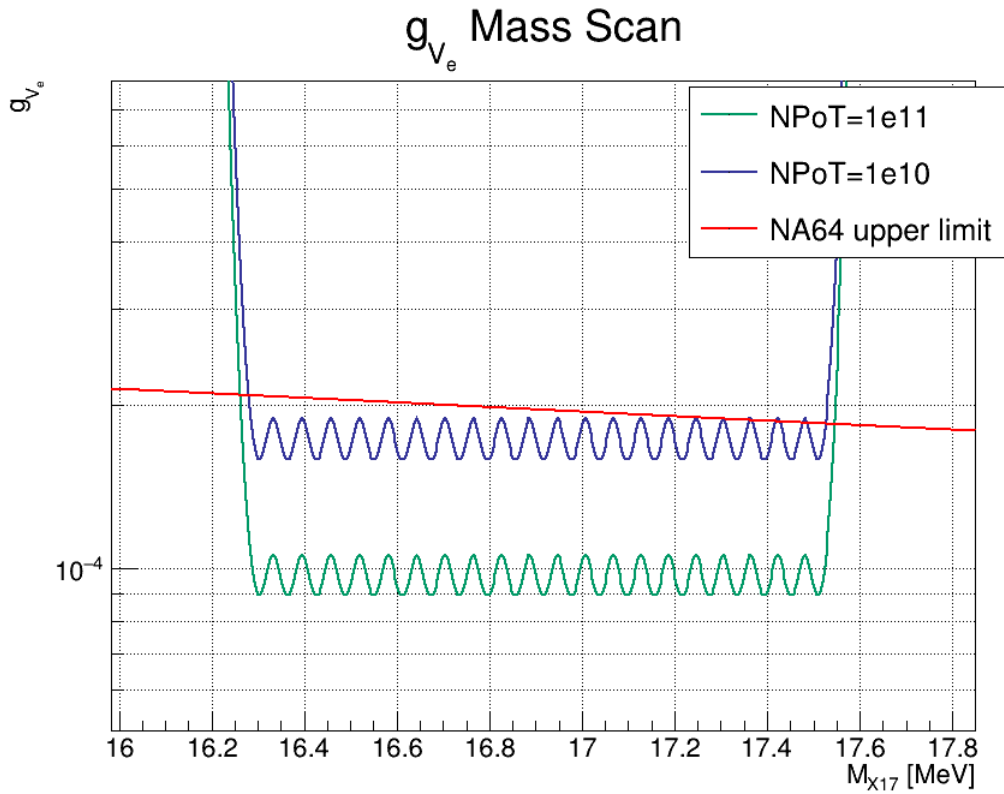

Figure 6.5: The 90% CL exclusion limit on the electrons coupling g_{Ve}. The teal line is associated to a production with $N^{PoT} = 10^{11}$, the blue to a production with $N^{PoT} = 10^{10}$. The NA64 bound [18] is represented with the red line.

7 Conclusions

In order to demonstrate the relevance of a PADME exclusion limit on the path to confirm or disprove the existence of the X17 particle, I add the results of this thesis work to the actual parameter space plot. Fig. 7.1 [54] shows the constraints on the parameters space at low energies, between 10 MeV and 24 MeV. On the Y axis the coupling of the vector particle to leptons is considered. The range in which the X17 boson is expected [9] is shown by the red vertical band. The teal area is the region accessible to the PADME experiment with a total number of Positron on Target of 21×10^{11}, (10^{11} PoT for each beam energy point in Fig. 6.5). The dark green area represents the exclusion for a total number of Positron on Target $N^{PoT} = 2.1 \times 10^{11}$ (10^{10} PoT for each beam energy point). The remaining filled areas represent limits obtained by previous experiments: KLOE [58] (orange region), NA64 [18] (navy region), E141 [59] (green region), KEK and OR-SAY [60, 61] (grey region). The red band represents the X17 $\pm 1\sigma$ mass range, imposed by the observation of the ^{8}Be and ^{4}He anomaly [54].

Concluding, the analysis of this thesis shows that the PADME experiment has the potential to completely cover the remaining open parameter space for the X17 vector hypothesis with a minimum data sample of $N^{PoT} = 2.1 \times 10^{11}$. This analysis assumes that the background coming from the $e^+e^- \rightarrow \gamma\gamma$ process can be controlled using the ETagger detector, and that the beam related background is negligible with respect to Bhabha scattering.

Under these assumptions, using a beam multiplicity of ~ 2500 Positron on Target per bunch and $N_{bunch} = 49$/s, PADME will be able to collect $\sim 10^{10}$ positron on target in $24h$ of beam time. The minimum data sample required, 2×10^{11} $N^{PoT} = 1 \times 10^{10} \times$ beam energy point, will then require order of one month of data taking with reasonable beam up time. Reaching the level of $1 \times 10^{11}/$ beam energy point, will require a much longer data taking period > 6 months, or the possibility or running with order 10000 positrons on target/bunch.

During the second half of July 2022, a first assessment of the maximum multiplicity per bunch and of the beam related background, will be obtained during the commissioning phase. The experiment is expected to start the data taking for
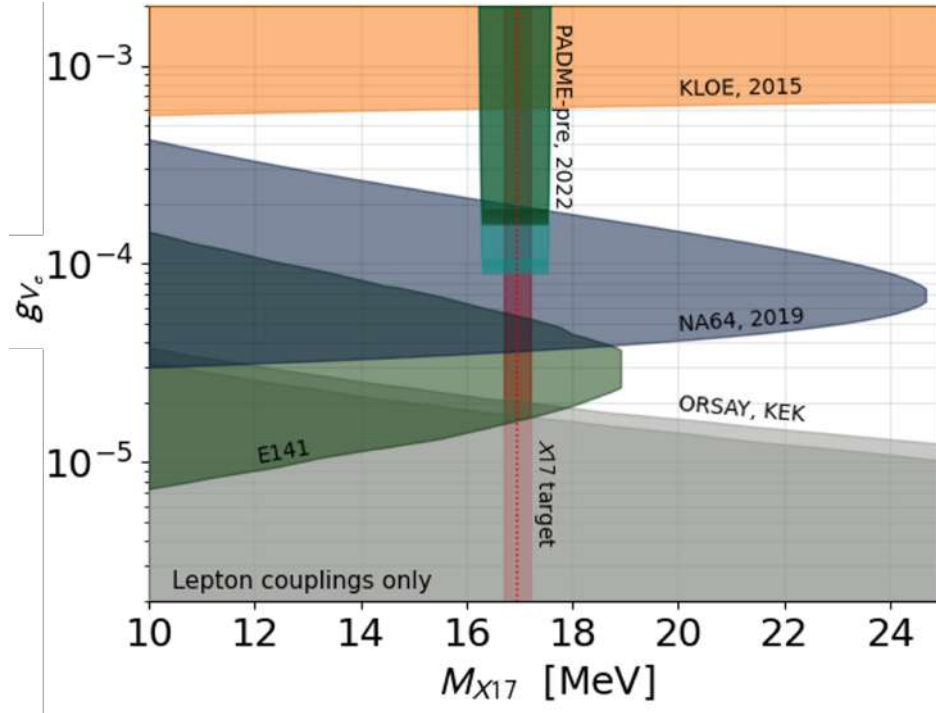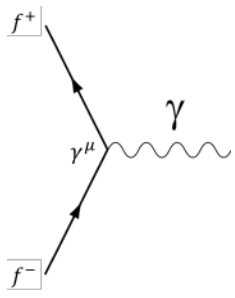
Figure 7.1: The actual parameters space. The PADME production with 21×10^{11} Positron on Target is represent with the teal region, while the dark green represents the production with $N^{PoT} = 21 \times 10^{10}$. The experimental limits provided others experiments are: KLOE [58] (orange region), NA64 [18] (navy region), E141 [59] (green region), KEK [60] and ORSAY [61] (grey region). The red band represents the X17 mass range.

physics for *Run III* during Autumn 2022 with the aim of collecting $2-4 \times 10^{11}$ PoT with beam energy in the range $260 - 300$ MeV close to the X17 resonant energy.

Appendices

A Feynman rules

The Feynman rules help us to write down the perturbation theory of Quantum field Theory [50, 52]. In this thesis we will focus on QED processes only, so there will be only the relative rules. Feynman rules associate a to each component of a Feynman diagrams a perturbation theory term as follow:

- QED vertex with two fermions and one : γ^μ $:=$ $\imath e Q_f \gamma^\mu$

- ingoing fermion: l —————• $:=$ $u_s(p)$

- outgoing fermion: •————— l $:=$ $\bar{u}_s(p)$

- ingoing antifermion: $\bar{l}$ —————• $:=$ $\bar{v}_s(p)$

- outgoing antifermion: •————— $\bar{l}$ $:=$ $v_s(p)$

- ingoing photon: γ $:=$ $\varepsilon_\mu(p)$

- outgoing photon: γ $:=$ $\varepsilon_\mu(p)^*$

- photon propagator: γ $:=$ $\frac{-\imath g^{\mu\nu}}{q^2 + \imath \varepsilon}$

- fermion propagator: l $:=$ $\frac{\imath(\not{p} + m_f)}{p^2 - m_f^2 + \imath\varepsilon}$

where Q_f is the fermion electric charge and it is $Q_f = 1$ for each one.

B Gamma matrices and Dirac identities

The γ^μ are a set of four $n \times n$ matrices that satysfies anticommutation relations [50, 52]

$$\{\gamma^\mu, \gamma^\nu\} \equiv \gamma^\mu\gamma^\nu + \gamma^\nu\gamma^\mu = 2g^{\mu\nu} \times \mathbb{1}_{n \times n} \tag{B.1}$$

where

$$g^{\mu\nu} = \begin{pmatrix} 1 & 0 & 0 & 0 \\ 0 & -1 & 0 & 0 \\ 0 & 0 & -1 & 0 \\ 0 & 0 & 0 & -1 \end{pmatrix} \tag{B.2}$$

is the Minkowski's metric tensor. γ^μ are four contravariant 4×4 matrices in Dirac representation and their expressions are:

$$\gamma^0 = \begin{pmatrix} \mathbb{1}_{2\times 2} & 0 \\ 0 & -\mathbb{1}_{2\times 2} \end{pmatrix}, \quad \gamma^i = \begin{pmatrix} 0 & \sigma^i \\ -\sigma^i & 0 \end{pmatrix} \tag{B.3}$$

where σ^i are the Pauli's matrices. These metrices are traceless and γ^0 is hermitian, while $gamma^i$ are anti-hermitian. There is a fifth reducible matrix, called γ^5 and defined as:

$$\gamma^5 = \imath\gamma^0\gamma^1\gamma^2\gamma^3 = \begin{pmatrix} 0 & \mathbb{1} \\ \mathbb{1} & 0 \end{pmatrix} \tag{B.4}$$

gamma matrices have the following algebric properties:

- $(\gamma^0)^\dagger = \gamma^0$, $(\gamma^i)^\dagger = -\gamma^i$

- γ^5 matrix satisfies: $(\gamma^5)^\dagger = \gamma^5$, $(\gamma^5)^2 = \pm\mathbb{1}$, $\{\gamma^5, \gamma^\mu\} = \gamma^5\gamma^\mu + \gamma^\mu\gamma^5 = 0$

there are also some identities follow from the fundamental anticommutation relation, so they hold in any basis:

1. $\gamma^\mu\gamma_\mu = 4\mathbb{1}$

2. $\gamma^\mu\gamma^\nu\gamma_\mu = -2\gamma^\nu$

3. $\gamma^\mu \gamma^\nu \gamma^\rho \gamma_\mu = 4g^{\nu\rho}\mathbb{1}$

4. $\gamma^\mu \gamma^\nu \gamma^\rho \gamma^\omega \gamma_\mu = -2\gamma^\omega \gamma^\rho \gamma^\nu$

one can demonstrate them using the anticommutation rule B.1.

Starting from γ's definitions, algebric properties and the previous identities, it is possible to derive trace identies:

1. $\text{Tr}(\gamma^\mu) = 0$

2. $\text{Tr}(\gamma^\mu \gamma^\nu \gamma^\alpha) = 0$, and every trace of an odd number of gamma matrix. Trace of γ^5 times an odd number of gamma is still equal to zero

3. $\text{Tr}(\gamma^\mu \gamma^\nu) = 4g^{\mu\nu}$

4. $\text{Tr}(\gamma^\mu \gamma^\nu \gamma^\alpha \gamma^\beta) = 4(g^{\mu\nu}g^{\alpha\beta} + g^{\mu\beta}g^{\nu\alpha} - g^{\mu\alpha}g^{\nu\beta})$

5. $\text{Tr}(\gamma^5) = \text{Tr}(\gamma^5 \gamma^\mu \gamma^\nu) = 0$

6. $\text{Tr}(\gamma^\mu \gamma^\nu \gamma^\alpha \gamma^\beta \gamma^5) = -4i\varepsilon^{\mu\nu\alpha\beta}$

7. $\text{Tr}(\gamma^\mu \gamma^\nu \gamma^\alpha \gamma^\beta ...) = \text{Tr}(...\gamma^\beta \gamma^\alpha \gamma^\nu \gamma^\mu)$

to prove these identies one has to use the main trace properties, that are the sum rule $\text{Tr}(A + B) = \text{Tr}(A) + \text{Tr}(B)$, the ciclicity $\text{Tr}(ABC) = \text{Tr}(CAB) = \text{Tr}(BCA)$ and the product with a scalar $\text{Tr}(kA) = k\text{Tr}(A)$.

Bibliography

[1] F. Zwicky. Die Rotverschiebung von extragalaktischen Nebeln. *Helv. Phys. Acta*, 6:110–127, 1933.

[2] V. C. Rubin, N. Thonnard, and W. K. Ford, Jr. Rotational properties of 21 SC galaxies with a large range of luminosities and radii, from NGC 4605 /R = 4kpc/ to UGC 2885 /R = 122 kpc/. *Astrophys. J.*, 238:471, 1980.

[3] Douglas Clowe, Marusa Bradac, Anthony H. Gonzalez, Maxim Markevitch, Scott W. Randall, Christine Jones, and Dennis Zaritsky. A direct empirical proof of the existence of dark matter. *Astrophys. J. Lett.*, 648:L109–L113, 2006.

[4] Mauro Raggi and Venelin Kozhuharov. Results and perspectives in dark photon physics. *Riv. Nuovo Cim.*, 38(10):449–505, 2015.

[5] P. A. Zyla et al. Review of Particle Physics. *PTEP*, 2020(8):083C01, 2020.

[6] R. Bernabei et al. New results from DAMA/LIBRA. *Eur. Phys. J. C*, 67:39–49, 2010.

[7] B. Abi et al. Measurement of the Positive Muon Anomalous Magnetic Moment to 0.46 ppm. *Phys. Rev. Lett.*, 126(14):141801, 2021.

[8] A. J. Krasznahorkay et al. Observation of Anomalous Internal Pair Creation in Be8 : A Possible Indication of a Light, Neutral Boson. *Phys. Rev. Lett.*, 116(4):042501, 2016.

[9] Jonathan L. Feng, Tim M. P. Tait, and Christopher B. Verhaaren. Dynamical Evidence For a Fifth Force Explanation of the ATOMKI Nuclear Anomalies. *Phys. Rev. D*, 102(3):036016, 2020.

[10] Xilin Zhang and Gerald A. Miller. Can a protophobic vector boson explain the ATOMKI anomaly? *Phys. Lett. B*, 813:136061, 2021.

[11] Enrico Nardi, Cristian D. R. Carvajal, Anish Ghoshal, Davide Meloni, and Mauro Raggi. Resonant production of dark photons in positron beam dump experiments. *Phys. Rev. D*, 97(9):095004, 2018.

[12] L. Darmé, E. Nardi, and M. Raggi. private comunication. 2022.

[13] Alessandra Filippi and Marzio De Napoli. Searching in the dark: the hunt for the dark photon. *Rev. Phys.*, 5:100042, 2020.

[14] J. P. Lees et al. Search for Invisible Decays of a Dark Photon Produced in e^+e^- Collisions at BaBar. *Phys. Rev. Lett.*, 119(13):131804, 2017.

[15] Eduardo Cortina Gil et al. Search for production of an invisible dark photon in π^0 decays. *JHEP*, 05:182, 2019.

[16] Hooman Davoudiasl, Hye-Sung Lee, and William J. Marciano. Muon $g2$, rare kaon decays, and parity violation from dark bosons. *Phys. Rev. D*, 89(9):095006, 2014.

[17] Rouven Essig, Jeremy Mardon, Michele Papucci, Tomer Volansky, and Yi-Ming Zhong. Constraining Light Dark Matter with Low-Energy e^+e^- Colliders. *JHEP*, 11:167, 2013.

[18] D. Banerjee et al. Search for Axionlike and Scalar Particles with the NA64 Experiment. *Phys. Rev. Lett.*, 125(8):081801, 2020.

[19] M. E. Rose. Internal Pair Formation. *Phys. Rev.*, 76:678–681, 1949. [Erratum: Phys.Rev. 78, 184–184 (1950)].

[20] U. Leinberger et al. First energy and angle differential measurements of e+ e- pairs emitted by internal pair conversion of excited heavy nuclei. *Eur. Phys. J. A*, 1:249–256, 1998.

[21] F. W. N. de Boer, R. van Dantzig, J. van Klinken, K. Bethge, H. Bokemeyer, A. Buda, K. A. Muller, and K. E. Stiebing. Excess in e+ e- pairs near 9 MeV/c^2 invariant mass. *J. Phys. G*, 23:L85–L96, 1997.

[22] J. Gulyás, T. J. Ketel, A. J. Krasznahorkay, M. Csatlós, L. Csige, Z. Gácsi, M. Hunyadi, A. Krasznahorkay, A. Vitéz, and T. G. Tornyi. A pair spectrometer for measuring multipolarities of energetic nuclear transitions. *Nucl. Instrum. Meth. A*, 808:21–28, 2016.

[23] Jonathan L. Feng, Bartosz Fornal, Iftah Galon, Susan Gardner, Jordan Smolinsky, Tim M. P. Tait, and Philip Tanedo. Particle physics models for the 17 MeV anomaly in beryllium nuclear decays. *Phys. Rev. D*, 95(3):035017, 2017.

[24] R. Brun, F. Bruyant, M. Maire, A. C. McPherson, and P. Zanarini. GEANT3. 9 1987.

[25] National Nuclear Data Centre https://www.nndc.bnl.gov/ensdf/.

[26] A. J. Krasznahorkay et al. New results on the ^{8}Be anomaly. *J. Phys. Conf. Ser.*, 1056(1):012028, 2018.

[27] A. J. Krasznahorkay, M. Csatlós, L. Csige, J. Gulyás, A. Krasznahorkay, B. M. Nyakó, I. Rajta, J. Timár, I. Vajda, and N. J. Sas. New anomaly observed in He4 supports the existence of the hypothetical X17 particle. *Phys. Rev. C*, 104(4):044003, 2021.

[28] D. R. Tilley, H. R. Weller, and G. M. Hale. Energy levels of light nuclei A = 4. *Nucl. Phys. A*, 541:1–104, 1992.

[29] N. J. Sas et al. Observation of the X17 anomaly in the ^{7}Li(p,e^+e^-)^{8}Be direct proton-capture reaction. 5 2022.

[30] A. J. Krasznahorkay. Status of experiments on 8Be and 4He https://agenda.infn.it/event/26303/contributions/135193/.

[31] Xilin Zhang and Gerald A. Miller. Can nuclear physics explain the anomaly observed in the internal pair production in the Beryllium-8 nucleus? *Phys. Lett. B*, 773:159–165, 2017.

[32] H. W. Hammer, C. Ji, and D. R. Phillips. Effective field theory description of halo nuclei. *J. Phys. G*, 44(10):103002, 2017.

[33] Jonathan L. Feng, Bartosz Fornal, Iftah Galon, Susan Gardner, Jordan Smolinsky, Tim M. P. Tait, and Philip Tanedo. Protophobic Fifth-Force Interpretation of the Observed Anomaly in ^{8}Be Nuclear Transitions. *Phys. Rev. Lett.*, 117(7):071803, 2016.

[34] J. R. Batley et al. Search for the dark photon in π^0 decays. *Phys. Lett. B*, 746:178–185, 2015.

[35] Manuel Meucci. MEG II experiment status and prospect. *PoS*, NuFact2021:120, 2022.

[36] Mauro Raggi and Venelin Kozhuharov. Proposal to Search for a Dark Photon in Positron on Target Collisions at DAΦNE Linac. *Adv. High Energy Phys.*, 2014:959802, 2014.

[37] Paolo Valente et al. Linear Accelerator Test Facility at LNF: Conceptual Design Report. 3 2016.

[38] Isabella Oceano. *Searching for the dark photon with PADME and measurment of the $e^+e^- \rightarrow \gamma\gamma$ cross section at $\sqrt{s} = 21$ MeV*. PhD thesis, Universita' Del Salento, 2021.

[39] Venelin Kozhuharov, Mauro Raggi, and Paolo Valente. New Projects on Dark Photon Search. *Frascati Phys. Ser.*, 64:310–318, 2017.

[40] P. Albicocco et al. The PADME experiment. *Frascati Phys. Ser.*, 66:337–344, 2018.

[41] Federica Oliva. *The PADME Active Diamond Target and Positron Bremsstrahlung Analysis*. PhD thesis, Universita' Del Salento, Salento U., 2021.

[42] https://home.cern/science/accelerators/super-proton-synchrotron.

[43] F. Ferrarotto, L. Foggetta, G. Georgiev, P. Gianotti, V. Kozhuharov, E. Leonardi, G. Piperno, M. Raggi, C. Taruggi, L. Tsankov, and P. Valente. Performance of the prototype of the charged-particle veto system of the padme experiment. *IEEE Transactions on Nuclear Science*, 65(8):2029–2035, 2018.

[44] M. Raggi et al. Performance of the PADME Calorimeter prototype at the DAΦNE BTF. *Nucl. Instrum. Meth. A*, 862:31–35, 2017.

[45] P. Albicocco et al. Characterisation and performance of the PADME electromagnetic calorimeter. *Journal of Instrumentation*, 15(10):T10003–T10003, oct 2020.

[46] A. Frankenthal et al. Characterization and performance of padme's cherenkov-based small-angle calorimeter. *Nuclear Instruments and Methods in Physics Research Section A: Accelerators, Spectrometers, Detectors and Associated Equipment*, 919:89–97, 2019.

[47] I. Valin et al. A reticle size CMOS pixel sensor dedicated to the STAR HFT. *Journal of Instrumentation*, 7(01):C01102–C01102, jan 2012.

[48] T. Poikela et al. Timepix3: a 65k channel hybrid pixel readout chip with simultaneous ToA/ToT and sparse readout. *Journal of Instrumentation*, 9(05):C05013–C05013, may 2014.

[49] https://www.crystals.saint-gobain.com/radiation-detection-scintillators/plastic-scintillators/bc-400-bc-404-bc-408-bc-412-bc-416.

[50] Steven Weinberg. *The Quantum theory of fields. Vol. 1: Foundations*. Cambridge University Press, 6 2005.

[51] P. Albicocco et al. Commissioning of the PADME experiment with a positron beam. 5 2022.

[52] Michael E. Peskin and Daniel V. Schroeder. *An Introduction to quantum field theory*. Addison-Wesley, Reading, USA, 1995.

[53] Alexander Belyaev, Neil D. Christensen, and Alexander Pukhov. CalcHEP 3.4 for collider physics within and beyond the Standard Model. *Comput. Phys. Commun.*, 184:1729–1769, 2013.

[54] L. Darmé and E. Nardi. private comunication. 2022.

[55] A. J. Krasznahorkay et al. New evidence supporting the existence of the hypothetic X17 particle. 10 2019.

[56] Gianfranco Pradisi. *Lezioni di metodi matematici della fisica*. Edizioni della Normale, Pisa, 2012.

[57] F. Bossi et al. The PADME beam line Monte Carlo simulation. 4 2022.

[58] A. Anastasi et al. Limit on the production of a low-mass vector boson in $e^+e^- \to U\gamma$, $U \to e^+e^-$ with the KLOE experiment. *Phys. Lett. B*, 750:633–637, 2015.

[59] E. M. Riordan et al. A Search for Short Lived Axions in an Electron Beam Dump Experiment. *Phys. Rev. Lett.*, 59:755, 1987.

[60] A. Konaka et al. Search for Neutral Particles in Electron Beam Dump Experiment. *Phys. Rev. Lett.*, 57:659, 1986.

[61] M. Davier and H. Nguyen Ngoc. An Unambiguous Search for a Light Higgs Boson. *Phys. Lett. B*, 229:150–155, 1989.